UNIVERSITA' DI PISA

DIPARTIMENTO DI FISICA
Corso di Laurea Magistrale in Fisica

Tesi di Laurea Magistrale

Surface acoustic wave (SAW)-enhanced surface plasmon resonance (SPR) biosensor

Candidato

Gina Greco

Relatore

Dr. Marco Cecchini

Anno Accademico 2013/2014

Contents

Introduction

After the birth of lab-on-a-chip (LOC) technology in the 80's and its growth through the 90's, a lot of scientists have worked in this field to produce devices for fluid manipulation, tools for biological applications, and sensors (to name but a few) [1] [2] [3]. LOC technology has the aim of integrating one or more laboratory functions onto a single chip with areas from 1 mm^2 up to no more than few cm^2.

With such an objective it is typically necessary in a LOC device to handle small quantities of fluids (usually of the order of μL down to less than 1 pL), and for this reason is often considered synonymous with microfluidics. One of the biggest challenge for microfluidics is mixing. In fact, microfluidic systems are generally characterized by laminar fluid flow where mixing is governed by diffusion. The problem of slow mixing can be overcome with the use of surface acoustic wave(SAW)-induced streaming [4].

SAWs are mechanical oscillations which propagate along the surface of a given crystal. In piezoelectric materials they can be generated using interdigital transducers (IDT), which are fabricated using thin-film metal deposition on the piezoelectric substrate. When a SAW comes into contact with the edge of a liquid in its path, the acoustic energy diffracts into the fluid due to the mismatch between the sound velocity in the substrate and the liquid, causing a longitudinal pressure wave front that gives rise to the acoustic streaming. By inducing acoustic-streaming, solutions can be efficiently mixed with times that are significantly shorter than without SAWs [5].

Surface plasmon resonance (SPR) sensors have also been developed concurrently to SAW devices because of their high reliability and quantitative real-time measurements, becoming a central tool for characterizing and quantifying biomolecular interactions.

Following the Drude model of electrical conduction, surface plasmons (SPs) can be considered as propagating electron density waves occurring at the interface between a metal and a dielectric and can alternatively be viewed as electromagnetic waves that are strongly bound to this interface. The resonance condition for SP excitation varies with the refractive index of the dielectric in the proximity (about 200 nm for visible light) of the surface of the metal film supporting the SP. A change in the resonance condition measured with an optical setup can be used to detect changes in the refractive index. SPR sensing is particularly useful for biological applications. By functionalizing the SPR sensor surface it is possible to detect binding events in real-time and quantify the concentration of the analyte to

be studied with high reliability. SPR biosensors have applications in numerous important fields including medical diagnostics, environmental monitoring, and food safety and security with resolution as low as 10^{-7} refractive index units (RIU) [3].

The aim of this master thesis work was the realization of a biosensor based on SPR which was integrated with SAW-driven microfluidics. It was the first time that such a chip was realized, characterized and used for biosensing, with the exception of Reanudin et al. [6] who made a droplet-based chip with a similar aim. Their work, however, had several critical aspects which were studied with the chip realized in this work.

Droplet-based SPR sensors in the Kretschmann configuration with wavelength modulation [7] were first characterized with solutions of water and ethanol at different concentrations. The SPR Kretschmann configuration with wavelength modulation consists of a chip placed onto a prism hit by a polychromatic light at a fixed angle (at which SPR can occur in the range of the wavelengths used). SPR is detected as a dip in correspondence of the resonant wavelength in the reflectance spectrum of p-polarized light (the only type of polarized light which can excite SPs). The chip was functionalized with biotin, and different resonant wavelength shifts were measured for streptavidin solutions at increasing concentrations. Due to the high affinity between streptavidin and biotin, when the streptavidin solution is placed in contact with the SPR functionalized gold surface, it binds to biotin making the refractive index change at the interface and causing a shift in the SPR condition. Then, a polydimethylsiloxane (PDMS) μchannel SPR sensor was used to measure the resonant wavelength shifts due to the functionalization of the SPR surface with the biotin solution and to the streptavidin (2.5 μM in a phosphate-buffered saline solution)-biotin binding events. Another chip with the same design as the previous sensor but with an IDT patterned onto the substrate in front of the microchannel was used to do the same measurements with the SAWs active. SPR was detected in two areas of the chip. In one area, consisting of the first chamber of the microchannel in front of the IDT, SAW was physically present and induced acoustic streaming and heating (side effect) in the fluid. In the other area, SAW was not present but its heating effect was still present. By measuring the resonant wavelength shifts in these two areas it was possible to decouple the streaming and heating effects of SAWs. In the case of biotin, resonant wavelength shifts were found to be higher than without SAW, showing that a better functionalization likely occurred.

Summary

This thesis is divided in two parts. In the first part the theoretical background of the physical phenomena is shown. It is divided in two chapters: the first chapter is an overview of the physics of the SPR sensing and the second chapter is an overview of the SAW-induced streaming. In the second part the experimental results are shown. It is divided in two chapters. Chapter 3 details the chips development (design and microstructure fabrication techniques) and setup optimization. In chapter 4 all measurements and results are shown. It is divided in two sections. The first section shows the chip characterization and the measurements and results obtained with droplet-based and μchannel SPR sensors (where

SAW was inactive). In the second section the acoustic and heating characterization of the SAW-based SPR sensor is shown with the relative measurements and results.

Part I

Theoretical Background

1 Surface Plasmon Resonance and Biosensing

1.1 Physics of Surface Plasmon Resonance

Following the Drude model of electrical conduction, *surface plasmons* (SPs) can be considered as propagating electron density waves occurring at the interface between a metal and a dielectric. The metal (as one of the two interface materials) is essential for the generation of SPs, due to its abundant quantity of free conduction electrons. Alternatively, surface plasmons can be viewed as electromagnetic waves that are strongly bound to this interface.
The surface plasmon field at the interface can be generated at very high intensities (see next chapters), which is the main reason why surface plasmon resonance (SPR) is such a powerful tool for many types of interface studies.

1.1.1 The Evanescent Wave

In order to understand the concept of SPR sensing it is essential to study the evanescent wave, and considering the phenomenon of total internal reflection will make its comprehension easier [8].
An electromagnetic plane wave that propagates in a medium with refractive index n can be described mathematically by an electric field $\mathbf{E}$:

$$\mathbf{E} = \mathbf{E_0}\, e^{(j\boldsymbol{kr})-j\omega t} = \mathbf{E_0}\, e^{(jk_x r_x + jk_y r_y + jk_z r_z)-j\omega t} \tag{1.1}$$

where E_0 is the amplitude of the electric field, ω is the angular frequency, t is time, $\boldsymbol{k}$ is the wavevector, $\mathbf{r} = (x, y, z)$ is the position vector and $j = \sqrt{-1}$. The wavevector direction is parallel to that of the wave propagation and its magnitude is given by

$$|\boldsymbol{k}| = \sqrt{{k_x}^2 + {k_y}^2 + {k_z}^2} = n\frac{2\pi}{\lambda} = n\frac{\omega}{c} \tag{1.2}$$

where λ and c are the wavelength and propagation velocity in vacuum, respectively.
Consider now the refraction of the above wave at an interface between two media, 1 and 2, with refractive indices n_1 and n_2, respectively. α is the angle of incidence of light whereas β is the angle of refraction (as shown in Figure 1.1). The 2D case can be studied without loss of generality by setting $k_z = 0$. In this situation Snell's law holds:

$$n_1 sin\alpha = n_2 sin\beta \tag{1.3}$$

or, equivalently,

$$k_{x_1} = k_{x_2} \equiv k_x \tag{1.4}$$

By using equations (1.4) and (1.2) an expression for the component of the wavevector k_y perpendicular to the interface[1] can be found

$$k_{y_2}{}^2 = n_1{}^2 \left(\frac{2\pi}{\lambda}\right)^2 \left(\frac{n_2{}^2}{n_1{}^2} - sin^2\alpha\right) \tag{1.5}$$

Now let us assume that $n_2 < n_1$. From eq. (1.5), it can be seen that for $sin\alpha > n_2/n_1$ the right part is negative, and, consequently, k_y is purely imaginary. Returning to eq. (1.1), it can be deduced that for this case in medium 2 there is only a traveling wave parallel to the interface:

$$\mathbf{E_2} = \mathbf{E_0} e^{-\kappa_{y_2} y} e^{(jk_x x - j\omega t)} \tag{1.6}$$

with the amplitude of the electric field exponentially decaying along the y-direction with a characteristic distance $1/\ \kappa_{y_2} = 1/\ jk_{y_2}$.
This field in medium 2 is denoted as *the evanescent field*. Eq. (1.5) can be used to calculate its penetration depth, L_{pd}. From its value it is possible to understand the interface sensitivity of the evanescent field. A change in the refractive index can be detected if it occurs within the penetration depth.

1.1.2 SP Dispersion Equation and Resonance

Only p-polarized light (whose electric field vector lies in the plane of incidence) interacting with an interface will be discussed here since only p-polarized light can excite SPs. Indeed only an electric field with a component perpendicular to the interface can induce surface charge density oscillations and only p-polarized light has a perpendicular electric field component [9].
SP dispersion equation can be found following Cardona's approach [10]. For any interface between two media, the complex reflection coefficient r_p for the electric field of p-polarized light electric is described by Fresnel's equations [11]

$$r_p = \frac{E_r}{E_i} = |r_p| e^{j\phi} = \frac{\tan(\alpha - \beta)}{\tan(\alpha + \beta)} e^{j\phi} \tag{1.7}$$

where E_r and E_i are the reflected and incident electric fields, respectively, and the angles α and β are defined as shown in Figure 1.1.
The angles α and β are again related by Snell's law (eq. 1.3); in addition, a phase change ϕ of the reflected field relative to the incident field occurs, depending on the refractive indices of the materials involved.
For the reflectance the following relation holds:

$$R_p = |r_p|^2 \tag{1.8}$$

It is clear from eq. (1.7) that two limiting cases exist. The former occurs if $\alpha + \beta = \frac{\pi}{2}$. In this case R_p becomes zero and we are in the case of the *Brewster angle* where there is no reflection for p-polarized light. The latter occurs when $\alpha - \beta = \frac{\pi}{2}$ where

[1] Direction y is always perpendicular to the surface in this chapter.

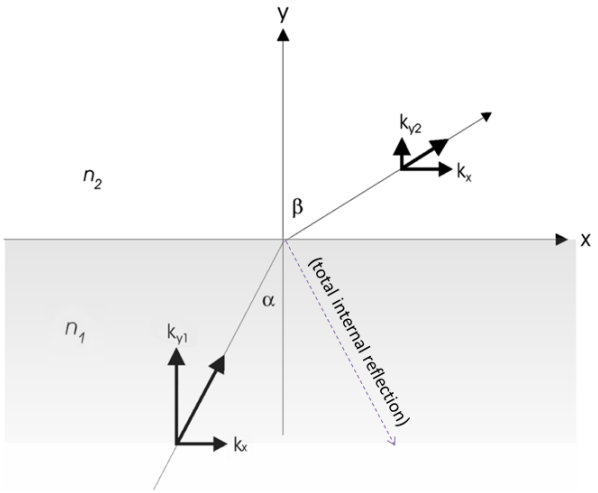

Figure 1.1: Refraction of light at an incident angle α, at an interface of two materials with refractive indices n_1 and n_2. The dashed arrow represents the case of total internal reflection. Definition of axis system and quantities. [11]

R_p becomes infinite. This is the resonant condition and it is possible to deduce the dispersion equation. For the components of the wavevector $\boldsymbol{k} = (k_x, k_y)$:

$$k_x{}^2 = k_1{}^2 - k_{y1}{}^2 = k_1{}^2 - k_x{}^2 \frac{\epsilon_1}{\epsilon_2} \tag{1.9}$$

$$k_x = \frac{\omega}{c}\sqrt{\frac{\epsilon_2\epsilon_1}{\epsilon_2+\epsilon_1}} \; and \; k_{yi} = \frac{\omega}{c}\sqrt{\frac{\epsilon_i{}^2}{\epsilon_2+\epsilon_1}} \tag{1.10}$$

where ϵ_1 and ϵ_2 are the dielectric constants ($\epsilon \equiv n^2$) of materials 1 and 2, respectively, and $i = 1$ *or* 2. Equation (1.10) is the *SPR dispersion equation for an interface between two semi-infinite media*.
Let us consider now the case where medium 2 is a metal. It contains a large number of free electrons and at angular frequency lower to the plasma frequency, $\omega < \omega_p$, its dielectric constant, ϵ_2, is negative.

$$\epsilon_2(\omega) = 1 - \frac{\omega_p{}^2}{\omega^2}, \tag{1.11}$$

where

$$\omega_p = \sqrt{\frac{4\pi\rho_e e^2}{m_e}} \tag{1.12}$$

is the so-called *plasma frequency*, ρ_e is the free electron density and e and m_e are the electron charge and mass, respectively.

As it can be seen from eqs. (1.1) and (1.2), for $\omega < \omega_p$ no electromagnetic field can propagate in a metal. Moreover, provided that $\epsilon_2 < -\epsilon_1$, k_{yi} is imaginary, whereas k_x remains real. It follows that there is an electromagnetic field which decays exponentially on both sides (cf. eq. 1.6) plumb to the interface.

What follows is a calculation of penetration depths on the basis of eq. (1.10) for a real case in order to have an idea of the quantities involved in this kind of

phenomenon. Let us consider a monochromatic light of wavelength $\lambda = 700nm$ ($\omega = 2.69 \cdot 10^{15}\ s^{-1}$) and a gold/water interface. At this wavelength $\epsilon_{gold} \approx -16$ and $\epsilon_{water} \approx 1.77$ so the penetration depths calculated to be $1/k_{y,water} \sim 238\ nm$ and $1/k_{y,gold} \sim 26\ nm$.

1.1.3 SP Properties

There are some properties of SPs that are particularly important if one is interested in using them for sensor applications: (1) the field enhancement, (2) the phase jump of the reflected field upon SP excitation and (3) the SP propagation length [8].

Field enhancement. On the basis of Fresnel's equations for the interface it is possible to calculate the electric field transmission. The electric field at the low index side of the metal can be much bigger than the electric field on the other side of the metal layer. It is found that very close to the SPR condition the intensity can be enhanced by a factor of more than 30.

Phase jump. A reflection event at an interface is generally accompanied by a phase jump of the reflected field.

Propagation length. Models and experiments indicate that a plasmon needs roughly four times the propagation length L_x for full decay or for full build-up; this propagation length is defined as

$$L_x = \frac{1}{2k_x''} \tag{1.13}$$

where k_x'' is the imaginary part of the propagation constant, k_x. In all the previous calculations only the real part of the dielectric constant was considered. In general ϵ is a complex number and for this reason it is possible to define an imaginary part of k_x. Intensity of SP decays with the square of the electric field, so at a distance x, the intensity has decreased by a factor of $e^{-2k_x''x}$. The propagation length is defined as the distance for the SP intensity to decay by a factor of $1/e$. It follows that in an SPR experiment it is possible to make areas that will behave independently, provided that these areas are significantly larger than L_x^2.

1.2 Excitation of SPs

By substitution of equations (1.11) and (1.12) into eq. (1.10), a graphical representation of the SPR dispersion relation can be obtained as shown in Figure 1.2 (line I).

It can be seen that, excluding the origin, the SPR curve never intersects the light curve (line a). This means that it is not possible to excite a plasmon using the simple configuration of a metal with a dielectric on top. One way to solve this problem it to introduce a second interface, which means adding another layer to the system. In Figure (1.2) the inset shows a thin metal layer (dielectric constant ϵ_m) placed between two dielectric materials 1 and 3 with different dielectric constants ϵ_1 and ϵ_3, with $\epsilon_1 > \epsilon_3$. Studying this system by applying Fresnel's equations to the two interfaces leads to more complex dispersion equations than eq. (1.10) (the physics

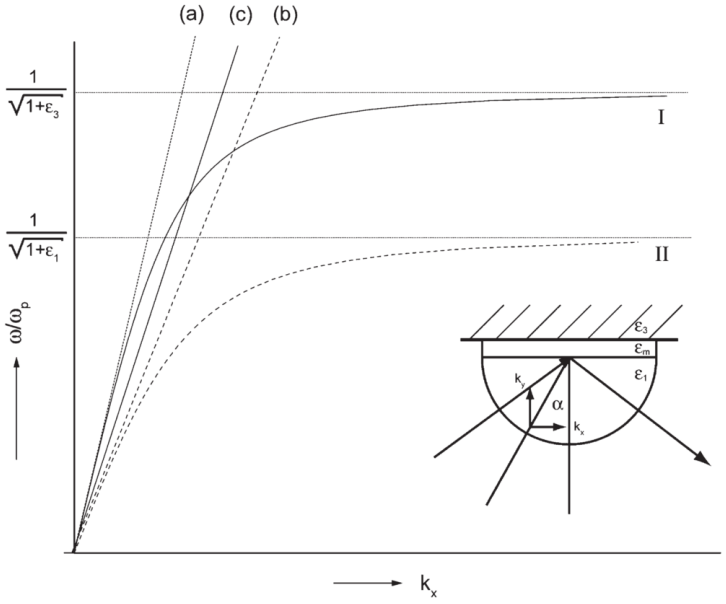

Figure 1.2: Dispersion relation for surface plasmons. Curves I and II represent the SP dispersion for the interfaces ϵ_3/ϵ_m and ϵ_1/ϵ_m, respectively. The lines a and b are the dispersion relations for "normal" light in medium ϵ_3 and ϵ_1, respectively, which are dependent on the angle of incidence α in the experimental setup as indicated in the inset. By varying α, any line c between the lines a and b can be realized [8].

of the problem remains unchanged). At this point two dispersion equations for k_x (one for each interface), are found (curve I and II) and the dispersion relation of light in medium 1 (line b) intersects the SPR curve (I). On varying the incident light angle or wavelength, we can tune the incoming wavevector

$$k_x = k\, n_1 \sin\alpha = \frac{2\,\pi}{\lambda} n_1 \sin\alpha \tag{1.14}$$

to match the wavevector necessary for SP excitation. In this way, any k_x between the two lines a and b can be set. This so-called *attenuated total reflection* (ATR) technique was first demonstrated by Kretschmann and Raether in 1968 [12] and has become the standard technique for SP excitation. Prism couplers, indeed, represent the most frequently used method for optical excitation of SPs. In the Kretschmann configuration (as shown in Figure 1.3) a light wave passes through a high refractive index prism and is totally reflected at the base of the prism, generate the evanescent wave to penetrate the thin metal film. The evanescent wave propagates along the interface with the propagation constant that can be adjusted to match that of the SP by controlling the angle of incidence or the light wavelength

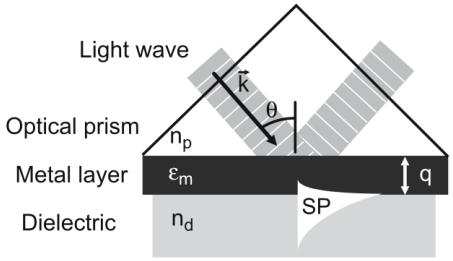

Figure 1.3: Excitation of surface plasmons in the Kretschmann geometry of the attenuated total reflection (ATR) method [13].

In a more real case, SPR-based sensors are systems made of more than three layers including the aqueous environment in which they are usually used. Depending on the substrate material, e.g., it can be necessary to use adhesion layers for the metal supporting SPR and to consider the biological medium that is supposed to be analysed in order to convert its thickness into surface concentrations. To study such a complex system Fresnel's eq. (1.7) can be applied repeatedly. The following relation holds for a system consisting of N layers with dielectric constants and thicknesses ϵ_i and d_i, respectively, placed between a prism with dielectric constant ϵ_p and a medium (e.g. water) with dielectric constant ϵ_w:

$$r_p(\alpha) = \frac{\left(M_{11} + M_{12}\frac{k_{y,w}}{\epsilon_w}\right)\frac{k_{y,p}}{\epsilon_p} - \left(M_{21} + M_{22}\frac{k_{y,w}}{\epsilon_w}\right)}{\left(M_{11} + M_{12}\frac{k_{y,w}}{\epsilon_w}\right)\frac{k_{y,p}}{\epsilon_p} + \left(M_{21} + M_{22}\frac{k_{y,w}}{\epsilon_w}\right)} \tag{1.15}$$

where M is the so-called transfer matrix:

$$M = M_1 \cdot M_2 \cdot ... \cdot M_N \tag{1.16}$$

with

$$M_i = \begin{bmatrix} \cos(k_{y,i}d_i) & \frac{-j\epsilon_i}{k_{y,i}}\sin(k_{y,i}d_i) \\ \frac{-jk_{y,i}}{\epsilon_i}\sin(k_{y,i}d_i) & \cos(k_{y,i}d_i) \end{bmatrix} \tag{1.17}$$

The dependence of r_p on α is implicit in the definition of $k_{y,i}$. Provided all thicknesses d_i and dielectric constants ϵ_i are known, eq. (1.15), (1.16) and (1.17) can give an accurate description of the SPR experiment.

1.3 SPR Sensors

The SPR phenomenon described in the previous sections can be exploited to make SPR sensors. Changes in the refractive index can be measured using the Kretschmann configuration (§1.2). By tuning the incident light wavelength and the angle of incidence it is possible to fulfill the coupling condition (eq. 1.14) that makes SPR possible. A change in the refractive index within the penetration depth of the evanescent wave implies a change in the incident light wavelength or angle to match the SPR condition. On the basis of which characteristic is measured

(change in the wavelength or angle, e.g., but also phase change can be measured), SPR sensors are classified in different ways. In this thesis work the sensor was used in the *wavelength modulation* configuration. In SPR sensors with wavelength modulation an SP is excited by collimated polychromatic light. The excitation of SPs is observed as a dip in the wavelength spectrum of reflected light (see 1.7, resonant case). A change in the refractive index is measured as the dip shift towards larger wavelengths if there is an increment of the refractive index or towards smaller wavelengths in the opposite case.

1.3.1 SPR Affinity Biosensor

An SPR affinity biosensor is a sensing device consisting of a SPR transducer capable of detecting a specific biological complex formation (see §1.4) and converting it into a signal which can be processed. For different specific binding events that one is concerned, different biorecognition elements must be used to functionalize the surface of a metal film supporting SPs. Analyte molecules in solution put on the SPR sensor bind to the biorecognition elements causing an increase in the refractive index at the sensor surface. The change in the refractive index produced by the binding event depends on the concentration of the analyte molecules at the sensor surface and the properties of the molecules. If the binding occurs within a thin layer at the sensor surface of thickness h, the sensor response is proportional to the binding-induced refractive index change, which can be expressed as [7]

$$\Delta n = \left(\frac{dn}{dC}\right)\frac{\Gamma}{h} \tag{1.18}$$

where $\left(\frac{dn}{dC}\right)$ denotes the refractive index increment of the analyte molecules (typically $0.1 - 0.3\ mL/g$) and Γ denotes the surface concentration in mass/area.

Among the characteristics of SPR biosensors [13], sensitivity and the limit of detection are the most used to quantify the sensor performance. For this reason only these will be discussed in more detail in the next subsections.

1.3.2 Sensitivity

Sensor sensitivity is the ratio of the change in sensor output to the change in the quantity to be measured (e.g., refractive index change or, more specifically, concentration of an analyte). The sensitivity of an SPR affinity biosensor, S_c, depends on two factors: sensitivity of the sensor output (e.g., resonant angle or wavelength) to a change in the refractive index and efficiency of the conversion of the binding event to a change in the refractive index [7].
Therefore it can be decomposed in two contributions:

$$S_C = \frac{\delta Y}{\delta n_b}\frac{\delta n_b}{\delta C} = S_{RI}S_{nc} \tag{1.19}$$

where S_{RI} denotes the sensitivity of the output, Y, to a refractive index change and S_{nc} is derived from the refractive index change (δn_b) caused by the binding of analyte (of concentration C) to biorecognition elements. S_{RI} can, in turn, be also broken down into two contributions:

$$S_{RI} = \frac{\delta Y}{\delta n_{ef}}\frac{\delta n_{ef}}{\delta n_b} = S_{RI,1}S_{RI,2} \tag{1.20}$$

where $n_{ef} = \frac{c}{\omega} k_x$ is the modal effective refractive index of the SP. The first term $S_{RI,1}$ depends on the method of excitation of SPs and the modulation approach used in the SPR sensor. $S_{RI,2}$ describes the sensitivity of the effective index of a SP to refractive index and is independent of the modulation method and the method of excitation of surface plasmons. It is clear at this point that S_C does not depend trivially on the refractive index change of the dielectric on top of the chip but on a series of aspects as the modulation configuration used and on how the the analytes in the solution bind to the functionalized surface. All these aspects have to be taken into account in order to characterize the sensor properly.

1.3.3 Limit of Detection and Minimum Resolvable Surface Coverage

The limit of detection (LOD) is derived from the smallest signal that can be detected with reasonable certainty for a given analytical procedure. It is the concentration at which we can decide whether an element is present or not [14] — that is, the point where we can just distinguish a signal from the background.
The minimum resolvable change of molecular mass captured by the biorecognition elements σ_Γ depends on the sensor sensitivity and the noise in the sensor output [7]:

$$\sigma_\Gamma = \frac{\sigma_{so}}{S_h} \frac{h}{\left(\frac{\delta n}{\delta C}\right)_{vol}} \tag{1.21}$$

where $\left(\frac{\delta n}{\delta C}\right)_{vol}$ denotes the volume refractive index increment of the molecular concentration, S_h denotes the refractive index sensitivity of sensor output to a refractive index change within the sensitive layer of a thickness h and σ_{so} denotes the standard deviation of noise of the sensor output. For thicknesses much smaller than the penetration depth of the surface plasmon ,L_{pd}, the following relationship holds: $\left(\frac{n_{ef}}{n_d}\right)_B = \left(\frac{\delta n_{ef}}{\delta n_d}\right)_S \frac{L_{pd}}{2h}$, and the resolution of surface coverage can be written as [7]

$$\sigma_\Gamma = \sigma_{RI} \frac{L_{pd}}{2\left(\frac{\delta n}{\delta C}\right)_{vol}} \tag{1.22}$$

where $S_h = \frac{\delta y}{\delta n_{ef}} \left(\frac{n_{ef}}{n_d}\right)_B$ and $\sigma_{RI} = \frac{\sigma_{so}}{S_{RI}}$.

For example, an SPR sensor operating at a wavelength of 760 nm ($L_{pd} = 320\ nm$) and a typical analyte with a refractive index increment $\left(\frac{\delta n}{\delta C}\right)_{vol} = 0.18\ cm^3/g$ (e.g. DNA) Eq.(1.22) suggests that a refractive index resolution of $\sigma_{RI} = 10^{-6}\ RIU$ corresponds to a surface coverage resolution of $\sigma_\Gamma = 0.91\ pg/mm^2$.

All these characteristics help in the evaluation of the performance of the sensor. Sensitivity should be as big as possible while LOD should be as small as possible in order to have a good SPR sensor. The process to enhance these characteristics will be discussed in the next sections.

1.4 Biosensing

1.4.1 Biorecognition Elements and Their Immobilization

In SPR affinity biosensors one of the interacting molecules (the biorecognition element or *ligand*) is immobilized on the metal layer of the SPR sensor while the other is immersed in a solution and placed on top in order to measure its concentration.

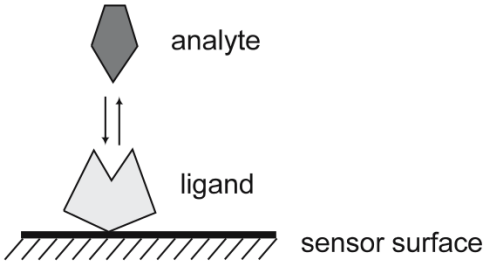

Figure 1.4: Schematic illustration of a ligand-analyte interaction on a sensor surface [13].

The choice of the biorecognition element is of critical importance. Not only it must be chosen so that it maximizes the covering of the sensing surface but the nonspecific bindings must also be minimized. Moreover, the immobilization must not affect the functional activity of the molecules. Evidently, the immobilization method depends on the experimental setup used because it affects key performance characteristic of the sensor such as sensitivity and LOD.

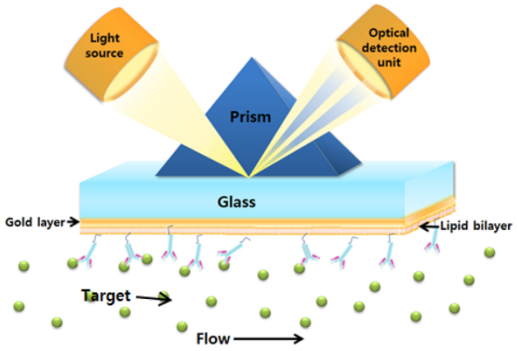

Figure 1.5: Schematic illustration of SPR detection in the Kretschmann configuration. A sensor chip measures the intensity of the reflection of the incident light due to the interaction between the biorecognition elements (green spheres) in the flow solution and the analytes (pink diamonds) [15].

For surface immobilization of biorecognition elements on the sensing surface, self-assembled monolayers (SAMs) of alkanethiolates or disulfides have been widely used [16]. Proteins, however, are the most frequently used biorecognition elements [7]. They are usually immobilized via a covalent bond formed between the nucleophilic functional groups supplied by amino acids (e.g., amino groups, lysine; thiol groups, cysteine) of the protein and electrophilic groups (e.g., activated carboxyls, aldehydes) on the sensor surface. The covalent immobilization is stable; however, as proteins typically contain many functional groups, immobilization via these functional groups results in random orientation of immobilized proteins. Another approach to the immobilization of proteins is based on biochemical affinity reaction. The most common example of this approach is the

immobilization based on avidin-biotin chemistry. In this immobilization method, protein avidin (or a closely related streptavidin) is immobilized on the sensing surface (covalently or via preimmobilized biotin) and provides binding sites for subsequent attachment of a biotin-conjugated protein (or viceversa). The protein can be biotinylated by various methods targeting different groups on the protein. Orientation of the immobilized proteins depends on the orientation of avidin/streptavidin molecules, the biotinylation method used, and the properties of the protein [7].

1.4.2 Biomolecular Interactions at Surfaces

Optical Quantification of Adsorption at an Interface

In SPR solution-based adsorption experiments the aim is usually to monitor the adsorption of an analyte in solution to the surface of a metal layer composed of a number of *binding sites*. The biorecognition elements bound to the metal surface exert an attractive force on the analyte. Once adsorbed to the surface the analyte is termed *the adsorbate*. As already stated in §1.3, the evanescent wave generated by the incident light at the metal-dielectric interface in, e.g., the Kretschmann configuration can probe change in the refractive index within the penetration length. For this reason the observed signal, S, follows the trend [8]

$$S \propto \int_0^\infty \delta n(y) e^{-\kappa_{y_2} y} dy, \tag{1.23}$$

where y is the distance normal to the surface and $\frac{1}{\kappa_{y_2}}$ is the characteristic length at which the amplitude of the electric field exponentially decaying along the y-direction. For planar surfaces it is typically of the order of $0.3 \div 0.5$ times the wavelength of the light used in the *total internal reflection* (TIR) experiment.
For a wide range of substances[2] the change in refractive index in response to the variation of the weight concentration of component i, c_i , can be approached as a linear function as the derivative $\frac{dn}{dC_i}$ is approximately constant,

$$n(C_i) = n(C_i = 0) + \frac{dn}{dC_i} C_i \tag{1.24}$$

Substitution of eq. (1.24) into eq. (1.23) allows us to relate the change in signal, ΔS, due to the weight concentration of component i at the interfacial layer, to situations in which initially no component i is present ($C_i = 0$), by

$$\Delta S \propto \frac{dn}{dC_i} \int_0^\infty \frac{dC_i}{dy} e^{-\kappa_{y_2} y} dy \tag{1.25}$$

On the basis of eq. (1.25), it can be deduced that the measured signal is, strictly, not a linear descriptor of the concentration of adsorbate, however for many cases it does approach a linear relationship.

[2]The approximate $\frac{dn}{dC}$ values for proteins and nucleic acids are 0.18 and 0.16 $ml\ g^{-1}$, respectively. The values for different types of carbohydrate range from 0.10 to 0.18 mlg^{-1}.

Analysis of Ligand–Receptor Interactions

For a simple bimolecular interaction with molecules A and B forming the complex AB

$$A + B \rightleftharpoons AB \tag{1.26}$$

the equilibrium association constant K_A and dissociation constant K_D are given by equations

$$K_A = \frac{[AB]}{[A][B]} \tag{1.27}$$

with K_A in l mol^{-1}, and

$$K_D = \frac{[A][B]}{[AB]} \tag{1.28}$$

with $K_D = \frac{1}{K_A}$ in mol l^{-1}. The brackets $[A]$, etc., indicate concentration of the molecules.
In a well-designed affinity experiment, several analyte concentrations are used, which should be in a range around the K_D value. In SPR experiments, [AB] and [B] are not approached as concentrations in solution, but as amounts at the surface expressed as SPR signal. The amount of complex AB is proportional to the shift in SPR angle which is expressed in millidegrees (m°) or in light wavelengths expressed in nm (for SPR sensors with angular or wavelength modulation, respectively). Frequently, the data (shift in SPR angle or wavelength), R_{eq}, are represented using the *Langmuir binding isotherm* in which [A] is the free analyte concentration and B_{max} is the maximum binding capacity in m° or nm, when all binding sites on the sensor surface are occupied:

$$R_{eq} = \frac{[A]}{[A] + K_D} B_{max} \tag{1.29}$$

In this way it is possible to fit the data with eq. (1.29), which can obtain the free analyte concentration or the dissociation constant (depending on the aim of the study).

Surface Acoustic Waves Microfluidics

2

2.1 Acoustic Waves

2.1.1 Wave Propagation in an Elastic Medium

An elastic medium behaves as a distributed mass-spring system in which displacement of a single element results in the propagation of a disturbance throughout the medium [17]. Different boundary conditions give rise to different modes of propagation of disturbance. Particles at a free surface, for example, are constrained by other particles from only one side and respond differently from the others that are situated inwards. In such a case unique modes of propagation exist. An elastic wave is the result of the interaction between elastic and inertial forces and its propagation depends not only on the boundary conditions but also on the properties of the medium that they pass through. Figure 2.1 shows schematically the waves that can propagate in an unbounded solid, a semi-infinite solid having a single plane boundary, and in a solid plate that has two plane boundaries.

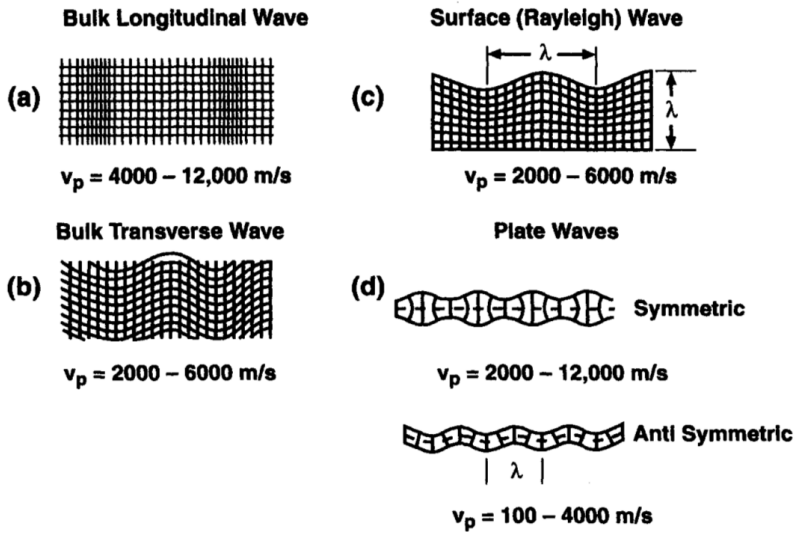

Figure 2.1: Schematics of elastic waves in solids. Typical wave speeds, v_p, are shown below each sketch. (a) Bulk longitudinal (compressional) wave in unbounded solid. (b) Bulk transverse (shear) wave in unbounded solid. (c) Surface acoustic wave (SAW) in semi-infinite solid, where wave motion extends below the surface to a depth of about one wavelength. (d) Waves in thin solid plates. [17]

Displacement, Stress and Strain

Application of a force to a solid causes stress to the solid (which is the force per unit area applied to the solid). Stress causes strain (the ratio of the length of the stressed material to its unstressed length) inside the solid: atoms or molecules of which the solid is composed are displaced from their unstressed position. Such a displacement can be described mathematically as a vector $\mathbf{u}(x, y, z, t)$ whose spatial components usually vary continuously within the solid. Let us consider a plane wave propagating along the x-direction. In this case the displacement vector can be written as

$$\boldsymbol{u} = (u_x\hat{\boldsymbol{x}} + u_y\hat{\boldsymbol{y}} + u_z\hat{\boldsymbol{z}})e^{j(kx-\omega t)} \tag{2.1}$$

in which u_x, u_y, and u_z represent particle displacements in the x, y, and z directions, respectively; $\hat{\boldsymbol{x}}$, $\hat{\boldsymbol{y}}$, and $\hat{\boldsymbol{z}}$ are unit vectors in their respective directions; ω is the angular frequency of the wave ($\omega = 2\pi f$, where f is frequency); $j = \sqrt{-1}$; and k is the wavenumber ($k = \frac{2\pi}{\lambda}$, where λ is wavelength). Figure 2.2 show a solid crystalline lattice perturbed by compressional and shear plane waves.

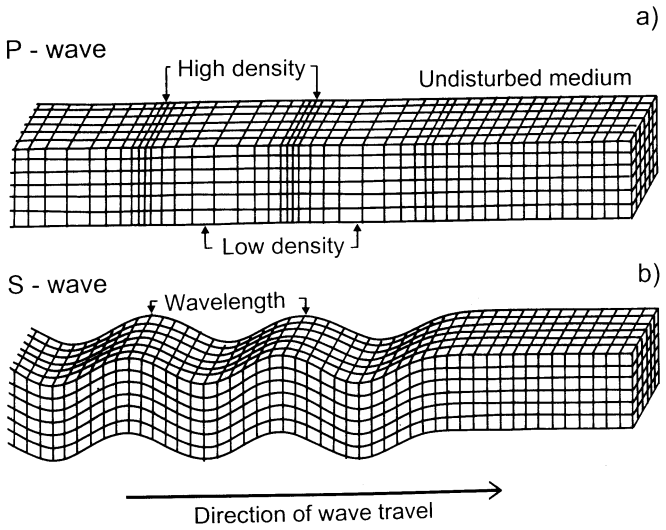

Figure 2.2: Plane waves propagating in a solid, showing compressional and shear waves.

A parameter used to describe such deformations is *the displacement gradient*, $\boldsymbol{\nabla u}$, which describes the local deformations of the solid. $\boldsymbol{\nabla u} = 0$ in case of translations which are not of interest for this kind of phenomenon. $\boldsymbol{\nabla u}$ is a second-rank tensor whose elements are given by $(\boldsymbol{\nabla u})_{ij} = \frac{\delta u_i}{\delta x_j}$, also denoted $u_{i,j}$ in which i denotes the i^{th} coordinate and j denotes a derivative with respect to the j^{th} spatial coordinate i.e.

$$\begin{pmatrix} \frac{\delta u_x}{\delta x} & \frac{\delta u_x}{\delta y} & \frac{\delta u_x}{\delta z} \\ \frac{\delta u_y}{\delta x} & \frac{\delta u_y}{\delta y} & \frac{\delta u_y}{\delta z} \\ \frac{\delta u_z}{\delta x} & \frac{\delta u_z}{\delta y} & \frac{\delta u_z}{\delta z} \end{pmatrix} \tag{2.2}$$

As with translations, global rotations are not of interest for this study and it is possible to write another parameter which describes only the local stretching of the solid: the strain matrix S (eq. 2.3).

$$\boldsymbol{S_{ij}} = \frac{1}{2}\left(\frac{\delta u_i}{\delta x_j} + \frac{\delta u_j}{\delta x_i}\right) \tag{2.3}$$

The diagonal strain terms (S_{ii}) represent *axial* or *compressional strains*, while the off-diagonal elements (S_{ij} with $i \neq j$) are *shear strains*. The shear strains physically represent the angular change (in radians) between elements initially in the i^{th} and j^{th} directions.
The strain can be written in matrix form as

$$\begin{pmatrix} S_{xx} & S_{xy} & S_{xz} \\ S_{yx} & S_{yy} & S_{yz} \\ S_{zx} & S_{zy} & S_{zz} \end{pmatrix} = \begin{pmatrix} S_1 & \frac{1}{2}S_6 & \frac{1}{2}S_5 \\ \frac{1}{2}S_6 & S_2 & \frac{1}{2}S_4 \\ \frac{1}{2}S_5 & \frac{1}{2}S_4 & S_3 \end{pmatrix} \tag{2.4}$$

by abbreviating subscripts [18] using the definition $p = \frac{1}{2}(i+j)(1-|sgn(i-j)|) + (-i-j+9)|sgn(i-j)|$, where i and j are subscripts that are combined to give a single subscript $p \in [1,6]$, $1 \leftrightarrow xx = (11)$, $2 \leftrightarrow yy = (22)$, $3 \leftrightarrow zz = (33)$, $4 \leftrightarrow yz = zy = (23) = (32)$, $5 \leftrightarrow xz = zx = (31) = (13)$, $6 \leftrightarrow xy = yx = (12) = (21)$.
By using equations (2.3) and (2.4), it is possible to write a relationship between strain and particle displacement:

$$\begin{bmatrix} S_1 \\ S_2 \\ S_3 \\ S_4 \\ S_5 \\ S_6 \end{bmatrix} = \begin{bmatrix} \frac{\delta u_x}{\delta x} \\ \frac{\delta u_y}{\delta y} \\ \frac{\delta u_z}{\delta z} \\ \frac{\delta u_y}{\delta z} + \frac{\delta u_z}{\delta y} \\ \frac{\delta u_x}{\delta z} + \frac{\delta u_z}{\delta x} \\ \frac{\delta u_x}{\delta y} + \frac{\delta u_y}{\delta x} \end{bmatrix} \tag{2.5}$$

In order to represent completely the state of stress at each point in a solid the stress tensor, $\boldsymbol{T}$, has to be used (eq. 2.6).

$$\begin{pmatrix} T_{xx} & T_{xy} & T_{xz} \\ T_{yx} & T_{yy} & T_{yz} \\ T_{zx} & T_{zy} & T_{zz} \end{pmatrix} = \begin{pmatrix} T_1 & T_6 & T_5 \\ T_6 & T_2 & T_4 \\ T_5 & T_4 & T_3 \end{pmatrix} \tag{2.6}$$

Each element of the stress tensor, $\boldsymbol{T_{ij}}$, represents the i^{th} component of force per area acting on the j^{th} face of an infinitesimal volume element.
Hooke's law

$$T_{ij} = c_{ijkl} S_{kl} \tag{2.7}$$

(in which c_{ijkl} are the *elastic stiffness constants*) describes what strain results from a given stress. Due to symmetry $c_{ijkl} = c_{jikl}$ and $c_{ijkl} = c_{ijlk}$. For this reason it is possible to write the fourth-order elastic stiffness tensor as a 6x6 matrix

$$T_I = \sum_{J=1}^{6} c_{IJ} S_J \tag{2.8}$$

The equation of motion for stress to particle displacement in a non-piezoelectric solid is

$$\boldsymbol{\nabla} \cdot \boldsymbol{T} = \rho_s \frac{\delta^2 \boldsymbol{u}}{\delta t^2} \tag{2.9}$$

where ρ_s is the material's mass density and t is time.

The wave equation

From the equation of motion (2.9) and the Hooke's law (2.7) it is possible to derive *the wave equation* which describes the propagation of plane acoustic waves in a non-piezoelectric solid:

$$\rho_s \frac{\delta^2 u_i}{\delta t^2} = \sum_{j,k,l=1}^{3} c_{ijkl} \frac{\delta^2 u_k}{\delta x_j \delta x_l} \tag{2.10}$$

In general, the solution to the previous equation consists of three propagating wave types: a *quasi-compressional wave*, whose principal polarization (the direction of particle displacement) lies along the direction of propagation, and two *quasi-shear waves*, each of whose principal polarizations is perpendicular to the propagation direction, as indicated in Figure 2.2.

2.1.2 Piezoelectricity

Application of an electrical field to a non-piezoelectric dielectric elastic solid would have no effect on its mechanical stress-strain characteristics. However, the coupling between strain and electrical polarization that occurs in many crystals makes the electric generation of acoustic waves possible. In the absence of a center of inversion symmetry (with the property that a straight line drawn from any point in the lattice through the center of inversion will meet an equivalent point at an equal distance from that center) the application of strain onto a crystal changes the charge distribution giving rise to a net, macroscopic, electrical polarization of the crystal. Such piezoelectric crystals also exhibit the opposite effect, by which the application of an electric field causes strain onto the crystal. By modifying eq. (2.8) and the electromagnetic constitutive relations it is possible to describe mathematically the interaction between the electric field, strain and stress in the case of piezoelectric solid materials and write the *piezoelectric constitutive relations*[1]:

$$T_I = c_{IJ}^E S_J - e_{Ij} E_j \tag{2.11}$$

$$D_i = \epsilon_{ij}{}^S E_j - e_{iJ} S_J \tag{2.12}$$

in which e_{Ij} are the piezoelectric stress constants, having units of $charge/(length)^2$, E_i are the electric field components, D_i are the electrical displacement components, and ϵ_{ij} are the permittivity constants.
The piezoelectric stress matrix (e_{Ij}) is a third-rank tensor, therefore 18 piezoelectric constants are necessary to characterize a piezoelectric material in the most general case. Piezoelectric constants for various crystal classes are shown in Table 2.1.
As is clear from equations (2.11) and (2.12) the elastic and electromagnetic fields are coupled in a piezoelectric substrate. By solving these equations it can be seen that the velocity of the electromagnetic wave is five orders of magnitude faster

[1] Summation over the repeated indices is assumed

		Piezoelectric Stress Constants (C/m^2)					
Material	Simmetry Class	e_{x1}	e_{x4}	e_{x5}	e_{y2}	e_{z1}	e_{z3}
Gallium Arsenide	Trig. 3 m		0.154				
Lithium Niobate	Trig. 32			3.7	2.5	0.2	1.3
Quartz	Hex. 6 mm	0.171	−0.0436				
Zinc Oxide	Cub. 43 m			−0.48		−0.573	1.32

Table 2.1: Piezoelectric Stress Constants [17]

than the elastic wave. Therefore, the mechanical dynamics can be treated as quasi-static:

$$\frac{\delta \boldsymbol{D}}{\delta t} = \boldsymbol{\nabla} \times \boldsymbol{H} = 0 \tag{2.13}$$

thus simplifying equation (2.12). Equations (2.3), (2.9), (2.11), (2.12), and (2.13), form a complete set for analysis of acoustic wave propagation in piezoelectric solids.

In a piezoelectric medium the elastic stiffness constants (seen the first time in eq. 2.7) result in an increase of a factor $\left(1 + K^2\right)$ known as *piezoelectric stiffening*. For *surface acoustic wave* (SAW) propagation in piezoelectrics it may be demonstrated that

$$K^2 = \frac{e^2}{c\epsilon}, \tag{2.14}$$

where e is the piezoelectric coefficient, c the elastic constant and ϵ the dielectric permittivity. Appropriate constants depend on both the crystal cut and the propagation direction of the surface acoustic wave.
K^2 is the *electromechanical coupling coefficient* and it is a numerical measure of the conversion efficiency between electrical and acoustic energy in piezoelectric materials. In Table 2.2 coupling coefficients for some standard piezoelectric media are shown. Crystal cuts and SAW propagation direction are specified due to the fact that K^2 depends on both these properties.

Material	Crystal Cut	SAW axis	v_{SAW} [m/s]	K^2[%]
Lithium Niobate	127.86°Y	X	3980	5.5
Lithium Niobate	Y	Z	3488	4.5
Quartz	Z	X	3160	0.14
Lithium Tantalate	X	112.2°Y	3290	0.75

Table 2.2: Typical substrates used for SAW devices. Cut direction, SAW propagation direction, SAW velocity and electromechanical coupling coefficient are shown for each crystal [19] [20] [21] [22].

2.1.3 Power Dissipation in a Lossy Medium

The acoustic wave amplitude decreases as the wave propagates in a real crystal as a result of several loss mechanisms such as scattering or thermoelastic attenuation. The latter is proportional to the thermal conductivity of the solid and it is therefore really important in metals whereas the dominant loss mechanism is phonon

scattering (that can be treated phenomenologically by introducing a viscous term into the elastic constitutive relation for the solid, eq. 2.8) in insulators.
From conservation of energy, the power dissipated by the wave P_d (power/volume) must be balanced by a reduction in power transmitted by the wave P. If the wave is propagating in the x direction, then

$$P_d = -\frac{\delta P}{\delta x} \tag{2.15}$$

Since energy density and power flow are proportional to the square of wave amplitude, in a lossy medium, following the *Stokes' law of acoustic attenuation* [17], it is possible to write

$$P(x) = P_0 e^{-2\alpha x} \tag{2.16}$$

so that

$$\frac{\delta P}{\delta x} = -2\alpha P \tag{2.17}$$

from which follows

$$\alpha = \frac{P_d}{2P} \tag{2.18}$$

Equation 2.18 indicates the relationship between wave attenuation and power dissipation in the medium: attenuation is the ratio of power dissipated to half the power transmitted by the wave.

2.2 Surface Acoustic Waves (SAWs)

2.2.1 SAW equation

The stress-free boundary condition for the surface of a crystal gives rise to a particular acoustic mode whose propagation is confined to the surface and is therefore known as a SAW.
In 1885 Lord Rayleigh discovered this mode of propagation in which acoustic energy is confined to the surface of an isotropic solid [23]. Such wave motion, now known as the *Rayleigh wave*, is of interest to seismologists because it is excited by earthquakes. In order to satisfy the stress-free boundary condition, coupled compressional and shear waves propagate together in a SAW such that surface traction forces are zero. The generalized SAW, propagating in the x-direction, has a displacement profile $u(y)$ that varies with depth y into the crystal as

$$\mathbf{u}(x,y,z) = \left[(u_x(y)e^{j\phi_1}\hat{\mathbf{x}} + u_y(y)e^{j\phi_2}\hat{\mathbf{y}} + u_z(y)e^{j\phi_3}\hat{\mathbf{z}}) \right] e^{j\omega t - \gamma x} \tag{2.19}$$

where ω is the angular frequency ($2\pi f$); $\gamma = \alpha + ik$ is the complex propagation factor representing both attenuation and wavenumber; u_x, u_y, and u_z represent displacement components in the x-, y-, and z-directions, respectively, and ϕ_i the phases of the components with respect to u_x. The component u_y is perpendicular to the surface, u_x is in the direction of propagation, and u_z is transverse to the yx plane (i.e., *the sagittal plane*).

The displacement components $u_i(y)$ vary approximately as $e^{-\frac{2\pi y}{\lambda}}$, where λ is the SAW wavelength along the surface and y is the distance into the substrate; the amplitude thus decays rapidly with distance into the bulk of the crystal. A cross-sectional view of the strain field generated by a surface wave propagating along the surface of a crystal is shown in Figure 2.3.

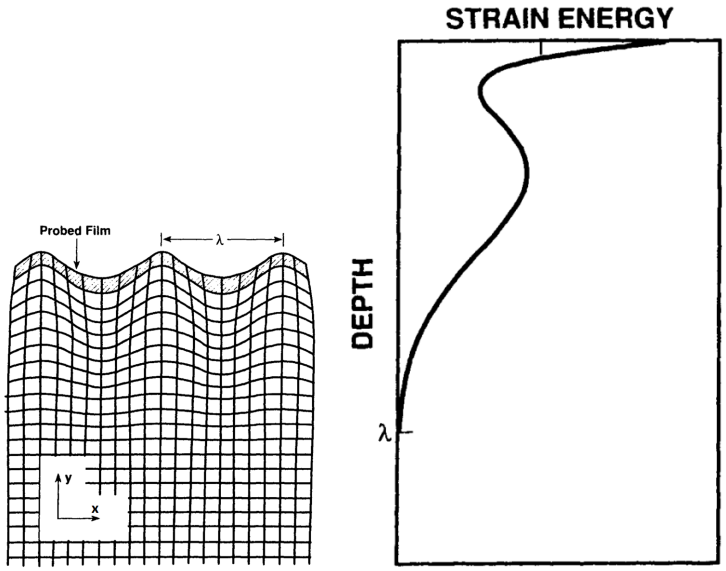

Figure 2.3: Deformation field due to a SAW propagating to the right along a solid surface (left) and the associated distribution of potential energy (right). [17]

In the figure above the *energy strain density* is also shown, indicating that the majority of wave energy is contained well within one wavelength of the surface, which thus acts as a waveguide. At higher frequencies acoustic energy is confined more closely to the surface and wave sensitivity to surface perturbations increases.
The instantaneous energy strain density (energy per volume) is given by

$$U_S = \sum_{I,J=1}^{6} \frac{1}{2} S_I c'_{IJ} S_J = \sum_{i,j,k,l=1}^{3} c'_{ijkl} \frac{\delta u_i}{\delta x_j} \frac{\delta u_k}{\delta x_l} \tag{2.20}$$

where c' denotes the *piezoelectrically stiffened elastic constants* in piezoelectric materials ($c' = c(1 + K^2)$), already mentioned in §2.1.2. Thus, the strain energy in this case includes stored electrical energy.

For propagation in an isotropic medium or along a pure-mode direction of a crystal (e.g., a plane of symmetry), eq. (2.19) reduces to a Rayleigh wave, characterized by having no transverse component: $u_z = 0$. Since u_y and u_x are $\frac{\pi}{2}$ out of phase, the particles move in an elliptical orbit in the sagittal plane and the surface motion looks like that of the ocean during the propagation of a wave. When the SAW medium is contacted by a liquid, the surface-normal displacement component generates compressional waves in the liquid and the power dissipated in this way leads to excessive attenuation of the SAW.

2.2.2 SAW excitation

SAWs are usually excited using *interdigital transducers* (IDTs) on a piezoelectric crystal as shown in Figure 2.5.

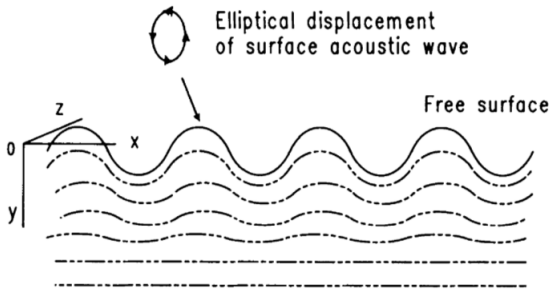

Figure 2.4: Schematic depiction of surface acoustic wave motion on the surface of an elastic solid. Modified from [24].

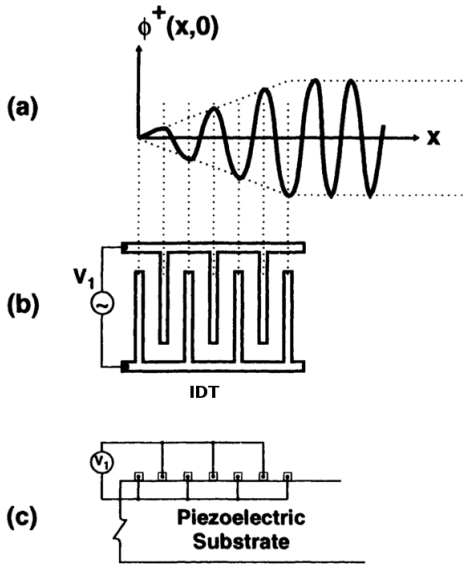

Figure 2.5: Interdigital transducer, formed by patterning electrodes on the surface of a piezoelectric crystal, for exciting surface acoustic waves: (a) SAW electrical potential, (b) plan view, (c) side view. Modified from [17]

A periodic electric field is generated on the crystal by the application of an alternating voltage on a pair of comb-shaped electrodes. Due to the piezoelectricity of the crystal, the electric field causes a periodic strain field to generate a standing SAW. The propagating waves generated in this way are launched in both directions away from the transducer with the wavefronts parallel to the transducer fingers. The most efficient configuration occurs when the SAW wavelength λ matches the transducer periodicity d. This happens when the transducer is excited at the synchronous frequency $f_0 = \frac{v_{sound}}{d}$ (where v_{sound} is the SAW propagation velocity along a given substrate).

Interdigital Transducer Frequency Response

Each finger of the comb-shaped electrodes may be considered as a discrete source for the generation of a SAW on the piezoelectric substrate. A transfer function relates the continuous wave voltage V_1 applied to a finger and the electrical potential

associated with the waves radiated in each direction

$$\phi^{\pm} = \mu_s V_1 \tag{2.21}$$

where μ_s is a substrate-dependent and frequency-independent constant, (ϕ^+ is associated with the rightward propagating SAW, while ϕ^- is a leftward propagating SAW). When an array of fingers is excited, the wave potential for a rightward propagating wave ϕ^+ at a position x is a vector sum of the contributions from each finger:

$$\phi^+(x) = \mu_s \sum_{n=0}^{N_f-1} V_n e^{jk(x-x_n)} \tag{2.22}$$

where x_n is the position of the n^{th} finger excited with voltage V_n; N_f is the total number of fingers. Equation 2.22 has the form of a discrete Fourier transform of the sequence V_n.
If N_f identical fingers are spaced periodically with period d and excited with alternating voltages $V_n = (-1)^n V_0$, Equation 2.22 becomes

$$\phi^+(0) = \mu_s V_0 \sum_{n=0}^{N_f-1} (-1)^n e^{\frac{jknd}{2}} \tag{2.23}$$

The sum in eq. (2.23) is a geometric series whose elements become unity, and add constructively, when $\frac{kd}{2} = m\pi$, where m is an odd integer. This condition defines the relationship between SAW wavelength and transducer periodicity for coherent addition, as shown in Figure 2.6. The IDT excites odd harmonics at odd multiples of the synchronous frequency: $f_m = mf_0$.

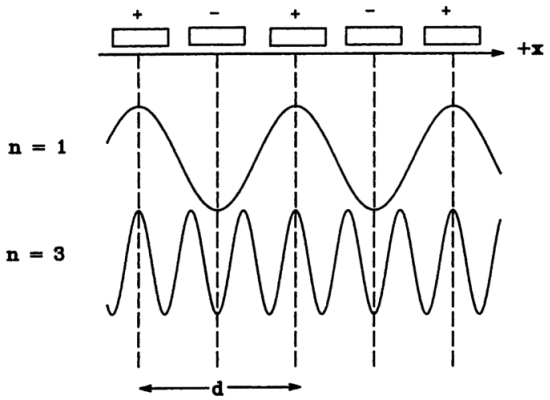

Figure 2.6: Relationship between transducer periodicity and coherently excited waves. [17]

Drifting away from the synchronous frequency, the sum becomes incoherent and causes the frequency response

$$|\phi^+(f)| = |\frac{\sin(X)}{X}| \tag{2.24}$$

in which

$$X = \frac{N_p \pi (f - f_0)}{f_0} \tag{2.25}$$

where f_0 is the transducer's synchronous frequency and N_p is the number of IDT periods $\left(N_p = \frac{N_f}{2}\right)$. The wave potential as a function of the *detuning parameter* X, described by Equation 2.25, is shown in Figure 2.7.

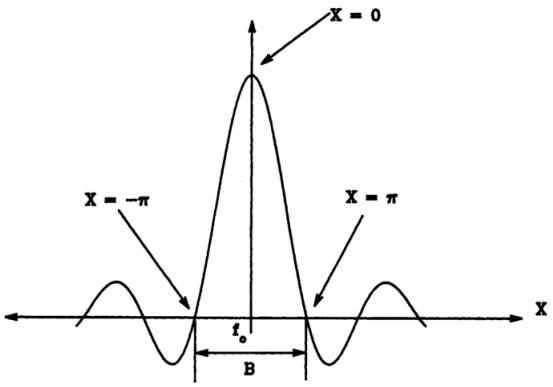

Figure 2.7: Transducer response, $\frac{sin(X)}{X}$, vs the "detuning parameter" X. [17]

It can be seen that when X is a multiple of π, ϕ^+ is zero. Consequently, the frequency interval B between the first nulls on either side of the synchronous frequency is

$$B = \frac{2}{N_p} \tag{2.26}$$

Thus, the transducer bandwidth B is inversely proportional to the number of IDT fingers and can be therefore made as narrow as possible increasing N_p.

2.3 Acoustic Streaming in Microfluidic Devices

2.3.1 Equations for Fluid Motion

To describe the motion of a viscous fluid it is necessary to modify the equation of motion of ideal fluids. The equation of continuity

$$\frac{\delta\rho}{\delta t} + \bigtriangledown \cdot (\rho \boldsymbol{v}) = 0 \tag{2.27}$$

holds either for viscous fluids or not. Euler's equation, on the other hand, requires modification. It can be written in the form

$$\frac{\delta(\rho \boldsymbol{v}_i)}{\delta t} = \frac{\delta \prod_{ik}}{\delta x_k} \tag{2.28}$$

where $\delta\prod_{ik} = p\delta_{ik} + \rho v_i v_k$ is the *momentum flux density tensor*.
The momentum flux is a reversible mechanical transfer of momentum (due to pressure forces and movement of fluid particles) while the viscosity is due to an irreversible transfer of momentum (from points where the velocity is large to those where it is small). The equation of motion of a viscous fluid may therefore be obtained by adding to the "ideal" momentum flux of eq. (2.28) a term $-\sigma'_{ik}$ which gives the irreversible "viscous" transfer of momentum in the fluid.
The general form of the tensor σ'_{ik} can be established as follows [25]. Internal

friction occurs in a fluid only when there is a relative motion between various parts of the fluid. Hence σ'_{ik} must depend on the space derivatives of the velocity. If the velocity gradients are small we may suppose that the momentum transfer due to viscosity depends only on the first derivatives of the velocity. For this reason σ'_{ik} may be supposed a linear function of the derivatives $\frac{\delta v_i}{\delta x_k}$. There can be no terms in σ'_{ik} independent of $\frac{\delta v_i}{\delta x_k}$ since σ'_{ik} must vanish for $v = constant$. Next, σ'_{ik} must also vanish when the whole fluid is in uniform rotation since in this case no internal friction occurs in the fluid.
The most general and convenient tensor of rank two which satisfies the above conditions is

$$\sigma'_{ik} = \eta \left(\frac{\delta v_i}{\delta x_k} + \frac{\delta v_k}{\delta x_i} - \frac{2}{3}\delta_{ik}\frac{\delta v_l}{\delta x_l} \right) + \zeta \delta_{ik}\frac{\delta v_l}{\delta x_l} \tag{2.29}$$

where the expression in parentheses has the property of vanishing on contraction with respect to i and k. The constants η and ζ are called *coefficients of viscosity* and are both positive. These quantities are in general functions of pressure and temperature and therefore they are not constant throughout the fluid. In most cases, however, the viscosity coefficients do not change noticeably in the fluid and they may be regarded as constants. Hence the equation of motion of a viscous fluid can be written, in vector form, as

$$\rho \left[\frac{\delta \boldsymbol{v}}{\delta t} + (\boldsymbol{v} \cdot \bigtriangledown)\boldsymbol{v} \right] = - \bigtriangledown p + \eta \bigtriangleup \boldsymbol{v} + \left(\zeta + \frac{\eta}{3} \bigtriangledown \bigtriangledown \cdot \boldsymbol{v} \right) \tag{2.30}$$

In the case of incompressible fluid ($\bigtriangledown \cdot \boldsymbol{v} = 0$) by adding $-\sigma'_{ik}$ to the ideal momentum flux of eq. (2.28) the *Navier-Stokes equation* can be obtained:

$$\frac{\delta \boldsymbol{v}}{\delta t} + (\boldsymbol{v} \cdot \bigtriangledown)\boldsymbol{v} = -\frac{1}{\rho} \bigtriangledown p + \frac{\eta}{\rho} \bigtriangleup \boldsymbol{v} \tag{2.31}$$

Lighthill [26] rewrote the Navier-Stokes equation highlighting that the presence of turbulence is typically coupled to structural vibrations of the fluid (the so called *Lighthill's aeroacoustic analogy*). Importantly, he also recognized that the converse situation can occur [27]: the propagation of sound through a fluid can generate bulk flow that can become turbulent. The acoustic wave transmits momentum flux into the fluid. Thus, this local oscillatory momentum flux results in a macroscopic fluid motion thanks to viscous dissipation.

2.3.2 Acoustic Streaming at Low Reynold's Numbers

The Reynolds number is defined as

$$Re = \frac{l \rho v}{\eta} \tag{2.32}$$

(where l is a characteristic linear dimension). This dimensionless number is the ratio of inertial to viscous forces. Hence, a low Reynolds number is to some extent equivalent to an increase of the apparent viscosity, which significantly influences the hydrodynamic behaviour of a liquid. As turbulent flow only occurs at high Reynolds numbers (> 2000), the typically low Reynolds number in microfluidic systems leads to laminar flow, which is typically associated to long mixing times. Therefore, the only way for small fluid volumes to mix effectively is by diffusion.

Here, the smallness of the system is in fact in favour of the diffusion limited time scales, as the respective length scales are equally small. However, for many applications, especially in so-called biochips or microarray based assays, a deliberate and controlled agitation of the fluid under investigation is of great importance to speed up unreasonable long mixing times.
By giving rise to second order effects, SAWs can induce streaming in microfluidic systems at low Re [28]. Consider a quiescent liquid, which before the presence of any acoustic wave has constant density ρ_0 and pressure p_0. Let an acoustic wave constitute tiny perturbations (subscript 1 and 2, first and second order, respectively) in the fields of density ρ, pressure p, and velocity v,

$$\rho = \rho_0 + \rho_1 + \rho_2 \quad , \quad p = p_0 + p_1 + p_2 \quad \text{and} \quad v = 0 + v_1 + v_2 \tag{2.33}$$

By inserting equations (2.33) in eq. (2.30), the Navier-Stokes equation becomes:

$$\rho_0 \left[\frac{\delta \boldsymbol{v_2}}{\delta t} + (\boldsymbol{v_1} \cdot \bigtriangledown)\boldsymbol{v_1} \right] = - \bigtriangledown p_2 + \eta \bigtriangleup \boldsymbol{v_2} + \left(\zeta + \frac{\eta}{3} \bigtriangledown \bigtriangledown \cdot \boldsymbol{v_2} \right) - \rho_1 \frac{\delta \boldsymbol{v_1}}{\delta t} \tag{2.34}$$

As the Navier–Stokes equation is nonlinear, the first-order fields calculated cannot in general be an exact solution and the second order field must be considered. Normally, the second-order fields would be negligible compared to the first-order fields. However, if the latter (as they do) have a harmonic time dependence then they do not contribute to any time-averaged effect whereas the time-averaged second-order fields will in general be non-zero. In that case the term $(\boldsymbol{v} \cdot \bigtriangledown)\boldsymbol{v}$ is no long negligible and acoustic streaming is possible (see Lighthill theory, §2.3.1).
The dynamics of a small volume element within a fluid, through which an acoustic wave propagates, can be defined by pressure and velocity oscillations. In an ideal fluid the time-averaged displacement of the volume element is zero. However, in a real fluid such as water, viscous attenuation results in a net displacement of the volume element during each cycle of oscillation as a direct result of the diminishing amplitude of its oscillation. The net displacement of many such volume elements in the fluid manifests itself as a global streaming flow.
SAW-induced Eckart streaming (among the different kinds of streaming that can occur in microfluidics systems) was exploited for this thesis work. Eckart streaming is the flow formed by the dissipation of acoustic energy into the bulk of a fluid (following Stokes' law of sound attenuation). The loss of acoustic energy results in a steady momentum flux, forming a jet of fluid inside the acoustic beam in the direction of acoustic propagation [29]. Eckart streaming can occur in microfluidic devices only if the chamber dimension parallel to the acoustic wave propagation direction is comparable to or greater in length than the acoustic attenuation length [30] (1 mm or more for frequencies of about 50 MHz, as in this thesis work).

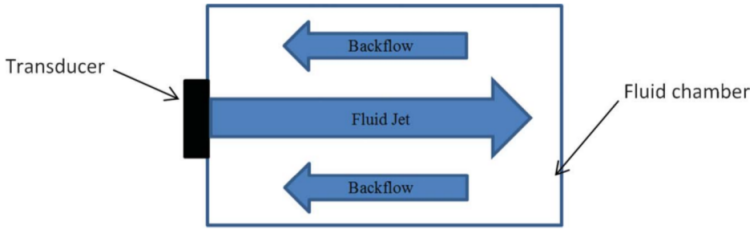

Figure 2.8: A typical Eckart streaming flow including a backflow that arises due to the confined region [30].

In particular when the SAW comes into contact with the edge of the liquid, the acoustic energy refracts into the fluid due to the mismatch between the sound velocity in the substrate, c_s, and that in the liquid, c_l ($\approx$ 1485 m/s for water), as shown in Figure 2.9. The angle at which the SAW diffracts into the fluid is given by the ratio between the sound velocities:

$$\theta_R = \sin^{-1}\left(\frac{c_l}{c_s}\right) \approx 22^{\circ}C \tag{2.35}$$

The SAW refracted at θ_R has an *attenuation length* given by

$$x_s = \lambda_{SAW}\frac{c_s\rho_s}{c_l\rho_l} \tag{2.36}$$

where λ_{SAW} is the SAW wavelength and ρ_s and ρ_l are the density of the substrate and of the fluid, respectively. This energy transfer into the liquid causes a longitudinal pressure wave front that gives rise to the acoustic streaming.

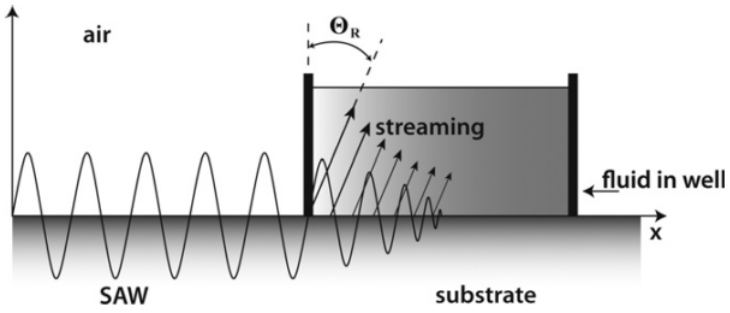

Figure 2.9: Schematic illustration showing the energy of the surface acoustic wave radiating into a fluid well at the Rayleigh angle θ_R and driving bulk recirculation (acoustic streaming) in the fluid (not to scale) [5].

The complex streaming patterns arising from the interaction between the SAW and a fluid on top of the substrate can be used for efficiently mixing small quantities of liquid.

Strobl et al. [4] showed first in 2002 that it was possible to make a novel microfluidic technology meeting the basic requirements for a microfluidic processor analogous to those of its electronic counterpart and that SAW could have an important role in this. Among different applications, they studied the mixing induced in a 5 μL-droplet. They made devices (of which a schematic representation in shown Figure 2.10) with IDTs exciting SAW at different frequencies (from 114 MHz to 800 MHz) onto a 128°-rot lithium niobate (LN) substrate at different RF powers (from -15 dBm to 30 dBm). A fluorescent dye was dissolved in the water droplet in order to visualize the fluid flow. Mixing was then observed with a CCD camera. They showed that the duration of the mixing experiment, going from minutes to tens of μs, inversely depended on the RF power (-12 dBm was the minimum RF power for mixing). They also showed that different SAW frequencies induced

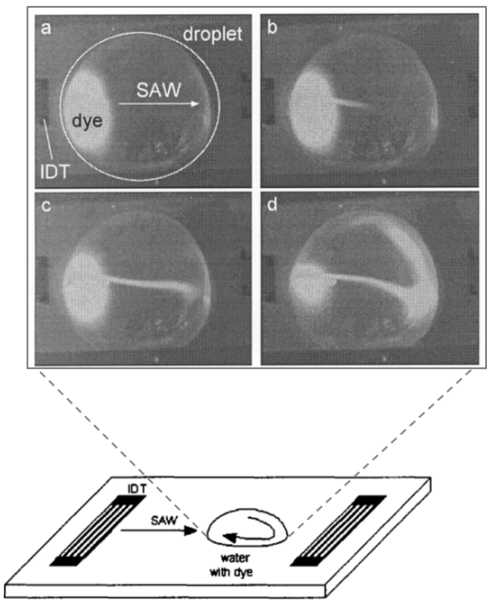

Figure 2.10: Schematic of the setup of Strobl et al. chip with an illustration of the mixing experiment they made. A 5 μL-droplet is shown while the fluorescent dye mixes because of the 114 MHz-SAW, propagating from left to right. IDT was fed by $-3.5\ dBm$ RF power. On top, Figure (a) shows the beginning of the experiment, (b) 240 ms after starting mixing, (c) after 1 sec and (d) after 5 sec. Modified from [4]

different shapes of the fluid flow. Some images of the experiment are shown in Figure 2.10. The first experimental quantification of the mixing phenomenon was made by Shilton et al. in 2011 [5]. They generated fast mixing flows in a microfluidic steel well using 20 MHz SAWs on a 128°-rot LN substrate (shown in Figure 2.11). The fluid in the well (volume of 2.5 μL) comprised a mixture of glycerol and water at varying ratios to alter the viscosity of the fluid. Fluorescent, 5 μm polystyrene particle suspensions were introduced in the fluid to aid the flow visualization made with a video camera. They showed that the strongest mixing flows were most evident at higher SAW excitation amplitudes and studied the effect of viscosity on streaming, showing that increases in viscosity essentially suppressed the chaotic advection and hence the mixing effect.

In order to better confine the working fluid and manipulate it, SAW technologies have been integrated into microfluidic channel systems. One of the first studies of mixing in a microchannel was made by Tan et al. in 2009 [31]. They cut 10 mm long and 180 μm deep microchannels of different widths W_{ch} (from 30 μm to 280 μm) with a 248 nm-laser into a 128°-rot LN substrate (see Figure 2.12). SAWs were excited at 20 MHz and 30 MHz by a pair of IDTs. The microchannel was filled with a deionized aqueous homogeneous suspension of either 500 nm- or 1 μm-diameter spherical fluoroscent polystyrene particles and the flow behaviour in the channel was determined using microscopic flow visualization. They showed that as the width of the channels was increased, the flow became progressively irregular at a constant input power (Figure 2.12 (a), (b), (c), (d)). In both cases, 20 MHz

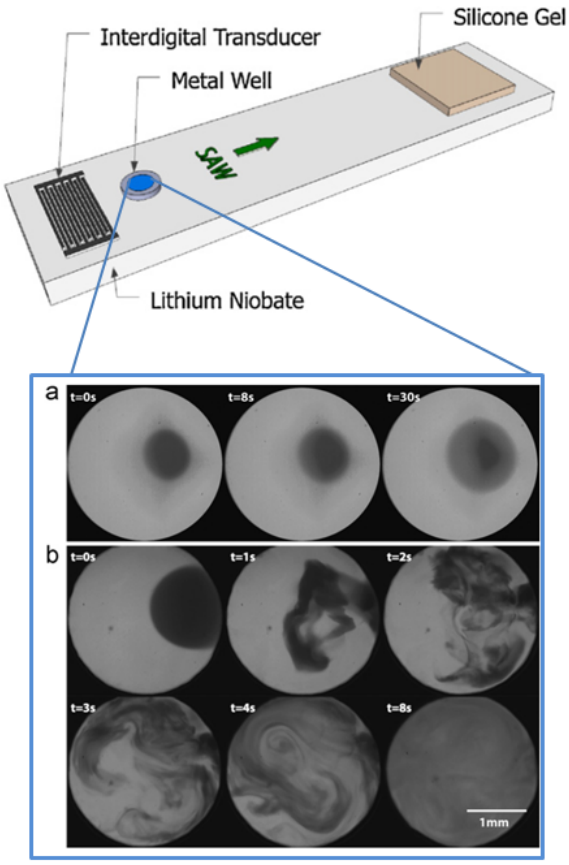

Figure 2.11: Schematic depiction of Shilton at al. SAW device. Images below show (a) mixing due to pure diffusion in absence of SAW, and (b) mixing under chaotic flow conditions driven by the SAW. Modified from [5].

and 30 MHz, the flow irregularities appeared when $W_{ch} > \lambda_{SAW}$. Moreover, flow streaming velocities were found to be lower in the plane C-C, deeper in the channel.

Luong et al. (2010) [32], made micromixers based on SAW streaming on a device with polydimethylsiloxane (PDMS) microchannels bonded on a 128°-rot LN substrate (Figure 2.13) in order to allow mixing in continuous flow (which was not possible in the Tan et al. device). Flow rates of 2, 5 and 10 mL/h were investigated. As in the other cited cases, water and fluorescent dye solutions in a side-by-side configuration (Figure 2.13 (a)) were used for the experiment and a CCD was used to capture the images at the end of the channel (10 mm away from the inlet of the channel where syringes with pumps were connected). They showed that by using IDTs with focusing electrodes [33] instead of parallel electrodes (both configurations are showed in Figure 2.13 (b) and (c)) the mixing efficiency could be improved from 0.5 to 0.78.

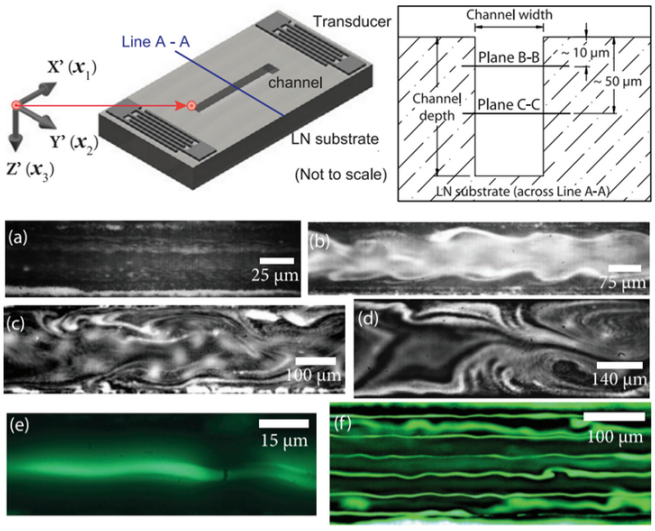

Figure 2.12: Image shows the Tan et al. device with the cut channel in detail (on the right). Images (a)-(d) show typical flow behaviour along plane B-B in $W_{ch} = 50, 150, 200, 280\ \mu m$ wide microchannels with 20 MHz-SAW. Images (e) and (f) were made along the plane C-C ina 30 μm and 200 μm channel width, respectively under 30 MHz SAW excitation. Modified from [31].

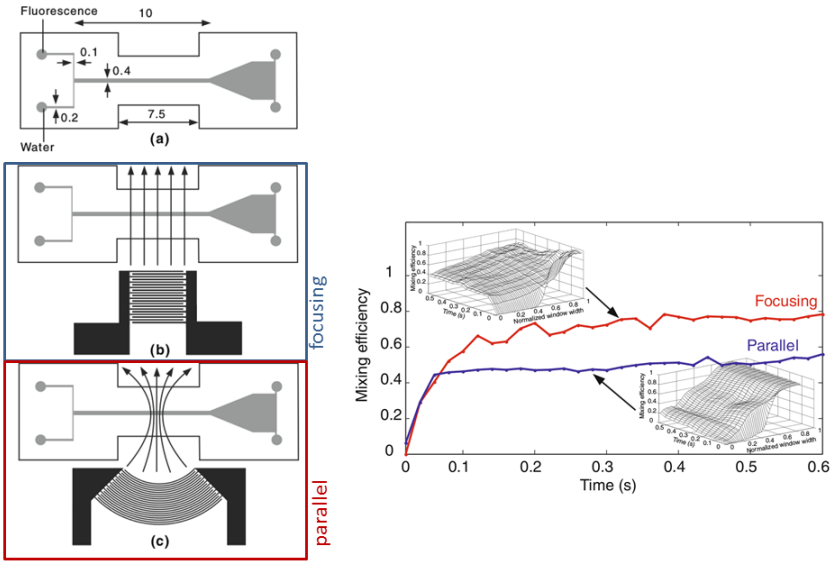

Figure 2.13: On the left, geometry of Luong et al. SAW micromixer (a), with parallel (b) and focusing (c) IDT. On the rifght, mixing efficiency as function of time for the focusing (red line) and parallel (blue line) design. The insets are the corresponding normalized intensity values. Modified from [32].

Renaudin et al. [6] were the first to exploit SAW-driven active mixing in a biosensor by integrating both SAW and SPR on a common substrate. SPR affinity biosensors are widely used for the detection and analysis of biomolecular interactions. They are label-free, (i.e. no fluorescent tagging is required), real-time (allowing reaction kinetics to be measured), can be implemented in parallel (allowing high-throughput screening and the use of multiple targets), and can provide quantitative measurements. The main issues that, at the moment, limit SPR biosensor sensitivity and LOD are are non-specific adsorption and mixing limitations. *Non-specific adsorption* is the weak binding of molecules other than the target analyte to the sensing surface, for example via long-range coulombic interactions. In the best case, this causes false positives and/or errors in the determination of concentration. In the worst case, the nonspecifically adsorbed molecules can completely obscure the surface-bound ligands. Moreover, microfluidics systems are used for SPR analysis in order to minimize the quantity of expensive reagents to be used, however, as already seen, they are characterized by $Re << 1$ and consequently by laminar fluid flow where efficient mixing is a challenge. Renaudin et al. tried to overcome these problems by designing and fabricating a biosensor (see Figure 2.14) where a 20 MHZ golden IDT and SPR golden surface where made on the same 128°-rot LN substrate (gold thickness of 48 nm). A microfluidic teflon well was clamped on top of the SPR sensing surface. The chip was used in the Kretschmann configuration on an SF10 glass ($n = 1.723$) coupling prism with index matching fluid ($n = 1.735$), and collimated light from a linearly-polarized 4 mW laser diode (635 nm) was used to excite the SP. S-polarization (that can not excite SPs) was used as a reference to remove time-dependant noise sources, as well as for normalization.

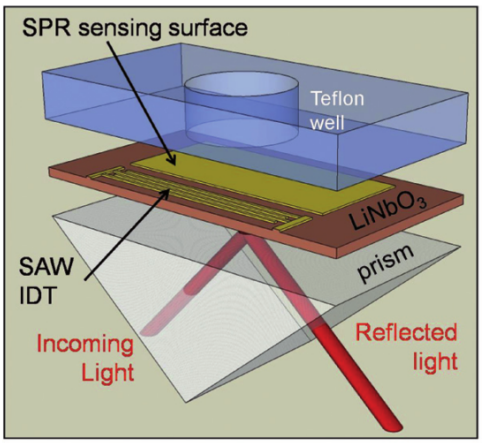

Figure 2.14: Schematic diagram of the integrated device made by Renaudin et al. showing the SPR sensing surface and SAW IDT electrodes on a common $LiNbO_3$ piezoelectric substrate. Also shown are the SPR excitation and reflected light paths that are coupled to the sensing surface via the prism, as well as the microfluidic well atop the SPR sensing surface [6].

They postulated that any temperature increase in the fluid at the metal surface due to a SAW pulse would dissipate after a certain relaxation time. This statement was justified by assuming that the majority of the fluid outside the SAW fluid heat range acted as a heat sink. They studied the heating effect in water by activating SAW at increasing RF power levels for 5 *sec* after each relaxation time (that was determined by measuring the time taken for the SPR signal to return to a stable plateau). They showed that the relaxation times ranged from 300 *sec* to 30 *sec*, with a linear dependence on power level (Figure 2.15).

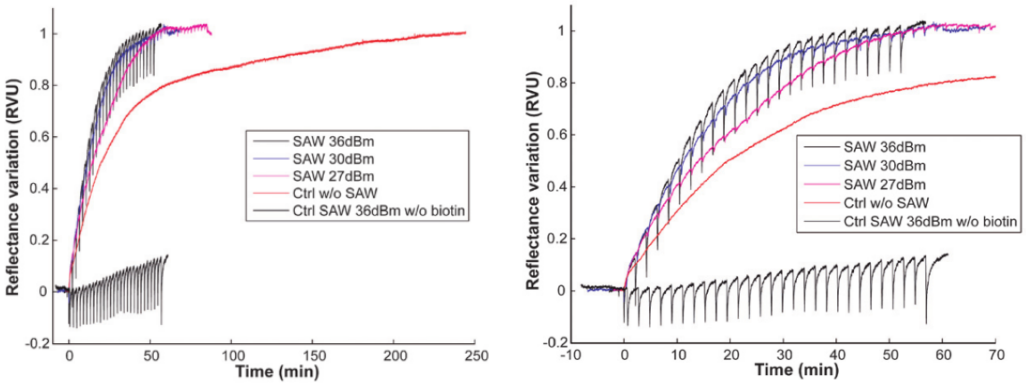

Figure 2.16: Graphs showing SPR reflectance variations at a fixed angle of interrogation as a function of time, for a biotin-avidin assay in PBS (avidin is introduced at $time = 0$). A negative control without the application of SAW in the avidin-biotin assay is shown (Ctrl w/o SAW). A negative control where unbiotinylated BSA was adsorbed onto the surface followed by injection of avidin under 36 dBm SAW is also shown (Ctrl SAW 36 dBm w/o biotin). LEFT: full time scale; RIGHT: Zoomed view [6].

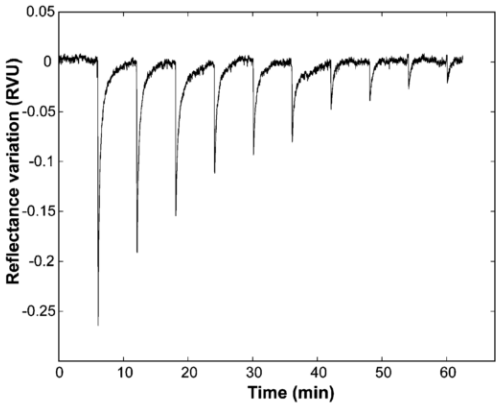

Figure 2.15: Plot of SPR reflectance variation over time at a fixed interrogation angle, showing the effect on the SPR response of heat injection into the fluid (water) caused by single SAW pulses of various power levels. For each power level (37 dBm to 28 dBm, in increments of 1 dBm), the SAW were excited for 5 s then turned off to allow the system to return to a stable plateau before the next SAW pulse. Results are given in reflectance variation units (RVU), where 1 RVU equals 100% reflectance change [6].

They functionalized the SPR surface with biotin and placed a solution of 1 $\mu g/mL$ avidin in PBS in the fluidic well (200 μL). Then, they alternately activated the SAW-induced mixing for 5 sec (0 sec after avidin introduction) and then turned it off for 120 sec, for about one hour in total. This experiment was made at different powers (27 dBm, 30 dBm and 36 dBm) resulting in accelerated kinetics (results are shown in Figure 2.16).

However, the study of Renaudin et al. did not fully address some important aspects related to chip operation and data interpretation. First of all, they did not use a microfluidic device but made all the measurements in droplet without the possibility of continuous flow operation. Moreover, they did not monitor full reflectance spectra that typically characterize SPR in Kretschmann configuration. RVU measurements are not exactly meaningful in this case because not only the minimum value of the reflectance shifts to higher wavelengths or angles of inci-

dence (depending on the type of modulation used) but also the spectrum changes its shape in a non-trivial way excluding the possibility of characterizing the chip properly and extrapolating quantitative data for biosensing applications. Another critical point of this work is the total lack of quantification of the SAW-induced streaming and heating in the fluidic well which led to conjectures to justify their methods and results. Despite this, not even feedback controls were used to decouple the different effects that could have influenced the system. They neither show the dynamics of mixing in the well nor quantify the heating, neglecting that different SAW powers, and consequently SAW amplitudes, induce different velocity fields and temperatures in the fluid. Temperature is a crucial factor in biological binding events and it must be known before saying anything about the system to be studied. By alternatively activating SAW pulses the biological system was subjected to heating pulses that could have irreversibly damaged or modified the biological system.

By the way, Reanudin et al. results are really promising but it is important to study in details all the SAW-induced effects in order to optimize the biosensor and to understand the involved physics. For this reason, this work formed the inspiration for this master thesis work.

Part II

Experimental Results

Chip Development and Setup Optimization 3

3.1 Nanostructure Fabrication Techniques

3.1.1 Lithographic Principles

Resist

Most processing steps in micro- and nano-fabrication use a temporary thin layer of a material known as *resist* (due to its ability to withstand certain acids as well as plasma-based etching process, which will be discussed later). They are usually a mixture of a polymer[1] and other molecules specially formulated for a given lithography technology. Resist deposition onto a clean substrate usually occurs via *spin-coating*. After the application of a small amount of resist on the center of the sample, it is then spun at high speed in order to evenly spread the resist by centrifugal force. After this first step the sample is *soft baked* in order to evaporate residual solvent (this procedure is shown in Figure 3.1).

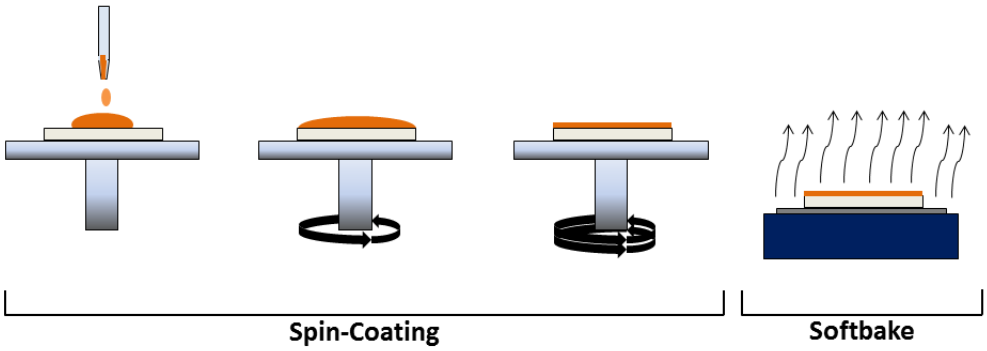

Figure 3.1: Diagram of spin coating of a resist onto a substrate and further soft baking.

Resists are generally classed as *positive* or *negative*. A *positive resist* is one whose solubility in the developer (an appropriate chemical solvent) increases when it is exposed to the lithographic source while the solubility of a *negative resist* decreases (Figure 3.2).

[1] A polymer is a large molecule, or macromolecule, composed of many repeated subunits

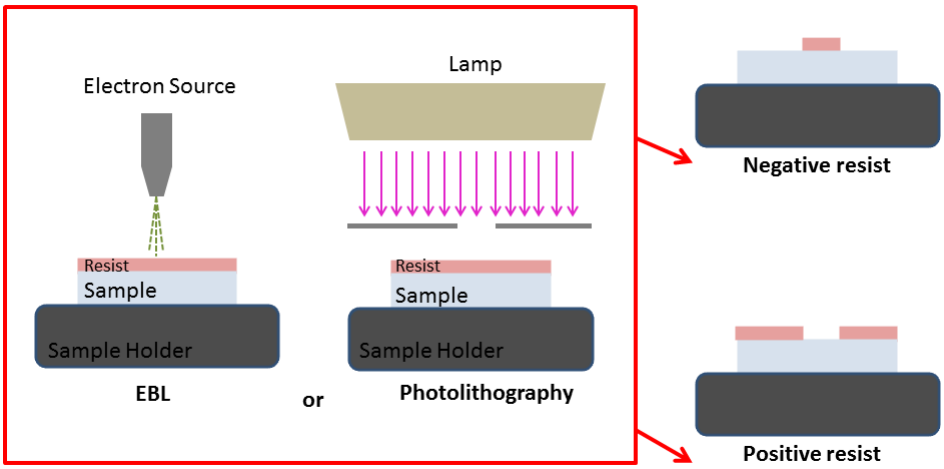

Figure 3.2: In the red box on the left, pictorial representation of electron beam lithography and photolitography. On the right, the sample after the development in the case of a positive (upper) and a negative (lower) resist on the same sample.

The most popular method for pattering a layer of resist (used in this case as an *etch mask*) employs UV light with a wavelength less than 500 nm and it is known as *photolitography*. This allows the patterning of features down to the order of 0.5 μm. In addition, a method for achieving features below 0.1μm employs low to moderate energy electrons tightly focused in a charged beam, in a technique known as *electron beam lithography*.

The final step, after lithography, is *resist development* where the exposed (or unexposed) resist is removed by a wet solvent. The solvents used are typically weak basic solutions and vary from resist to resist. Developing is done by submerging the resist-coated substrate in the developer, sometimes diluted with water to slow the dissolution rate, and once developing is complete the substrate is rinsed with water to remove all traces of the developing solution. After blow-drying the substrate with high pressure dry nitrogen the process is complete.

Photolithography

Photolitography relies on the use of a photosensitive organic film of resist, known as *photoresist*. After spin-coating and softbaking, the coated substrate is then selectively exposed, typically by passing UV light through a *photomask*. A photomask consists of a glass plate coated with an opaque surface, which can be etched with highly detailed patterns. The most common type of photomasks are quartz glass plates with an opaque chrome layer. The photomask is aligned on the substrate by using a mask aligner, using the substrate boundaries for the first lithographic step, or registry marks from previous lithographic layers for further layers. Mask aligners based on contact lithography (where the photomask and the substrate are placed in direct physical contact, so that a 1:1 copy of the photomask pattern is transferred to the photoresist) are the most common. Contact aligners typically use mercury lamps as the UV source, using either 465 nm or 365 nm emission wavelengths. The exposure dose D (expressed in J/m^2) depends on the type of the resist to be used and on the thickness of its layer.

For the experimental setup used for this thesis work, feature sizes are limited to resolution of order $1-2\ \mu m$ and above, although with some care features as small as $0.5\ \mu m$ can be achieved over small areas.

Electron Beam Lithography (EBL)

EBL provides linewidths significantly less than $1\ \mu m$ down to the nm scale. Systems range from converted scanning-electron microscopes for direct writing under the control of a computer to full lithographic systems with automatic pattern alignment and stitching capability to write over large areas. The basic principles are very similar to those of photolithography; the electron beam replaces the UV illumination as the exposure source, and different types of resists are used to those used for optical processes, but otherwise the concepts remain the same.
The beam of electrons can be created using a number of different sources ranging from cold Schottky emitters for field-emission systems to tungsten (W) or lanthanum hexaboride (LaB_6) for thermionic emitters. Once the electrons are extracted from the source they are accelerated by electrostatic fields to energies, E, ranging from a few keV up to $100-200\ keV$ and a system of magnetic lenses and beam stop apertures is used to focus and narrow the beam. Magnetic scan coils are used to direct the beam to different points on the sample. A probe used to measure electron current in the beam, I, may also be included as well as a beam blanker to switch the beam on and off rapidly.
The sample resides in a chamber at the base of the column on a stage allowing translation and rotation. The electron beam hits the sample with the electrons passing through the top surface and then scattering within the volume of the sample. The pattern is exposed in several steps using stitched subfields (the so-called *write fields*, WF). The exposure time t_{exp} must follow the relationship $D \cdot A = t_{exp} \cdot I$, where A is the area exposed. Radiation in the form of X-rays and secondary electrons are emitted from the sample, the latter forming the primary imaging mechanism for viewing.

3.1.2 Thermal Evaporation of Metallic Thin Films

Thermal evaporation is performed in a vacuum system with a base pressure of 10^{-6} *Torr* or lower in which the substrate and the material to deposit (the source) are placed. The source material is heated to the point where its vapour pressure becomes sufficiently high to generate a substantial flow of material from the source and the atoms flow ballistically without colliding with residual gas atoms to the substrate surface where typically a high percentage ($\sim 30\%$) of the atoms adhere and form a film. Metals typically must be heated to temperatures of at least $400-500^{\circ}C$, higher for *refractory metals* such as Ti or Ni. This can be done by *Joule heating* where the source is placed in a boat or on a wire filament made of a high temperature resistant material (typically W or Mo) through which a DC current of order $100\ A$ is run.
The ballistic transport from the evaporation source to the substrate means that material will only be deposited at points on the substrate that are on a line of sight to the evaporation source; points blocked by intervening material such as a mechanical mask patterned on the substrate will not receive any material.

3.1.3 Etching Techniques: Dry and Wet

Etching is the process by which material is removed from a surface. Among all dry etching techniques reactive ion etching (RIE) is the most common form for plasma etching. A mixture of gases (dependent on the material to be etched) are introduced in a high-vacuum chamber where they are ionized by an RF voltage source applied between a pair of parallel plate electrodes. Because of the large voltage difference, the positive ions tend to drift toward the low voltage electrode at the base, where they collide with the samples to be etched reacting with it. The reaction products must be volatile and are carried away in the gas stream.

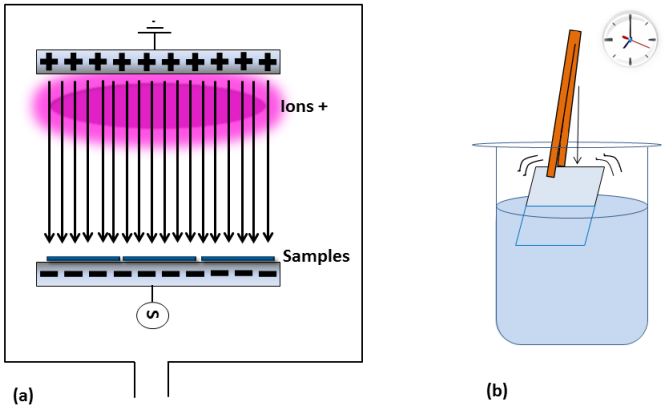

Figure 3.3: Diagram of RIE (a) and typical wet etching procedure (b) are shown in the figure.

The dry etching techniques tend to have higher lateral resolution and in some cases better depth control than the wet etching techniques. Wet etching is suitable for structures with lateral dimensions above 1 μm or so, although with care structures can be patterned with lateral dimensions down to 0.1 μm. On the other hand, wet etching has two advantages: very high chemical selectivity (with certain combinations of masks and substrates) and very low crystalline and electronic damage induced by the relatively gentle chemical process. Some chemical etches also etch preferentially along certain crystal directions or etch certain crystal planes very slowly. However, vertical control is typically much more difficult to achieve with wet etching than with dry etching.

3.2 Chip Development

Three different chips were used during the various experiments performed during this master thesis work.

3.2.1 *Droplet-Based SPR sensor*

In order to characterize the SPR sensing system itself, measurements were taken with a so-called *droplet-based SPR sensor* (a 3D model of the chip is shown in Figure 3.4a). It consists of a 1 $inch \times 1$ $inch$ 128° Y-cut LN substrate (0.5 mm thick) with

two metallic layers on top: an adhesion layer of titanium (10 nm thick) and a layer of gold (55 nm thick).
The fabrication procedure for each chip was made in an ISO 6 cleanroom. The chip substrate was cut from a 128° Y-cut lithium niobate (LN) wafer with a diamond scriber, followed by a wash in Acetone (ACE), (semiconductor grade, `Sigma-Aldrich`, then in 2-Propanol (IPA), ($\geq$ 99.5 %, `Sigma-Aldrich`), and finally blow-dried with nitrogen. The metallic layers were deposited by a thermal evaporator (`Kurt J. Lesker` Nano 38, KJL) at high-vacuum base pressure ($\sim 10^{-5}$ $mbar$).

Lift-off and KJL Calibration
The evaporator was calibrated before starting the fabrication processes. Samples of 1 $cm \times 1$ cm of 128° Y-cut LN were cut, spin-coated for 1 min at 6000 rpm with the positive resist S1818 and softbaked at 90°C for 1 min. Photolithography with an exposure dose of 65 mJ/cm^2 was made with a manual MBJ4 mask aligner (`SUSS MicroTec`). The resist was successively developed in MF319 for one minute, washed in a 250 mL-beaker filled with water and then blow-dried with dry nitrogen. After this procedure the resist covered only half of the sample. The samples were treated with oxygen plasma to promote the adhesion of the metals onto the substrate. Each sample was then evaporated at different nominal thicknesses. After the evaporation, the samples were placed in beakers with ACE. ACE dissolved the resist which was exposed to the UV-light and only half of the LN substrate was covered by the metals. This procedure (where the part of the sample covered with resist will be metal-free after its dissolution in a proper solvent) is known as *lift-off* and it is a method of patterning a material (in this specific case the metallic layers) on the surface of a substrate (LN, in this specific case) using a photoresist (S1818).
All the surface profiles of the samples were measured with a 3D Stylus Profilometer DEKTAK XT (`Bruker`). The difference between the thickness of the nominal Ti and the thickness of the measured Titanium (Ti) layer was found to be negligible (of the order of 10^{-1} nm) whereas the measured thickness of the gold (Au) layer was about 0.87 times the nominal thickness layer. Therefore, by following these results, it was possible to set the real gold thickness by dividing the nominal value by a factor 0.87.

The best thicknesses for SPR excitation of the Ti and Au layers were found with matlab simulations in a previous work [34]. They were chosen in order to maximize SPR detection parameters (as discussed in the following sections). Gold (instead of other metals) was chosen because of its high chemical inertness and ease of chemical functionalization.

3.2.2 *μchannel SPR sensor*

After the characterization of the SPR sensing system with droplets, the following step was the characterization of the SPR sensing system coupled to PDMS microchannels (the motivations for the design will be discussed in the next section). Four gold square SPR sensing areas of 4 mm^2 were patterned on a 1 $inch \times 1$ $inch$ 128° Y-cut LN according to the following

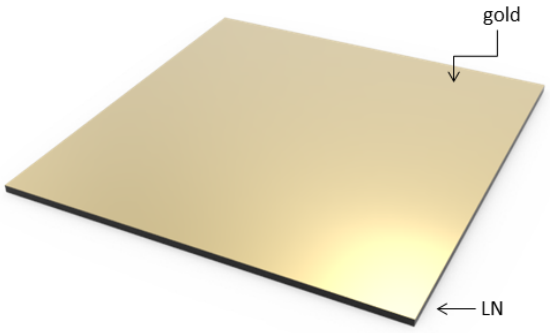

(a) Droplet-Based SPR sensor

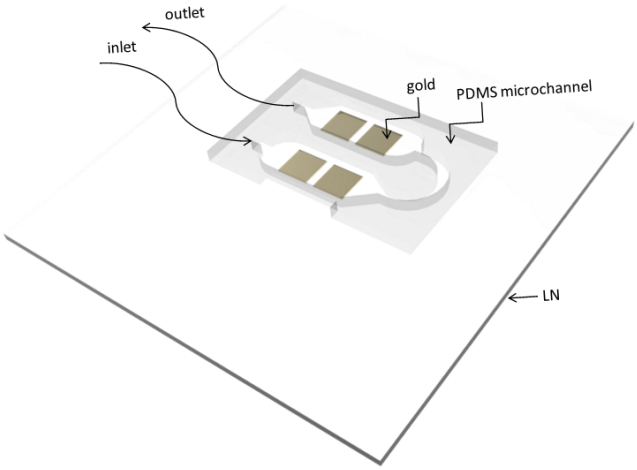

(b) μchannel SPR sensor

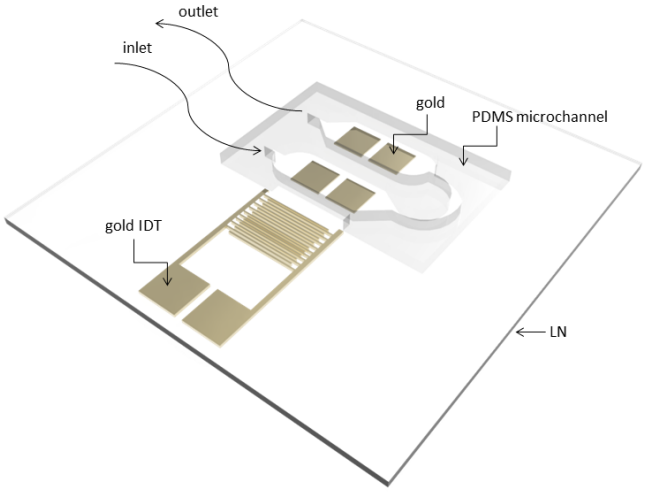

(c) SAW-Based SPR sensor

Figure 3.4: 3D models (not to scale) of the sensing chips.

MICROFABRICATION PROCEDURE:

1. cutting and cleaning (ACE-IPA-dry nitrogen) of the LN chip substrate from the 0.5 mm-thick wafer;
2. spin-coating of S1818 for 1 min at 6000 rpm and softbaking at 90°C for 1 min;
3. UV-lithography (exposure energy of 65 mJ/cm^2);
4. resist development in MF319 for 1 min (stop in water) and blow-drying with dry nitrogen;
5. oxygen (10 %) plasma treatment, 100 W, $p \sim 2$ $mbar$, $V_{bias} = 300$ V;
6. evaporation of Ti:Au (10 nm : 100 nm-thick);
7. lift-off (1 $hour$ in ACE);
8. cleaning (IPA-dry nitrogen)

A schematic of the photomask used for the UV-lithography step is shown in Figure 3.5a whereas a schematic of the chip after the process is shown in Figure 3.5b. The photomask consisted of a black-printed slide attached onto a (10.12×10.12) cm^2 quartz (2.3 mm-thick) substrate.

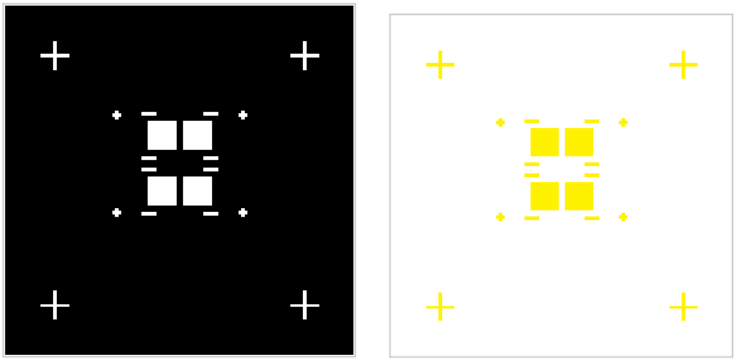

(a) Schematic of the photomask used for the UV-lithography of the SPR gold square surfaces.

(b) Schematic of the chip after the microfabrication procedure used to make the SPR gold square surfaces.

Figure 3.5: Pictorial representation of (a) the photomask used for the UV-lithography of the SPR gold square surfaces and of the (b) chip after the microfabrication procedure described above.

The distances between the SPR gold square surfaces are 500 μm along the y direction and 2 mm along the x direction (see Figure 3.6). In both directions the distances between SPR squares are much more than the typical propagation length (see §1.1.3) of SPs excited at a gold-water interface by visible light (which is 40 μm at its maximum value). In this configuration, SPR surfaces can be considered decoupled. Two SPR gold square surfaces are present in each chamber in order to have the possibility of functionalizing only one of the two and have a feedback controls on the functionalization. The small four crosses around the SPR gold square

surfaces (see Figure 3.5b) are markers necessary for the microchannel alignment during the bonding procedure. The choice of microchannels made of PDMS is due to the advantages associated to this material In fact, unlike traditional microfabrication materials, such as silicon and glass, PDMS is a low-cost material and the micro-molding processes are simple and rapid when compared to traditional etching and bonding approaches. The primary advantages of PDMS material for microfluidics applications include ease of bonding and optical properties (transparent in the UV and visible light ranges) [35].

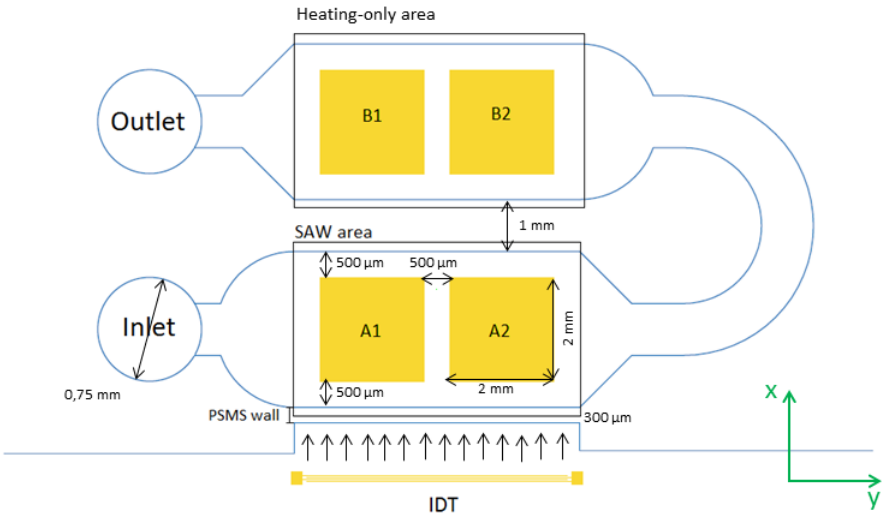

Figure 3.6: Schematic of the SAW-based SPR sensor in the microchannel area (top view). Except for the IDT (of which only the end of the busbars and the first two pairs of fingers are shown), it is exactly the scheme of the microchannel area of the μchannel SPR sensor. The main dimensions are specified by the black double-arrows.

MICROCHANNEL FABRICATION

The first step of microchannel fabrication is the preparation of PDMS. In its raw form PDMS is a highly viscous flowing liquid – though still optically transparent. A curing agent can be added to this PDMS to accord its structural rigidity. They act as branching points, helping form internal cross links that turn the PDMS into an elastomer.

A solution of 20 g of PDMS and curing agent in a ratio of 10 : 1 was made first. The mixture was vigorously whisked in a plastic cup with a spatula. About 2 minutes of whisking was needed to uniformly distribute the curing agent, ensuring that the final PDMS mold was uniformly cross linked. The mixture was poured into the microchannel mold (that consisted of a silicon substrate -placed in a plastic petri dish- where the microchannel was patterned by the resist SU-8-2100). The final mixture was filled with air bubbles from the whisking process. For this reason, the mold with the mixture was kept for about 1 *hour* in a bell-jar dessicator connected to a vacuum pump to release the trapped air bubbles. Once a clear, bubble free PDMS mixture was obtained the mold was placed in an oven at 80°C for at least 1 *hour*. Once the PDMS was consolidated, microchannels were

cut with a scalpel and inlet and outlet holes were made with 0.75 *mm*-diameter biopsy puncher.
A schematic of the section of the base of the microchannel is shown in Figure 3.6. The microchannel consisted of two chambers of a height of 360 μm and a width of 3 *mm* (0.5 *mm* larger, on each side, than the width of the SPR surfaces) that covered the four gold SPR surfaces (two squares in each chamber). The 45°-shape inlet aperture and curved outlet were made in order to minimize the creation of air bubbles in the fluid during the injection.
A *plasma activated bonding* process was used to irreversely bond the microchannel to the LN substrate.

LN-PDMS PLASMA-ACTIVATED BONDING PROCEDURE:

1. oxygen (10%) plasma treatment to the LN substrate, 120 *sec*, 100 *W*, $p \sim 2 \cdot 10^{-1}$ *mbar*, $V_{bias} \sim 340$ *V*;
2. oxygen (10%) plasma treatment to the LN substrate and the PDMS microchannel, 45 *sec*, 10 *W*, $p = 2 \cdot 10^{-1}$ *mb*, $V_{bias} \sim 100$ *V*;
3. alignment of the microchannel onto the LN substrate (without any contact) and contact (this step was made using a microscope and the alignment marks on the substrate and the microchannel);
4. baking at 80°*C* in an oven;

Different procedures (with different plasma times and baking times) were used to find the procedure that optimized the LN-PDMS bonding. The procedure described above was the procedure after which all the PDMS area placed in contact with the LN substrate was bonded with it. In this case the bond was so strong that the microchannel broke if one tried to separate it from the LN substrate. Therefore, this system was really stable under fluid injection and continuous flow operation.
A syringe was connected by a `Tygon` tube to the inlet hole in order to fill the microchannel. The outlet hole was connected to a beaker (waste) in order to gather the fluids used during the experiments.

3.2.3 *SAW-Based SPR sensor*

The chip used in the final part of this master thesis work, after the SPR characterization in droplets and microchannels, is identical to the μchannel SPR sensor but with an IDT (needed to excite the SAW) patterned on the chip (see Figure 3.4c). The single-electrode IDT (with an aperture of 5 *mm*: the length of each microchannel chamber) was fabricated in front of the the four SPR square gold surfaces (Figure 3.6) and was composed of 19 pairs of fingers, two busbars and two pads (see Figure 3.7).

The nominal width of each finger was 20 μm with a periodicity of 80 μm that matched the λ_{SAW} (in order to work in the most efficient configuration, as explained in §2.2.2). As the speed of sound along the LN substrate is 3980 m/s, the resonant frequency, $f_0 = f_{SAW} = \frac{v_{sound}}{\lambda_{SAW}}$, was about 50 MHz. The number of finger pairs was chosen in order to make the conductance of the IDT match the conductance of the electrical circuit of the PCB, G, (equal to 0.02 $S = 1/r$ where $r = 50\ \Omega$). $G = 8K^2C_0f_0WN_p{}^2$ where W is the IDT aperture (see Figure 3.7) and

C_0 is the capacitance per finger pairs. The choice of the 128° Y-cut LN substrate was due to its good electromechanical coupling coefficient (see Table 2.2) Figure 3.7 shows a schematic of a single-electrode IDT and a detail of a portion of the fingers and a busbar made with the IDT fabrication procedure.

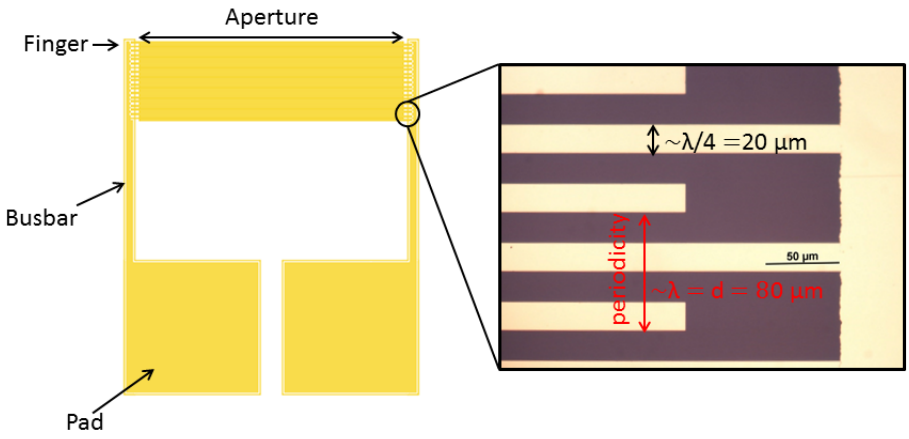

Figure 3.7: Schematic of a single-electrode IDT composed by two busbars, two pads and finger pairs. On the right a picture made with a Nomarski optical microscope (50X) shows a portion of fingers connected to a busbar.

The microchannel had two chambers (one in front of the others) covering the SPR areas to provide feedback controls on the measurements. In fact, the microchannel was designed and fabricated so that the SAW was completely damped after the first chamber. SAW modulation starts at the first PDMS wall of 360 μm and continues along it and along the 500 μm of water before the A1 and A2 SPR surfaces (see Figure 3.6). As a consequence no acoustic modulation but only acoustic streaming occurred on the SPR squares of the first chamber that the SAW runs into. A 1 mm PDMS wall was present between the first and second chamber to separate them. It follows that SAW-induced streaming was only possible in the first chamber (in the *SAW area*, see Figure 3.6) whereas in the second chamber (in the *heating-only area*, see Figure 3.6) only the possible heating effect of SAW on the substrate was present. By using this microchannel design, it was possible to make measurements of the sample by decoupling the heating and streaming effects of the SAWs.

The MICROFABRICATION PROCEDURE for this chip was the following:

1. substrate preparation;
2. IDT fabrication;
3. SPR gold square surfaces fabrication

where SUBSTRATE PREPARATION consisted of:

1. cutting and cleaning (ACE-IPA-dry nitrogen) of the LN chip substrate from the 0.5 mm-thick wafer;

2. plasma oxygen treatment, 100 W, 1 min, $p \sim 2 \cdot 10^{-1}$ $mbar$, $V_{bias} \sim 300$ V;
3. evaporation of Ti:Au:Ti layers (10 nm : 55 nm : 30 nm-thick);

IDT FABRICATION PROCEDURE:

1. spin-coating of AR-300-80 (negative resist used as adhesion promoter) for 1 min at 4000 rpm and softbaking at 90°C for 5 min;
2. spin-coating of MA-N-2403 (negative resist) for 1 min at 6000 rpm and softbaking at 90°C for 1 min;
3. EBL, 10 keV, beam aperture of 20 μm, $D = 10 \mu C/cm^2$, $WF = (200\ \mu m)^2 \Rightarrow$ fingers of the IDT (19 pairs with a width of 20 μm);
4. resist development in MA-D-525 for 1 min (stop in water) and blow-drying with dry nitrogen;
5. wet etching of 30 nm-thick Ti layer 30 sec in a solution of hydrofluoric acid (HF) and water (1 : 30)
6. spin-coating for 1 min of S1818 at 6000 rpm and softbaking at 90°C for 1 min;
7. UV-lithography (exposure energy of 65 mJ/cm^2) $\Rightarrow$ busbars and pads of the IDT;
8. resist development for 1 min in MF319 (stop in water) and blow-drying with dry nitrogen;
9. evaporation of a 30 nm-thick layer of Ti;
10. lift-off (1 $hour$ in ACE);
11. RIE, 69 W, $V_{bias} = 378$ V, process time of 10 min, 43 $sccm$ of Ar ($p_{process} = 9.04\ 10^{-2}$ $mbar$);
12. wet etching of 10 nm-thick Ti layer 10 sec in a solution of hydrofluoric acid (HF) and water (1 : 30)

whereas the SPR gold square surfaces fabrication was the same used for the μchannel SPR sensor and described in the previous section.

Figure 3.8 shows a schematic of all the IDT fabrication procedure steps.

3.3 Gold Surface Functionalization

Making SPR measurements of biological binding events requires the functionalization of the SPR surfaces with a proper biorecognition element. Functionalization is the procedure used to immobilize these targeting ligands onto the sensing surface and it depends on the surface to be functionalized and on the analyte to be studied. In this master thesis work a biotin-streptavidin system was studied (motivations are explaned in §4). Biotin was used as biorecognition element. Thiol-modified biotin was synthesized by a chemist of the laboratory. The chemical modification

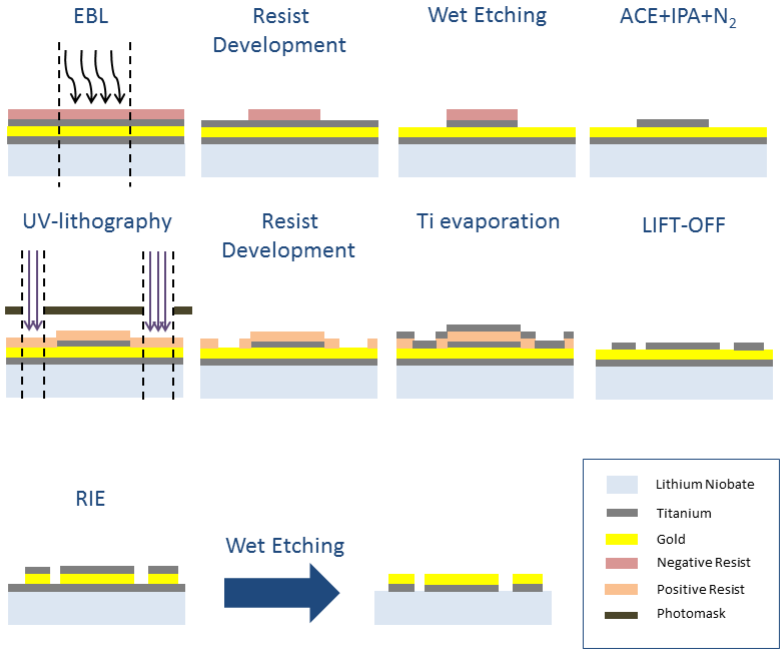

Figure 3.8: Schematic of the steps of the IDT fabrication procedure described above.

of biotin with a thiol functional group was necessary to make the biotin interact with the gold surface. Thiol-gold semicovalent interaction strength (owing to the the strong affinity of sulfur for metals) provides the basis to fabricate robust self-assembled monolayers (SAMs). SAMs of thiolates form within a few minutes [36].

Biotin-thiol was in a freeze-dried form stored at $-20°C$. For a typical experiment, the modified biotin was dissolved into a water-ethanol (10:1) solution at a concentration of 1 mg/mL. The biotin-thiol weight (8 mg, typically) was measured with a microbalance whereas the water-ethanol solution was made with Gilson pipettes. Ethanol was placed first in a 15 mL Falcon conical centrifuge tube. Freeze-dried biotin-thiol was added into the Falcon to start its dissolution. Water was added at the end and the solution was mixed overnight with a vortex mixer at $4°C$. The gold functionalization occurs almost immediate after placing the biotin-thiol-water-ethanol solution on top of the surface making it possible to have short experiment times. Droplet-based SPR sensors (1 $inch \times 1$ $inch$-SPR gold squares) were functionalized with 300 μL of the main solution whereas the four 4 mm-SPR squares of the other two chips were functionalized with 1.44 μL each. In all of these cases the biotin concentration in water-ethanol was enough to saturate the SPR gold squares and guarantee the maximum functionalization by particle diffusion.

3.4 Experimental Setup

3.4.1 Optical Setup Optimization

The optical setup used to make SPR measurements was in the Kretschmann configuration with wavelength modulation (as described in §1.3). Therefore, a high-refractive-index prism and a polychromatic light source were needed. A light source `Leica` CLS 150 XE (halogen lamp) was used at its maximum power (150 W) to excite the SPs and an uncoated SF11 10 mm- micro right angle prism ($n_d = 1.7847$) purchased from `Edmund Optics` was used to make the SPR possible by the evanescent field excitation at a fixed angle. The SPR was detected by acquiring reflectance spectra of p-polarized (which can excite SPs) and s-polarized (which can not excite SPs) light with a TRISTAN light desktop spectrometer (`MUT`) working in the range of $400 - 800$ nm.
An optical setup mounted in the laboratory was used and optimized (Figure 3.9).

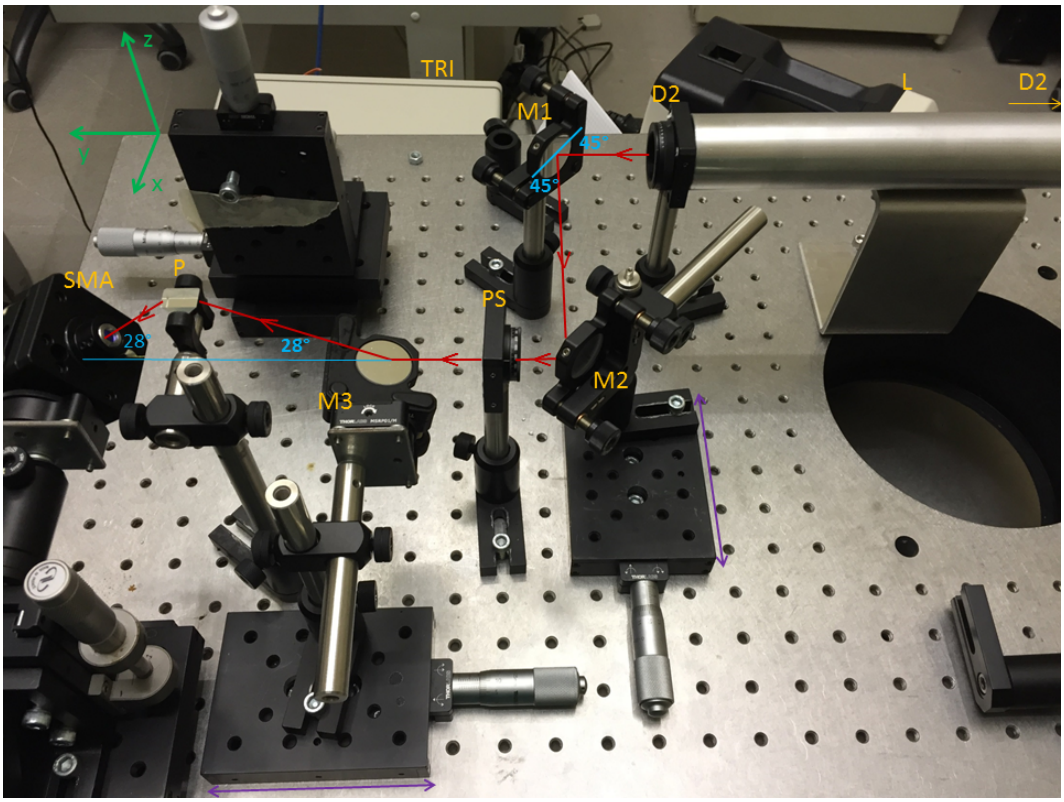

Figure 3.9: Photo of the optical setup used for SPR excitation. The optical path of the light beam is shown with a red arrow. The characteristic angle of the planes of the components with respect to the light beam is shown in blue. Labels of the name of the main components of the setup are shown in yellow. The green arrows on top of the left side of the picture represent the lab coordinate system.

To limit the divergence of the light beam, two diaphragms (D1 and D2 in Figure 3.9) of variable diameter ($1 - 12$ mm) were placed at a distance of 30 cm from each other. Their diameters were both set to be 1 mm in order to collimate the light beam as much as possible directly after the light source. In this configuration the approximation of plane waves hold. The two diaphragms were connected by

a metallic tube in order to minimize the light noise from the laboratory. For a similar reason, the direction along which the SPR measurements had to be taken was chosen to be different from the optical path of the light source. In this case noise would have been caused by the light source. To avoid this, two silver mirrors (M1 and M2 in Figure 3.9) were placed at 45° with respect to the direction of the light beam. The first mirror was placed in a fixed position in front of the second diaphragm whereas the second mirror could be moved with a single-axis translation stage with standard micrometer (with a resolution of 500 μm and a travelling distance of 25 mm). In this way it was possible to move the light beam along the x-direction of the sample (laboratory coordinate system axes are shown in green on top of the left side of Figure 3.9). A linear polarizer (PS in in Figure 3.9) in a rotation mount was placed between the second mirror and a third mirror. The third mirror (M3 in in Figure 3.9) was mounted on a manual rotation stage (with a sensitivity of 0.5°) onto a linear translation stage (with its translation direction perpendicular to the translation direction of the previous stage). By changing the tilt angle of its plane it was possible to change the incidence angle of light on the oblique face of the prism and consequently with respect to the sample. At the beginning a scan in angle was necessary to find the best configuration for SPR excitation. By moving the mirror with the stage it was possible to move the light beam along the y-direction of the sample. The optical path was minimized by design in order to minimize the cross-section of the light beam along the prism. The light beam alignment was checked at each optical component. Each component was placed so that the beam was centred (their best working area). After having found the SPR excitation angle, the rotation platform of the mirror was blocked and the translator was used to move the beam spot along the chip substrate. Total internal reflection occurs at the plane of the prism parallel to the plane of the lab. For this reason the reflected light can be detected at an angle equal to the incidence angle. An SMA optical fiber connector (SMA in Figure 3.9) was used to detect the reflectance spectra with the spectrometer. The optical fiber connector consisted of a lens with a central focal length of 18.24 mm, an alignment wavelength of 633 nm and a numerical aperture (NA) of 0.15. The SMA was mounted on a rotation stage mounted onto an assembled XYZ translation stage. This allowed the maximization of the signal in a simple and fast way because if the position of the light beam underneath the sample (x, y and angle) changed, the SMA position had to change symmetrically on the other side. Before each measurement the detection of the signal was optimized by translating the SMA in the three directions and tilting its plane so that it was perpendicular to the light beam. The signal was considered optimized when by small changes of the position of the SMA and the angle of its plane the reflectance spectra (watched in real time on the screen of the laptop connected to the spectrometer with a TriWin software) decreased in amplitude. A typical reflectance spetra of s-polarized and p-polarized light for water in SPR condition is shown in Figure 3.10.

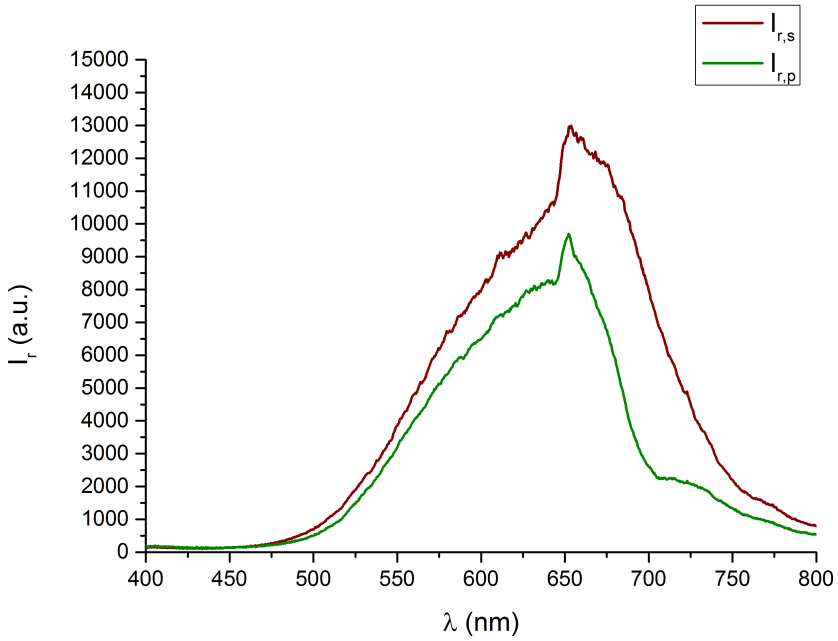

Figure 3.10: Reflectance spectra of s- and p-polarized light incident on a droplet-based SPR sensor with 300 μL-droplet of water on top (resonant condition).

The integration time was set to 500 *ms*. In this situation the signal intensity measured as RAW data (expressed in arbitrary units) was about 13000 for incident s-polarized light. The integration time was chosen to be as high as possible in order to reduce noise (after checking that the signal was always constant over this time) but not close to the saturation (15000 *a.u.*).
The polarizer was calibrated with another polarizer with known direction of polarization. P-polarization of light coincided with the direction indicated by the 194°-direction whereas s-polarization was along the 284°-direction. Due to the fact that only p-polarized light can excite SPs and that the polychromatic light used was not polarized instead of the reflectance of p-polarized light, the SPR can be detected as a dip in the normalized reflectivity:

$$R = \frac{R_p}{R_s} = \frac{I_{r,p}}{I_{r,s}} \tag{3.1}$$

where R_p is the reflectivity of p-polarized light, R_s is the reflectivity of p-polarized light, $I_{r,p}$ is the intensity of the p-polarized light reflected by the prism and $I_{r,p}$ is the intensity of the p-polarized light reflected by the prism. This normalized reflectivity could be used to detect SPR instead of reflectivity because the polychromatic light source used for the experiment was not polarized (see §4 for more details). As shown from simulations (an example in Figure 3.11), in the Kretschmann configuration with wavelength modulation (in the range of wavelengths detected by the spectrometer used for these experiments) SPs can be excited at different light incident angles but only one maximizes SPR detection.

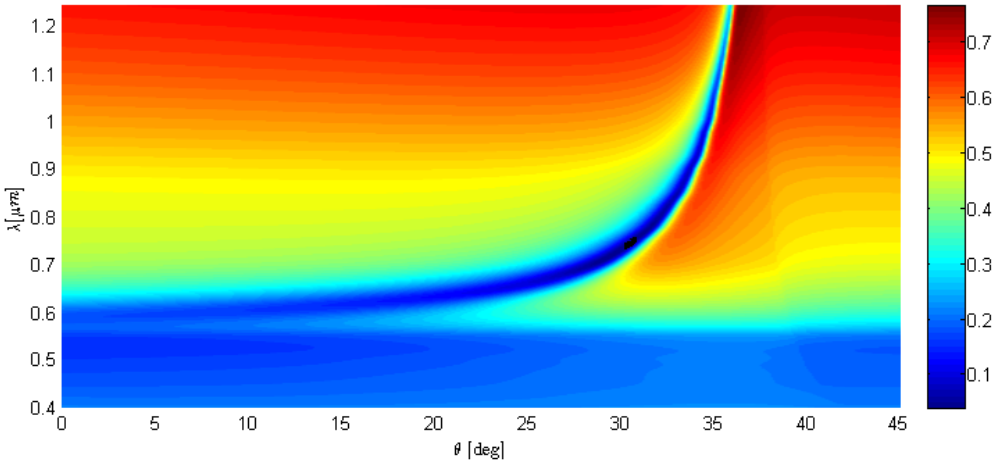

Figure 3.11: 3D colormap made with Matlab simulations. The plot shows the reflectance of p-polarized light at different angles of incidence of light (with respect to the laboratory plane) at different wavelengths.

The fixed angle at which all measurements were taken was the angle at which the amplitude of the dip was at its maximum and its full width at half maximum (FWHM) was minimum. Moreover, the angle chosen had to ensure a good range of detection. The angle at which the best signal for water droplets (water is the typical dielectric used to test SPR sensor characteristics) was found was 28° with respect to the lab coordinate system plane ($\alpha = 62°$). Figure 3.12 shows the normalized reflectivity for a 300 μL water droplet at different angles. The shape of the dip justifies the choice of 28°.

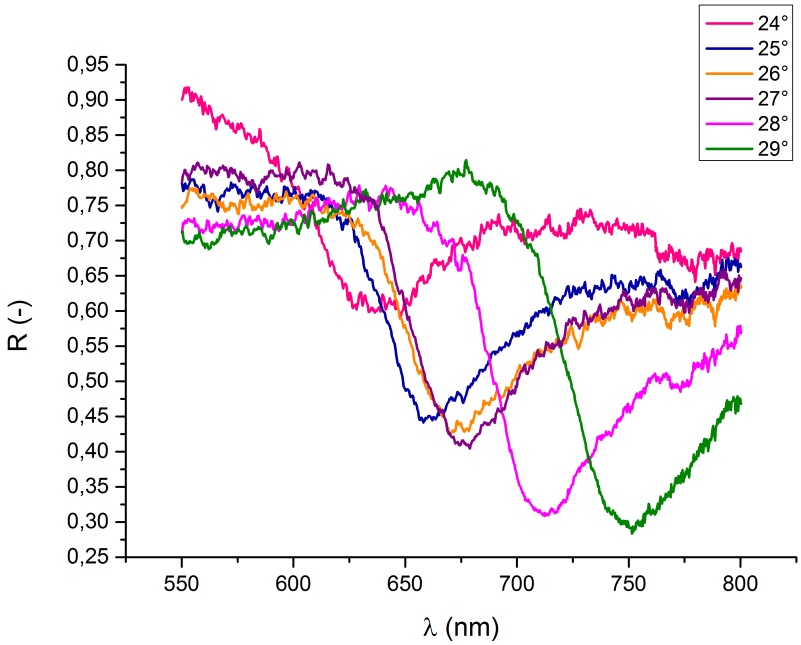

Figure 3.12: R vs λ at different angles of incidence of light (with respect to the lab plane).

μchannel and SAW-based SPR sensors

Measurements in droplets were made by placing a droplet of glycerol (matching layer, $n_d = 1.4716\ RIU$) onto the prism and by placing the chip onto it. The chip was placed such that the direction of SAW propagation was perpendicular to the light beam direction in order to avoid oscillations in the measurements due to the birefringence of the LN substrate. When the chip was placed onto the prism, the glycerol droplet spread over the face of the prism parallel to the lab coordinate system plane. Glycerol spread because of the weight of the chip, covering the whole detection area. The chip surface was all covered by gold (see description in §3.2.1) allowing the detection of SPR in any point of the surface.
In the experiments made with the μchannel and SAW-based SPR sensors the microchannels (connected to the syringe from the inlet and to the waste from the outlet, see Figure 3.13c) needed to be fixed onto the prism and, in the second case, the IDT onto chip had to be connected to an RF signal generator. For this reason in these experiments the chips were not simply placed on top of the prism but were mounted on a printed circuit board (PCB), mounted on an XYZ translator stage (Figure 3.13a). The chip was fixed to the PCB as shown in Figure 3.13b.

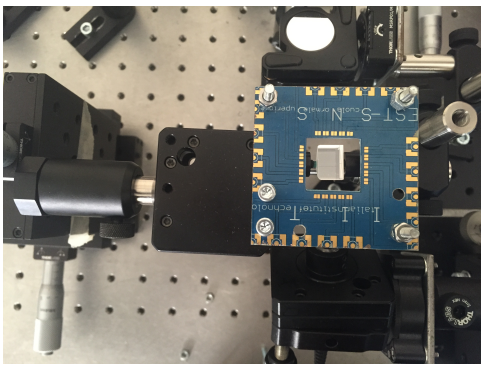

(a) Photo of the PCB used to connect the SAW-based SPR sensor to the RF generator.

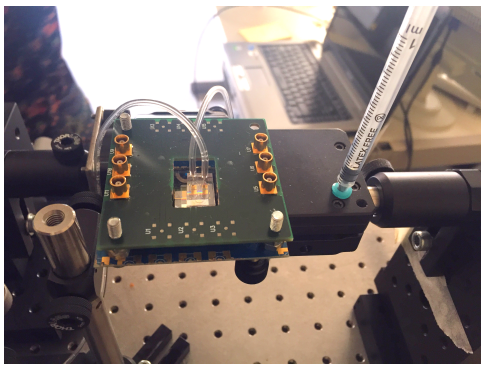

(b) SAW-based SPR sensor mounted on the PCB.
Tygon tubes are connected to a syringe (inlet) and to a waste beaker (outlet).

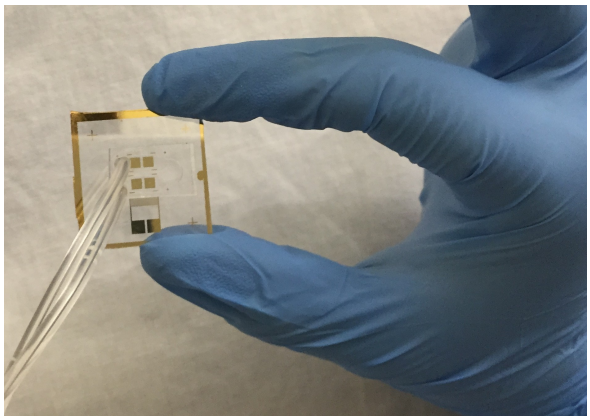

(c) Photo of a SAW-based SPR sensor.
Tygon tubes are connected to a syringe (inlet) and to a waste beaker (outlet).

Figure 3.13

A hole was made in the center of the PCB so that the chip could be put in contact with the glycerol on the prism. The positioning procedure consisted of first placing the glycerol on top of the prism. The PCB was then aligned with the prism along the x and y directions (see Figure 3.9) by cantering its hole onto the parallel face of the prism (the PCB was several *mm* above the parallel face of the prism). At this point the chip was mounted on the PCB. A second alignment was made to have the gold SPR surfaces in a good position (where it was easier to find and center the SPR gold squares with the light beam) and the stage was moved along the z-direction to place the chip in contact with the glycerol. Translation along the z-axis was made until the glycerol was completely spread over the parallel face of the prism (the same condition as in the droplet-based SPR sensor). By moving the beam along the x and y directions with the second and third mirrors it was possible to center one of the four SPR squares in the cross section of the beam. This beam alignment had to be made in the dark because by opening the diameter of the second diaphragm it was possible to see the shadow of the part of the chip illuminated on a small piece of paper between the prism and the coupler. After having moved the light beam cross-section on the desired position the diameter of the diaphragm was closed to its minimum aperture in order to take the measurements with the smallest light spot.

3.4.2 Electrical Setup

An electrical setup was used in the experiments were SAWs were involved.
After the fabrication of the chip the resonant frequency was measured using a vector network analyzer (VNA, `Agilent` E5071C), shown in Figure 3.14, connected via a coaxial cable to the pads of the IDT mounted on the PCB. The VNA provides a controlled-amplitude signal to the input of the chip over a range of frequencies, then records and displays the output of the device in terms of its magnitude and phase relative to the input as a function of frequency, i.e., it measures the elements of the scattering matrix, $S-matrix$. S_{11} is one of the most common $S-matrix$ elements used to characterize IDTs. It is the ratio between the amplitude of the wave reflected to the port of the analyzer and the amplitude of the wave emitted by it. The resonant frequency of the IDT is the frequency corresponding to the minimum of the S_{11}.
The IDT was fed by an RF generator at a set power and at its resonant frequency (at which SAWs had the necessary amplitude for the effects to be studied in the experiments). To activate the SAWs on the chip, the SAW-based SPR sensor were mounted on the PCB. The line of the PCB connected to the pads of the chip was connected to an analog signal generator (100 $kHz-6$ GHz bandwidth, MXG, `Agilent`), shown in Figure 3.14 through a coaxial cable. The cable connecting the PCB to the RF generator also connected an additional 40 dBm-amplifier. This means that the power applied to the IDT was the power set at the RF generator plus the 40 dBm supplied by the amplifier. The amplifier was powered by a 24 V power supply, shown in Figure 3.14.

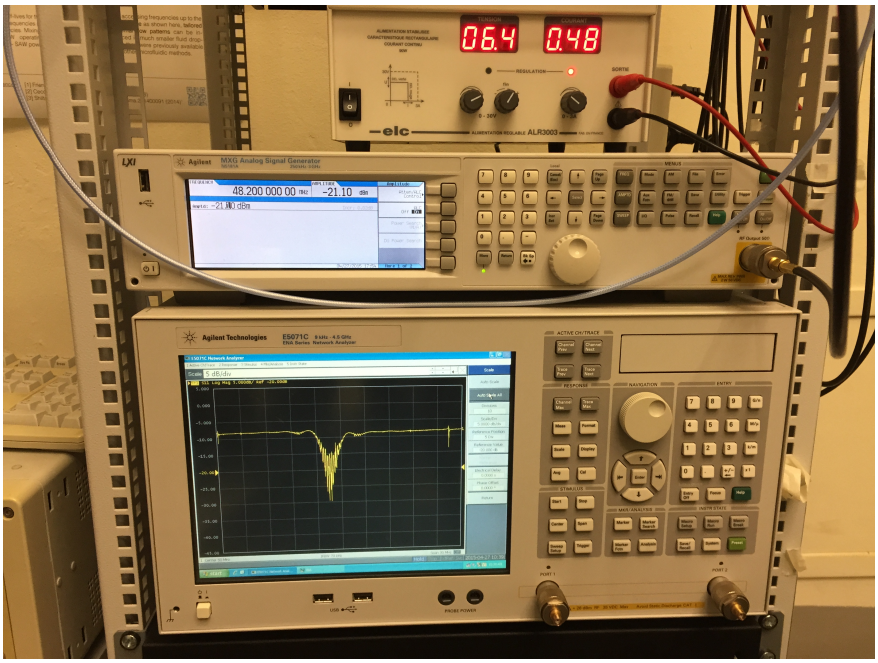

Figure 3.14: Photo of (from upper to lower) the amplifier power supply, the RF signal generator, and the VNA used for the SAW experiments. The VNA display shows the first diagonal element of the $S-matrix$ of a typical IDT used for SAW application.

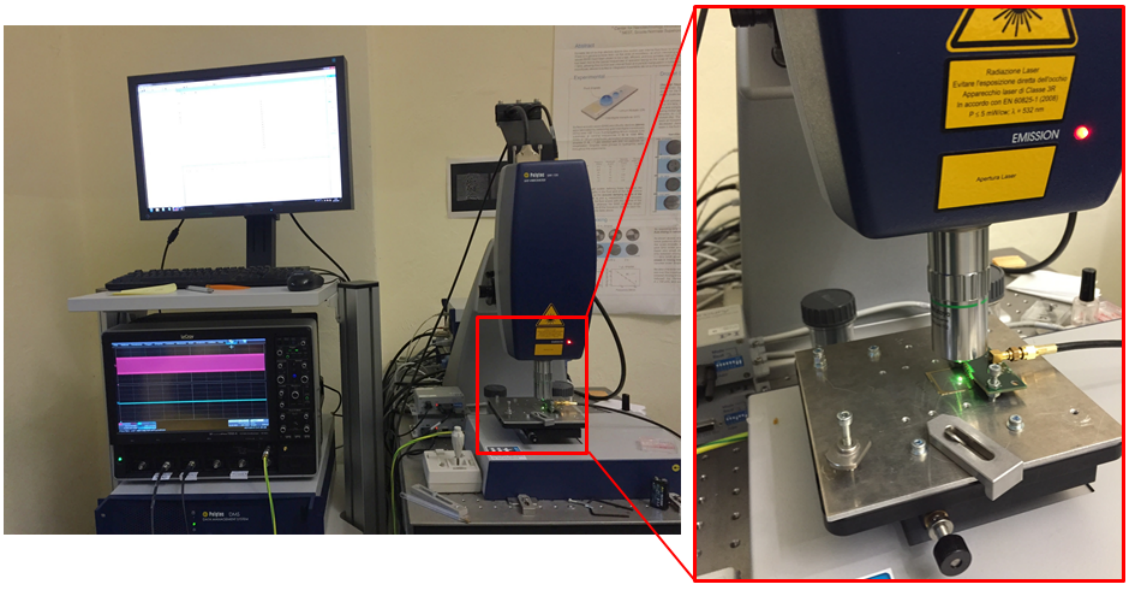

Figure 3.15: Photo of the LDV. On the left the oscilloscope is shown where the signal from the laser (in violet) can be seen. The reference signal of the RF generator is usually shown in cyan under the laser signal. On the right the LDV is shown with a zoomed section of the chip stage. The green spot is the laser spot used for the measurements.

SAW characterization was made with a laser Doppler vibrometer (LDV), shown

in Figure 3.15, which was used to quantify the amplitude of the SAWs. The laser beam from the LDV is directed at the surface of interest, and the vibration amplitude and frequency are extracted from the Doppler shift of the reflected laser beam frequency due to the surface motion.
The laser beam is split in two beams; one is directed to the surface of interest and the other is used as a reference. The vibration amplitude and frequency are extracted from the Doppler shift of the frequency of the reflected laser beam (collected on a photodiode) due to the motion of the surface.
Figure 3.16 (made with the LDV) shows the SAW propagating along the area in front of the IDT.

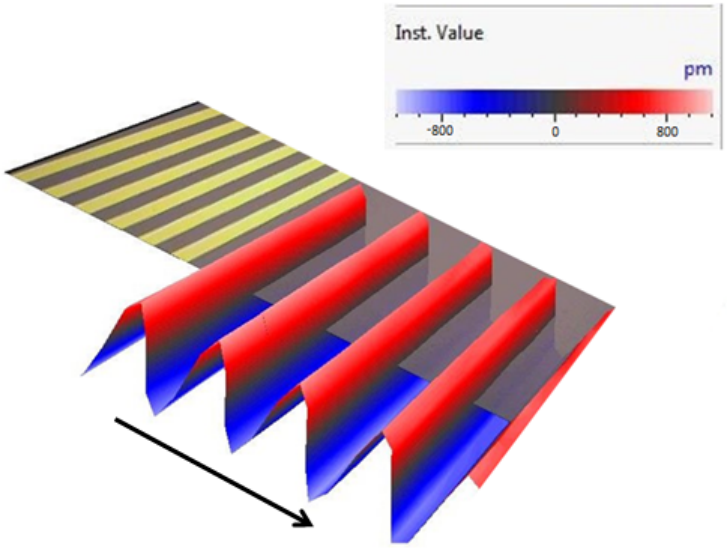

Figure 3.16: 3D representation of SAW made via an LDV scan of the substrate displacement beneath the fingers.

4 SAW-driven Biosensing: Measurements and Discussion

4.1 SPR Sensing

4.1.1 Measurement Error and Uncertainty

As already stated in the previous chapter, the SPR can be detected as a dip in the curve of the *normalized reflectivity* defined as:

$$R = \frac{I_{r,p}}{I_{r,s}} \tag{4.1}$$

where $I_{r,p}$ is the intensity of the p-polarized light reflected by the prism and $I_{r,s}$ is the intensity of the s-polarized light reflected by the prism.
On changing light wavelength at a fixed angle, and monitoring the intensity of the reflected light, the intensity of the reflected light passes through a minimum. At this wavelength, p-polarized light excites SPs causing a dip in the intensity of the reflected light. Such *resonant wavelength*, that will be denoted λ_{min}, is the main information needed to characterize the SPR system. For each curve its value was obtained by fitting the dip with the following gaussian function:

$$g(x) = a_1 \cdot e^{-\left(\frac{x-b_1}{c_1}\right)^2} + d_1 \tag{4.2}$$

where a_1 is the dip intensity, $b_1 = \lambda_{min}$, $FWHM = c_1 \cdot \sqrt{4 \ln\left(\frac{2}{\sqrt{\pi}\, c_1}\right)}$ and d_1 is the normalized reflectivity baseline.

Several aspects of the SPR measurements were considered to evaluate the error and uncertainty associated to the λ_{min} values. The main sources of instrument error were the spectrometer used to analyze the reflected spectra and the polarizer used to polarize light before it reached the sample. The spectrometer used for the experiments had a resolution of 0.3 nm and the polarization direction of the polarizer was known with an error of $\pm 2^\circ$. Light could be s-polarized or p-polarized by making it pass through the polarizer with the 284°-direction or 194°-direction, respectively, perpendicular to the laboratory plane. To estimate how the error of the polarizer direction affected the error to be associated to the λ_{min}, measurements were taken by polarizing light along the 282°, 284° and 286° directions (s-polarization) of the polarizer and by polarizing light along the 192°, 194°, 196° directions of the polarizer (p-polarizarion). Normalized reflectances were calculated at all the possible combinations of $I_{r,p}$ and $I_{r,s}$ of light polarized along the

six directions mentioned above. R curves where then fitted with eq. (4.1) in the same range of data. λ_{min} values found in this way had a standard deviation of 0.01 nm, 1 order of magnitude less than the spectrometer error and for this reason negligible.
Measurements were also made in order to evaluate the stability of the signal with respect to time. λ_{min} values of normalized reflectivities taken for 40 minutes every 10 minutes had a standard deviation of less than 0.1 nm. This uncertainty is lower than the spectrometer error and, for this reason, it could be considered negligible as in the case of the error due to the polarizer.

It was found then that the error to be associated to the λ_{min} values was 0.3 nm.

What follows is the plot of R with respect to the wavelengths of the polychromatic light used in the experiment with a droplet of DI water on top of an *droplet-based SPR sensor*:

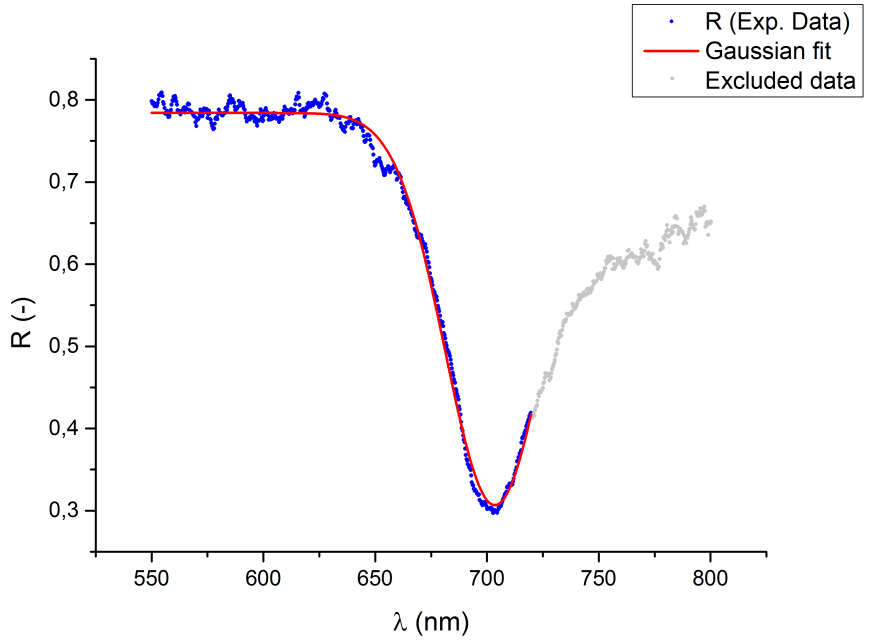

Figure 4.1: R vs. λ, 350 μL-droplet of water. Best-fit gaussian function (eq. 4.1): $a_1 = -0.477$, $\sigma_{a_1} = 0.001$, $b_1 = 703.6\ nm$, $\sigma_{b_1} = 0.1\ nm$, $c_1 = 31.5\ nm$, $\sigma_{c_1} = 0.2\ nm$, $d_1 = 0.7840$, $\sigma_{d_1} = 0.0006$ $Adj.R - square = 0.99$. The blue dots represent the data used for the fit while the grey dots the excluded ones. The red line represents the best-fit gaussian function.

A gaussian fitting function was used in the range of data where it best approximated the dip. The range of data for the fit was chosen to result in the best fit (i.e., $Adj.R - square$ as close as possible to 1).

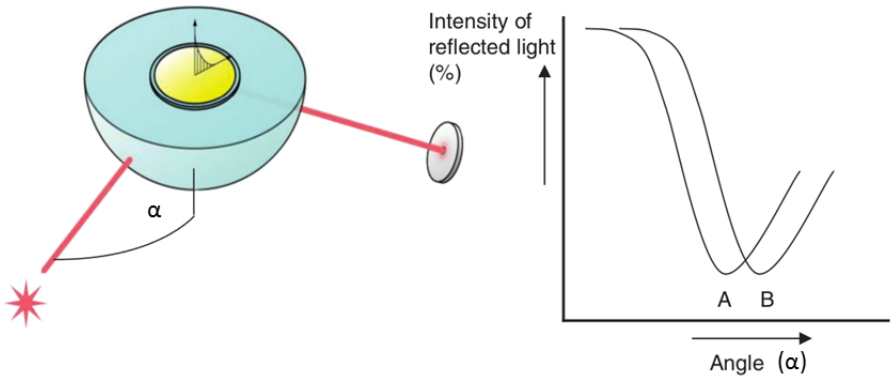

Figure 4.2: On the left, schematic of an SPR sensing experiment with angular modulation and, on the right, relative R vs. α plot. Curve B refers to a dielectric with a higher refractive index than the dielectric in A. Modified from [8].

4.1.2 Average Refractive Index and Sensitivity

The majority of SPR sensors are used with angle modulation where a monochromatic light wave excites the plasmon at different angles of incidence α. In this case, reflectivity curves R are plotted with respect to the angle of incidence of light, α. An example of such configuration and relative R curve is shown in Figure 4.2.

The R curve in Figure 4.2 has a similar trend to the curve made with the SPR sensor used with wavelength modulation in this thesis work (see Figure 4.1). In such SPR sensors a polychromatic light wave hits the chip at a given angle of incidence, conversely to what happens in SPR sensors used with angle modulation. In the configuration with wavelength modulation, the plasmon is concurrently excited by different wavelengths at a fixed angle of incidence. The use of this configuration requires a brief note about *sensitivity*.

Sensitivity is generally defined as:

$$S = \frac{\delta Y}{\delta n_d} \tag{4.3}$$

where Y denotes sensor output and n_d the refractive index of the dielectric on top of the SPR sensor. Y is the angle of incidence or the wavelength corresponding to the minimum of the normalized reflectivity in the case of angle or wavelength modulation, respectively. S is, therefore, the α_{min} or λ_{min} shift due to a change in the dielectric refractive index on top of the SPR sensor used with angle or wavelength modulation, respectively.
The refractive index of a medium strictly depends on the wavelength of the light wave that passes through it. It is correct, therefore, to talk about a refractive index shift in the angle modulation case because the light used is monochromatic. This does not hold in the case of wavelength modulation where it is no longer possible to define a δn_d. In order to compare SPR sensors with wavelength modulation using sensitivity it is necessary to define an *average refractive index* as follows:

$$\bar{n} = \frac{\sum n_i}{\sum i} \tag{4.4}$$

where $i : \lambda_i \in \{\lambda_{DIP}{}^{(i)}\}$ is the i^{th} acquisition channel of the spectrometer. The refractive index was calculated by doing the average over the refractive indices in the range of wavelengths where the dip was fitted (as Homola et al. [37]). It should be clear that the sensitivity of an SPR sensor used with wavelength modulation is strictly dependent on the system to be analyzed although in the majority of articles this problem is incorrectly circumvented by defining the refractive index of the medium for only one wavelength (conventionally 589 nm) [38].

The sensitivity of the droplet-based SPR chip was calculated for the case of water and ethanol at different concentrations. The refractive indices of water and ethanol with respect to light wavelengths were obtained by using the coefficients of the Sellmeier equation found by Kedenburg et al. in 2012 [39] (eq. 4.5)[1].

$$n(\lambda)^2 = \begin{cases} 1 + \frac{0.75831\lambda^2}{\lambda^2 - 0.01007} + \frac{0.08495\lambda^2}{\lambda^2 - 8.91377} & \text{(water)} \\ 1 + \frac{0.83189\lambda^2}{\lambda^2 - 0.00930} + \frac{-0.15582\lambda^2}{\lambda^2 + 49.45200} & \text{(ethanol)} \end{cases} \tag{4.5}$$

The refractive index of the solution at different concentrations of water and ethanol was obtained by applying the *Arago-Biot formula* [40] at each wavelength:

$$n_{12} = \phi_1 n_1 + \phi_2 n_2 \tag{4.6}$$

where, in the general case, n_i is the refractive index of liquid 1 or 2 and ϕ_i is the volume fraction of liquid 1 or 2. By substituting eq. (4.5) in eq. (4.6) it was possible to define $\bar{n}_{12}$ for the system to be studied.

Di-water and pure ethanol ($>$ 99.5%, Sigma Aldrich) were used in this experiment and each measurement was taken using a droplet of a volume of 350 μL. At this point another source of error arose: the cleaning procedure used between different measurements. A small piece of texwipe was used to remove the droplet on top of the chip after each measurement. The texwipe was put in contact with a corner of the sensor until all the solution was absorbed. After the cleaning process, a new droplet with a higher concentration was placed on top of the chip in order to take the new measurement. By measuring the SPR signal of water droplets placed on the same chip after several cleaning procedures it was shown that an error of 0.92 nm affected the measurements.
All the independent sources of error were combined resulting in a total error of 1 nm associated with the λ_{min} values. This error contains the uncertainty due to the average of the spectra, to the polariser sensitivity and to the spectrometer sensitivity. It also took into account the uncertainty caused by the cleaning procedure.

Solutions of water and ethanol were made in the cleanroom using Gilson pipettes. The volume of each mother solution was 14 mL. A P1000 Gilson pipette was used to put the 350 μL-droplet on top of the chip. Table 4.1 shows the $\bar{n}$ and λ_{min} at different concentrations of ethanol in the binary solution.

[1] $T = 20°C$

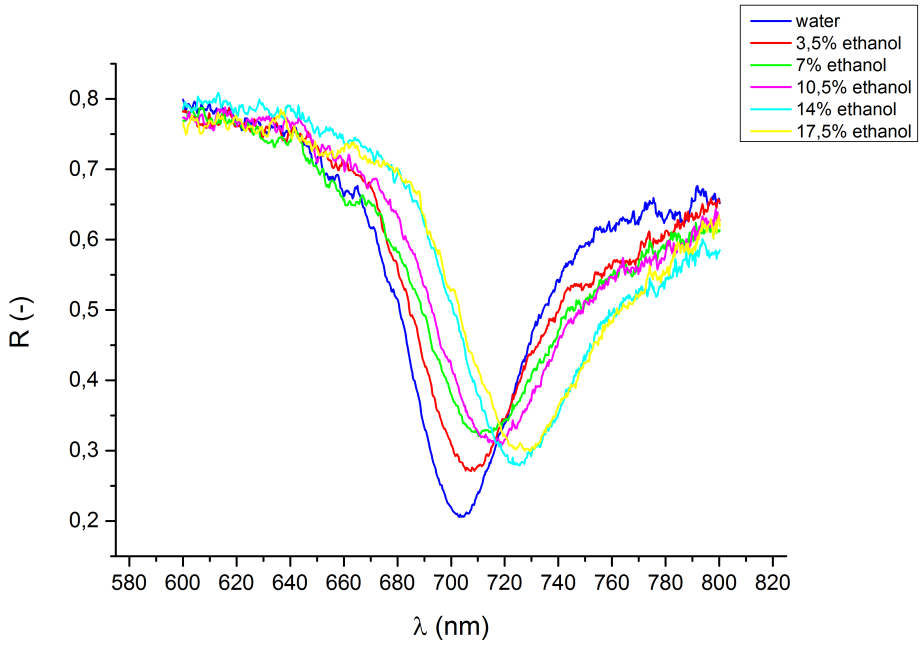

Figure 4.3: Normalized reflectivity for water and water-ethanol at different concentrations. The λ_{min} shifts towards larger wavelengths by increasing $\bar{n}$, as expected from eq. (1.14).

ϕ_{eth} [%]	$\bar{n}(RIU)$	$\lambda_{min} \pm 1$ (nm)
0	1.3414	703.7
3.5	1.3421	707.6
7	1.3431	712.2
10.5	1.3438	715.9
14	1.3462	724.5
17.5	1.3470	726.8

Table 4.1: Average refractive indices, $\bar{n}$, and resonant wavelengths, λ_{min}, of different solutions of water and ethanol at different volume fractions of ethanol, ϕ_{eth}.

Figure 4.3 shows the shift of the dip of the normalized reflectivity towards larger wavelengths by increasing the refractive index of the sample, as expected from eq. (1.14). Sensitivity of the chip is plotted in Figure 4.4 whereas the data are shown in Table 4.2. Average refractive index as discussed in §4.1.2 was used to define the curve.

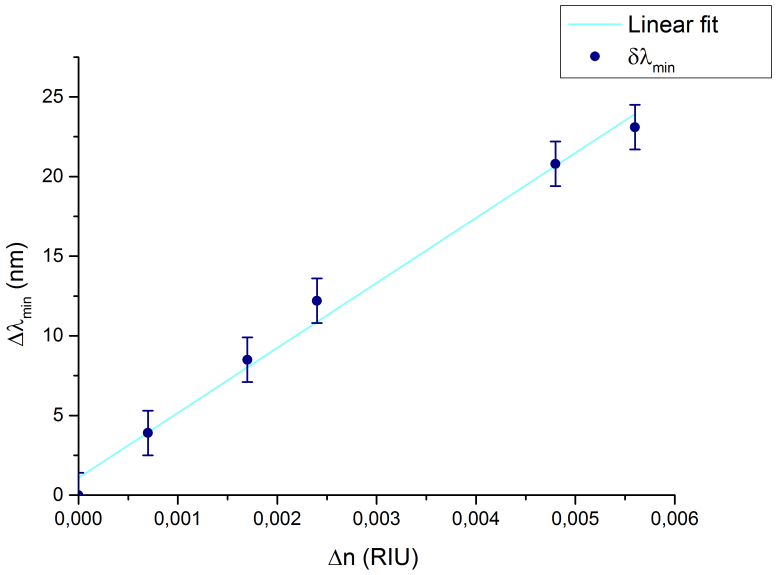

Figure 4.4: Sensitivity of the droplet-based SPR sensor in the case of water-ethanol solutions at different concentrations. The cyan curve represents the best-fit linear curve: $a = 4079.6$, $\sigma_a = 196.6$, $b = 1.1\ nm$, $\sigma_b = 0.6\ nm$, $Adj.R - square = 0.99$.

ϕ_{eth} [%]	$\delta\bar{n}(RIU)$	$\delta\lambda_{min} \pm 1.4$ (nm)
3.5	0.710^{-3}	3.9
7	1.710^{-3}	8.5
10.5	2.410^{-3}	12.2
14	4.810^{-3}	20.8
17.5	5.610^{-3}	23.1

Table 4.2: Shifts of the average refractive index, $\delta\bar{n}$, and of the resonant wavelength, $\delta\lambda_{min}$, of water-ethanol solutions at different volume fractions of ethanol, ϕ_{eth}, with respect to water.

The sensitivity has a linear trend with respect to the average refractive index shift (Figure 4.4), as expected. Data were fitted by a linear function of which a denotes the slope and b denotes the intercept. The SPR occurred at increasing wavelengths by increasing the concentration of ethanol in the binary solution. The shifts of λ_{min} at different concentrations of ethanol with respect to $\lambda_{min,water}$ has a linear trend with respect to ethanol concentrations. From the sensitivity found by the linear fit, $S = (4080 \pm 200)\ nm/RIU$, it was shown that a shift of 1 $mRIU$ in the system causes a shift of 4.1 nm of the resonant wavelength. In summary, the sensitivity of the SPR sensor for a water-ethanol system is a linear function of the refractive index shift and concentration of ethanol, as found in literature (§1.4.2) [41] [42] and as expected by simulations made with Matlab. The LOD is on the order of magnitude of $7 \cdot 10^{-4}\ RIU$, enough to detect the presence of biological binding phenomena (as will be shown in the following section).

SPR detection system used in Kretschmann configuration with angle modulation

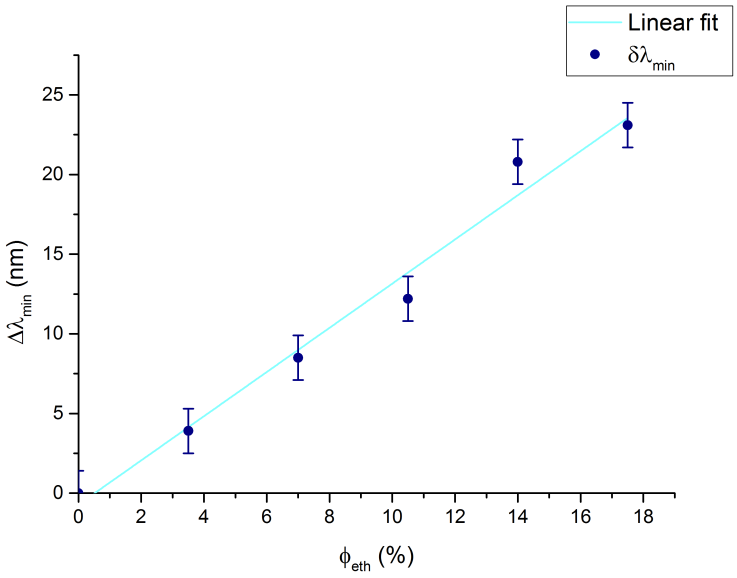

Figure 4.5: λ_{min} shift with respect to the volume friction of ethanol in the water-ethanol solution. The cyan curve represents the best-fit linear curve: $a = -0.7\ nm$, $\sigma_a = 1\ nm$, $b = 1.4$, $\sigma_b = 0.1$, $Red.R - square = 0.97$.

can also be used with intensity modulation. In this way, SPR is detected as a reflectivity variation (expressed in reflection variation units, RVU, where 1 RVU equals 100 % reflectance change) at a fixed angle and at a fixed wavelength of detection. Some works present in literature use this method [6] but Figure 4.3 shows how the SPR detection via reflectance variations may not always be optimal. For example, if in this case the SPR detection was decided to be evaluated in RVU, choosing for example to measure the intensity of reflected light at about 720 nm, the results would have been totally meaningless. In fact, the value of the reflectance would have been the same for all the curves relative to the different refractive indices except for the solutions with 7 % and 17.5 % of ethanol. Therefore, it is necessary to acquire all the reflectivity spectrum to have reliable measurements. Only α_{min} or λ_{min} for the case of Kretschmann configuration with angle or angle wavelength modulation, respectively, characterize the SPR in a solid way.

4.1.3 SPR Biosensing

The biotin-Streptavidin System

Streptavidin is widely used in molecular science owing to its highly selective and stable interaction with biotin. Other factors also contribute to the popularity of the streptavidin–biotin system, including the stability of the protein and various chemical and enzymatic biotinylation[2] methods available for use with different experimental designs [43]. A lot of results have been reported for detection [44], labelling [45] and drug delivery [46].
Streptavidin is a 53 kDa homotetramer from the bacterium *Streptomyces avidinii* that binds up to four biotin molecules (Figure 4.6) with $K_D \sim 10^{-14} M$. The protein also has high thermostability ($T_m = 112^{\circ} C$ for biotin-streptavidin) and is resistant to extreme pH, denaturing agents, and enzymatic degradation, which are important traits for use under a wide range of experimental conditions.
Biotin is a 244.31 Da vitamin, generally classified as a B-complex vitamin. Its molecular form is $C_{10}H_{16}N_2O_3S$. Biotin is stable at high temperatures ($\sim 100^{\circ}$ C) and it is soluble in acid and alkaline medium, ethanol and water. Biotin is widely used throughout the biotechnology industry to conjugate proteins for biochemical assays because, due to its small size, it does not affect the biological activity of the proteins.

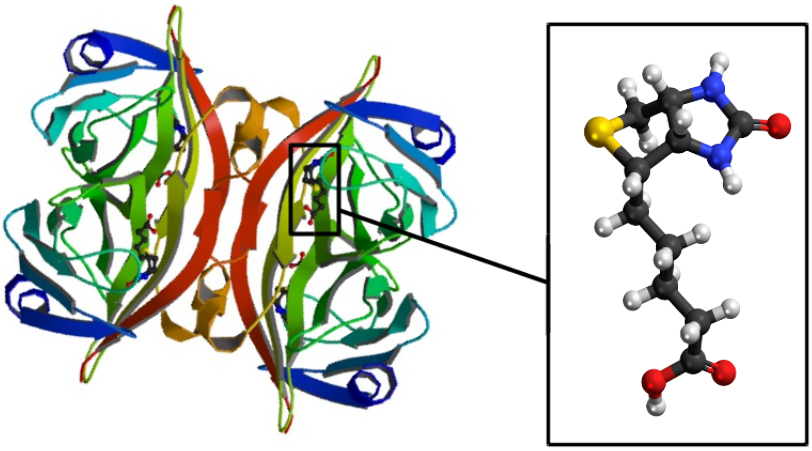

Figure 4.6: On the left, 3D representation of the Streptavidin-Biotin complex [47]. On the right, Biotin [48].

For all these reasons, streptavidin and biotin were used in this thesis work to test the sensor. Biotin-thiol in a water-ethanol solution (see §3.3) was used for the functionalization of the gold detection areas and it acted as a biorecognition element for streptavidin. Streptavidin at different concentrations in phosphate-buffered saline (PBS)[3] 1X was used as analyte for the SPR affinity experiments. PBS 1X consists in DI water with 10 mM $PO_4{}^{3-}$, 137 mM $NaCl$, and 2.7 mM KCl. In these experiments PBS was made by dissolving PBS tablets purchased from Gibco in 500 mL of DI water.

[2]The attachment of biotin to another molecule, such as a protein, is known as *biotinylation*.
[3]PBS is commonly used in biological research because its osmolarity and ion concentration match those of the human body.

Measurements in Droplets

An affinity experiment was made with streptavidin at different concentrations in PBS with the SPR gold area functionalized with biotin. Before taking the measurements it was checked that salts in PBS did not deposit on the chip within the time necessary for the experiment. The signal R was acquired for 65 minutes in 15 minute intervals. λ_{min} varied with a standard deviation of 0.5 nm, half of the error associated to λ_{min} values. Consequently salt depositions of PBS were not a problem.

The functionalization procedure discussed in §3.3 was used to attach biotin on the droplet-based SPR chip. At this point the chip was ready to be used for the experiment. The first measurement was taken with a 250 μL-droplet of PBS. It was the reference for the signal of the streptavidin which was analyzed in a PBS solution. After the measurement, the PBS was removed with the cleaning procedure discussed in the previous section and a 250μL-droplet of 250 pM streptavidin in PBS was placed on the chip using a Gilson $P1000$ pipette. After 15 minutes the measurement was taken. The biotin-streptavidin binding event is fast (within the first 3 minutes) [49] but the measurement was taken after 15 minutes to be sure that the system had reached equilibrium. 250 pM-Streptavidin-PBS solution was removed with the usual cleaning procedure and a solution with a higher concentration of streptavidin was placed on the chip. This procedure was repeated until the final streptavidin solution (25 μM) was analyzed. Results of the measurements are displayed in Table 4.3.

C (M)	$\lambda_{min} \pm 1$ (nm)
0	727.4
$250 \cdot 10^{-12}$	728.2
$2.5 \cdot 10^{-9}$	728
$25 \cdot 10^{-9}$	727.2
$250 \cdot 10^{-9}$	735.5
$2.5 \cdot 10^{-6}$	740
$25 \cdot 10^{-6}$	739.6

Table 4.3: Resonant wavelengths, λ_{min}, of streptavidin at different concentrations in PBS, C.

A solution of 25 μM streptavidin in PBS (mother solution) was used to make the other solutions of lower concentrations. 100 μL of the mother solution was diluted to made a new solution of 1 mL of volume following the simple relationship:

$$C_1 V_1 = C_2 V_2 \tag{4.7}$$

where C_1 and V_1 are concentration and volume, respectively, of the initial solution whereas C_2 and V_2 are concentration and volume of the new solution ($C_2 < C_1$). Eq. (4.7) was applied iteratively with $C_1|_{i^{th}dil} = C_2|_{(i-1)^{th}dil}$. For this reason, a relative error of 1.2 % was associated to each concentration value except for the concentration of the mother solution where the error was negligible.
In Figure 4.7 the normalized reflectivities of all the solutions are shown. As the concentration increases the dip shifts towards larger wavelengths until it reaches

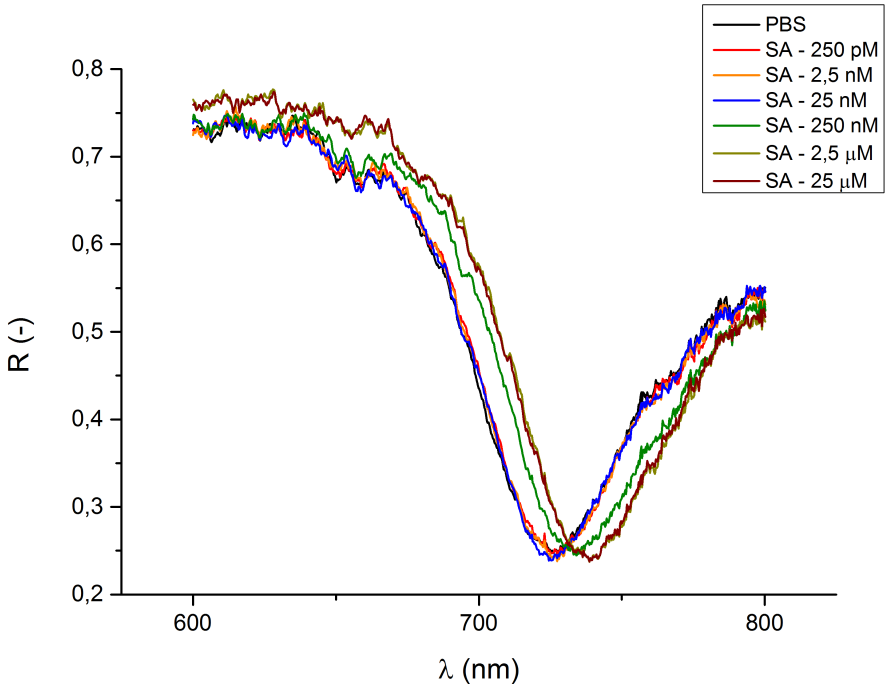

Figure 4.7: Normalized reflectivity for PBS and streptavidin at different concentrations in PBS. The λ_{min} shifts towards larger wavelengths by increasing the concentration until saturation.

2.5 μM. After that point the surface is saturated and there is no further shift. In table 4.4 λ_{min} shifts at different concentration of streptavidin are displayed.

C (M)	$\delta\lambda_{min} \pm 1.4$ (nm)
$250 \cdot 10^{-12}$	0.8
$2.5 \cdot 10^{-9}$	0.6
$25 \cdot 10^{-9}$	-0.2
$250 \cdot 10^{-9}$	8.1
$2.5 \cdot 10^{-6}$	12.6
$25 \cdot 10^{-6}$	12.2

Table 4.4: λ_{min} shifts at different concentrations of streptavidin in PBS.

These data were then fitted with the Langmuir equation (1.29). The plot of the λ_{min} shifts with respect to the streptavidin concentration in PBS is shown in Figure 4.8 with the best-fit curve in cyan. The dissociation constant K_D and the maximum binding capacity B_{max} (defined in §1.4.2) were obtained from the fit (see §1.4.2). In literature the association constant K_A (the inverse ratio of K_D) is used to describe the binding event. Using equations (1.27) and (1.28), $K_{A,surf} = (5.5 \pm 2)\ 10^6 M^{-1}$ was extracted from the fit. Its value is in agreement with typical values found in literature (e.g., $K_A = (7.3 \pm 0.2) 10^6 M^{-1}$, Tang et al. 2006 [50]). Moreover, the limit of detection is between 25 nM and 250 nM. This results are comparable with the state of the art and even slightly better than the results of some published local-

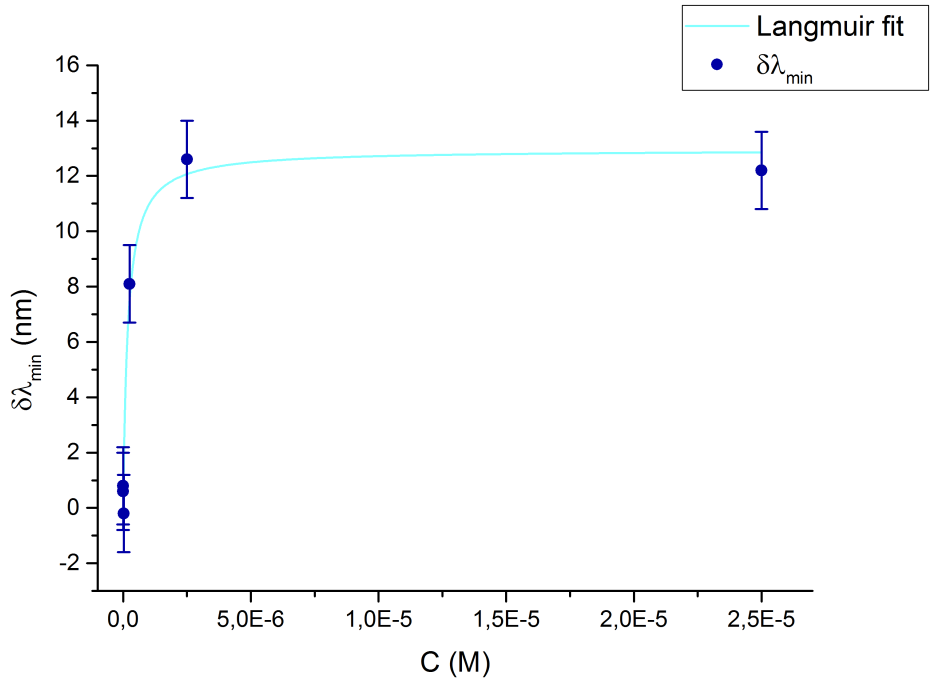

Figure 4.8: λ_{min} shifts at different concentrations of streptavidin in PBS. The cyan line represents the best-fit Langmuir function (eq. 1.29): $K_{D,surf} = 1.82 \cdot 10^{-7}\ M$, $\sigma_{K_{D,surf}} = 0.68 \cdot 10^{-7}\ M$, $B_{max} = 12.9\ nm$, $\sigma_{B_{max}} = 0.89\ nm$, $Adj.R - square = 0.96$.

ized SPR-biosensor (e.g., Arai et al. [38]).

Measurements in Channels

Measurements of 2.5 μM streptavidin in PBS (1X) were taken using the μchannel SPR chip (§3.2). First of all, a solution of water and ethanol (10:1) was injected into the microchannel using a disposable sterilized 2 mL-syringe. After filling the microchannel, the measurements were taken. Air was then injected in order to empy the microchannel and to inject the biotin solution for the functionalization of the gold SPR areas. The solution was left for approximately 20 minutes to be sure that the functionalization was complete (§4.1.3). PBS was then injected to measure the reference for the streptavidin. Streptavidin measurements were taken repeatedly for about 1 hour and a half after the injection in order to check if it was possible to follow the kinetics of the binding event. In this time the λ_{min} value was stable within the error of 1 nm, concluding that it was not possible to follow the kinetics. Therefore, the data reported are the result of the mean over all the measurements taken for approximately an hour after injection.

A plot of the experimental results described above is shown in figure 4.10. Each column represents the injection with respect to time of the solution to be analyzed: water-ethanol, biotin in water-ethanol, PBS and streptavidin in PBS, in this order. The column widths specify the mean over the λ_{min} values taken in the time between the injection of different solutions. Figure 4.9 shows a schematic of the SPR phenomena occurring on the chip during the different steps of the experiment. Typical normalized reflectivity spectra are also shown. Table 4.5 shows the average resonant wavelengths in the case of biotin and streptavidin and their shift from the λ_{min} of the water-ethanol solution and PBS which were the references for biotin and streptavidin, respectively.

$\lambda_{min,W.-E.}$ (nm)	$\bar{\lambda}_{min,biot.}$ (nm)	$\delta\lambda_{min}$ (nm)
744.6 ± 1	748 ± 1	3.3 ± 1.4
$\lambda_{min,PBS}$ (nm)	$\bar{\lambda}_{min,strept.}$ (nm)	$\delta\lambda_{min}$ (nm)
736.1 ± 1	741.8 ± 1	5.7 ± 1.4

Table 4.5: Resonant wavelengths of the water-ethanol solution (10:1), $\lambda_{min,W.-E.}$, and PBS, $\lambda_{min,PBS}$, references, respectively, for the average resonant wavelengths of biotin, $\bar{\lambda}_{min,biot.}$, and streptavidin, $\bar{\lambda}_{min,strept.}$. resonant wavelength shifts, $\delta\lambda_{min}$, are displayed for these three cases.

$\delta\lambda_{min}$ in the case of 2.5 μM is about half of the value obtained in the droplet ((12.6 ± 1.4) nm). This difference may be explained as follows. The beam cross-section was less than 1 mm^2 after the first diaphragm but when it reached the chip it was about 6 mm^2, larger than the gold SPR area to be analyzed. For this reason about 36% of the signal was noise. 36% of the light spot did not excite SP and for this reason did not contribute to the signal causing a noisier dip and a shift of the non-resonant baseline.

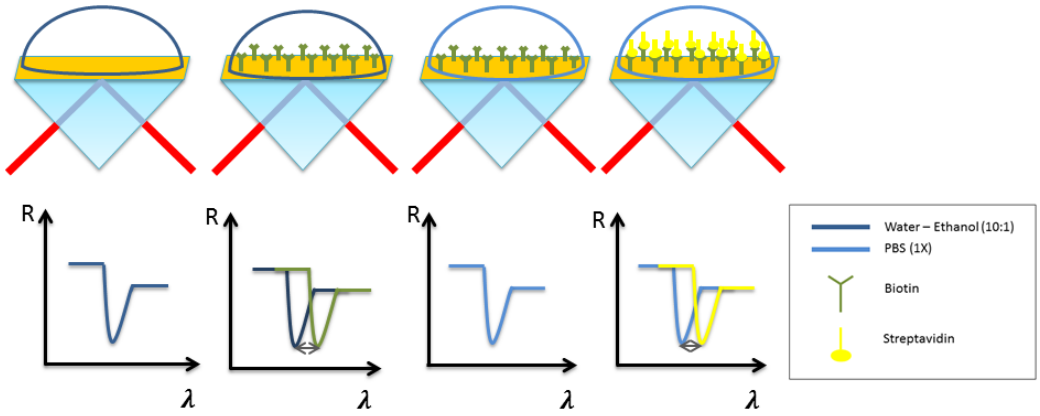

Figure 4.9: Schematic of the SPR phenomena occurring on the chip during the different steps of the experiment. Typical normalized reflectivity spectra are shown.

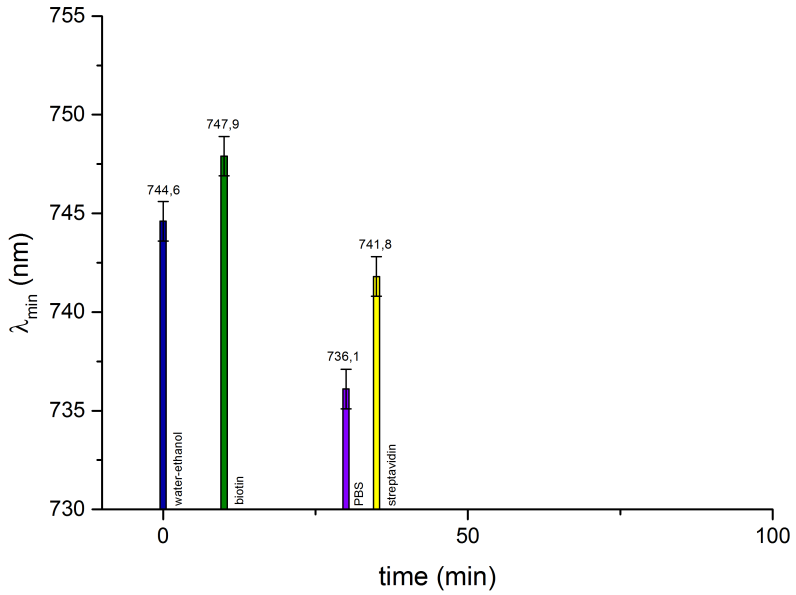

Figure 4.10: Diagram of the resonant wavelengths, λ_{min}, for water-ethanol (10:1), biotin in water-ethanol (1 mg/mL), PBS (1X) and streptavidin in PBS (1 μM). Each column with these four values is plotted in correspondence of the time at which the injection of the solution in question was made.

4.2 SAW-driven Biosensing

4.2.1 Acoustic Characterization

Before taking measurements with the SAW active it was necessary to characterize its excitation and propagation on the piezoelectric substrate of the chip. At this stage the microchannel had not yet been bonded on the chip.
The biosensor was mounted on a PCB and the line connected to the pads of the chip was then attached to the VNA. Figure 4.11 shows the diagonal term S_{11} of the S-matrix of a SAW-based SPR chip. A dip of about 14 dBm can be seen in correspondence with the resonant frequency at 48.1 MHz.

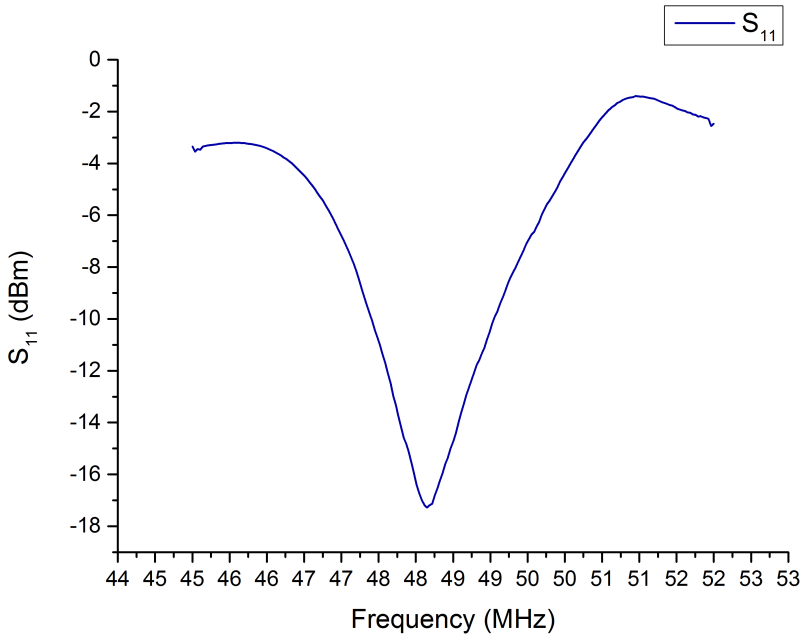

Figure 4.11: First diagonal element of the S-matrix, S_{11}, with respect to frequency for a SAW-based SPR chip. SAW excitation frequency was 48.1 MHz, in correspondence of which the reflected amplitude decreased by 14 dBm.

The working frequency of the IDT is less than expected from the chip design. This is due to the mass loading effect of the gold IDT on top of the piezoelectric substrate [17]. Some scans of the *SAW area* in front of the IDT (see SAW-based SPR sensor design in §3.2) where made by the LDV at different powers of the RF generator in order to find a SAW amplitude of 800 pm. The average power at which the SAW amplitude on the SAW-based SPR sensor was 800 pm was -21.6 dBm. It means that the sensor was typically powered with 18.4 dBm (i. e., 69.1 mW).

SAW amplitude along its direction of propagation and perpendicular to its direction of propagation is shown in Figures 4.12a and 4.12b, respectively. The SAW amplitude has two maxima in correspondence of the two edges of the IDT. This is the typical transverse fingering instability of IDTs due to Fresnel diffraction of the acoustic wave as a consequence of the finite aperture of the electrodes used to generate the SAW [24].

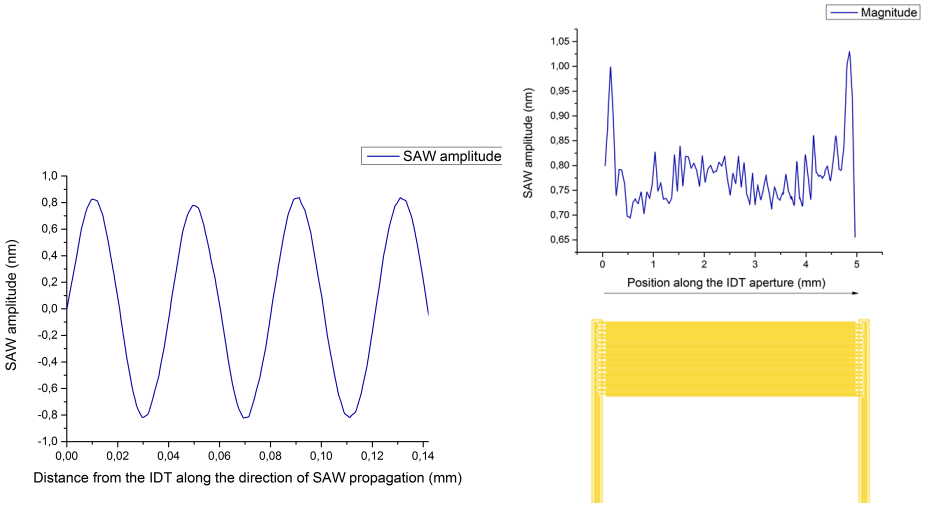

(a) SAW amplitude along its direction of propagation.

(b) SAW amplitude in the Fresnel area, right after the IDT, with typical ripples across its profile.

Figure 4.12: SAW amplitude along (a) and perpendicular to (b) its propagation direction.

Simulations and measurements made in a previous work [34] show that an optimal streaming occurs at an amplitude of 800 pm. Figure 4.13a shows the 2D projection of the 3D streaming effect of SAW in this case. The picture shows that there are two vortices at the borders of the chamber. Due to their different geometry, the vortex on the left is counterclockwise whereas the one on the right is clockwise. The vortex in the central area in front of the PDMS wall is due to the vertical streaming effect, in a plane perpendicular to the chip surface. The velocity field made with particle image velocimetry (PIV) confirms the absence of SAW in the second chamber. It shows that the SAW velocity decreases from the second half of the SAW chamber and goes to zero before the second chamber. The fluid velocity goes from 2000 $\mu m/s$ in the center of the vortexes to 600 $\mu m/s$ at its half. Figure 4.13b shows the velocity field in the left corner of the chamber.

To summarize, this chip (all the distances between the various components in all directions, the shape of each component and the material used) was designed in order to have a specific acoustic streaming, at a set SAW amplitude, with known streamlines and velocity field. SAW streaming in the fluid within the microchannel was completely characterized by the velocity field and streamlines of the fluid, as it can be seen in Figure 4.13a and 4.13b. Such an acoustic streaming is completely reproducible, contrary to the inspiring previous work published by Renaudin et al. [6] where the fluid was simply placed in a microfluidic well and SAW-induced streaming was not characterized quantitatively.

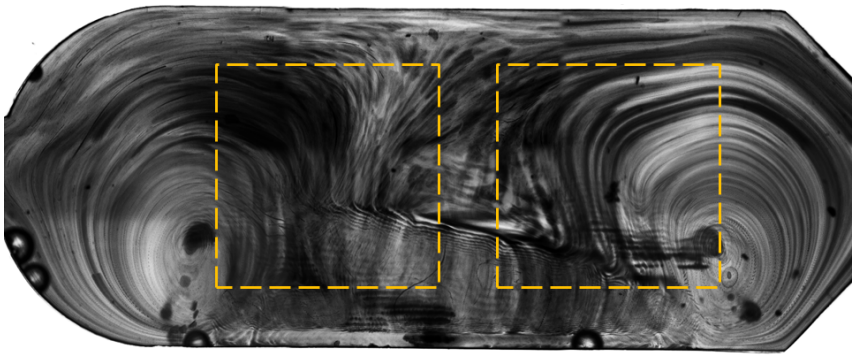

(a) Streamlines made by tracing microparticles in di-water (1 mM) in the SAW chamber with an optical microscope (300 fps) [34]. The areas corresponding to the SPR gold squares are defined by the yellow squares.

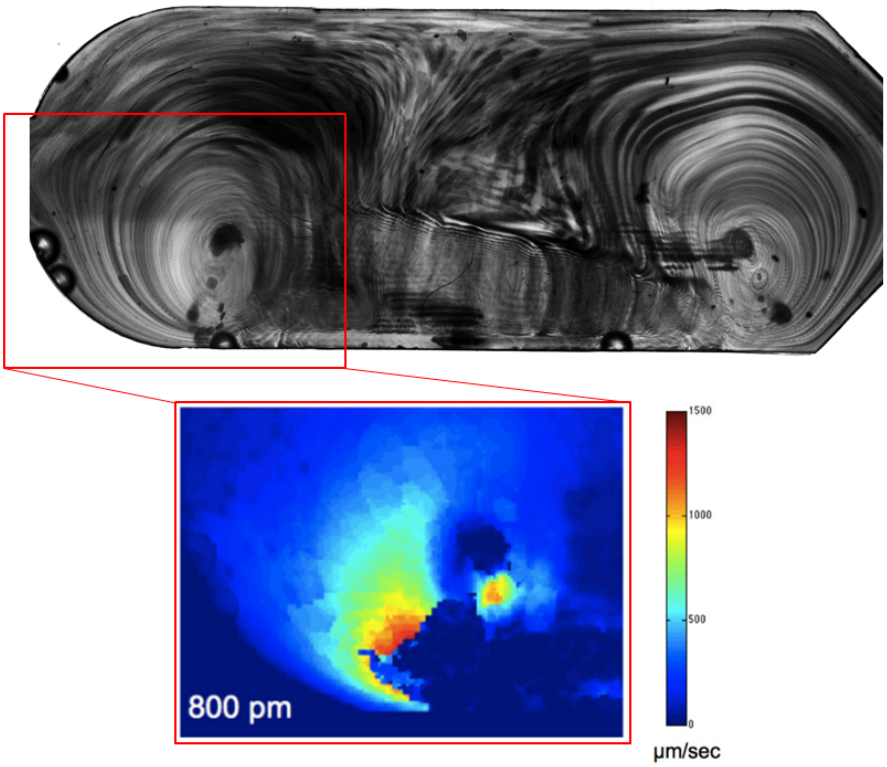

(b) Velocity field map in the left corner area of the microchannel during the acoustic streaming induced by SAWs of 800 pm-amplitudes.

Figure 4.13: Images of the streamlines (a) and velocity field map (b) of di-water in the microchannel with SAW active. [34]

4.2.2 Heat Characterization

The activation of SAW on the piezoelectric substrate of the chip results not only in streaming of the fluid within the microchannel but also in the heating of the sample. This means that when the SAW is active, temperature effects must also be taken into account. An IR camera (FLIR A655sc) was used to measure the temperature of the piezoelectric substrate during the activation of SAWs until the equilibrium temperature was reached. In particular, the temperature was measured from the substrate below the *SAW area* and the *heating-only area* under the PDMS microchanel (see chip description in §3.2 and Figure 3.6).

The equilibrium temperature was reached after about 8 minutes. The temperatures of the substrate $T_{substr.}$ under the *heating-only area* and under the *SAW area* at equilibrium were approximately the same: $T_{substr.,heat.} = (41.4 \pm 0.1)°C$ and $T_{substr.} = (42.1 \pm 0.1)°C$ with an accuracy of $\pm 2°C$. Figures 4.14 and 4.15 show the heating of the substrate following SAW activation ($t = 0$ *sec*) until equilibrium. The temperatures displayed in these two plots are the mean over the rectangle areas shown in the insets. They show images taken by the IR camera after 0 *sec*, 50 *sec*, 100 *sec*, 300 *sec* and 595 *sec* from SAW activation.

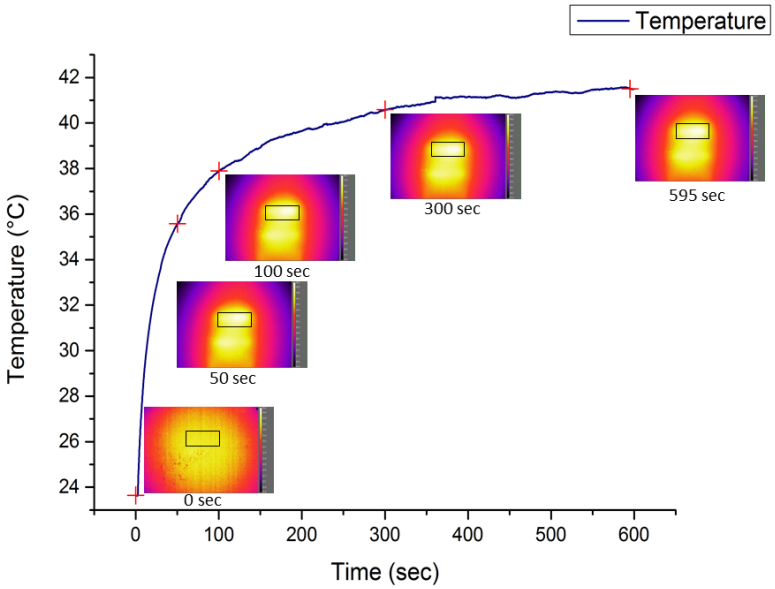

Figure 4.14: Heating of the LN substrate under the microchannel with respect to time since SAW activation ($t = 0$). The insets show five images from the thermocamera at 0 *sec* , 50 *sec*, 100 *sec*, 300 *sec* and 595 *sec* after SAW activation. Temperature values are the mean over the area shown by the black rectangle in the insets, under the second chamber where only the heating effect of SAW was present.

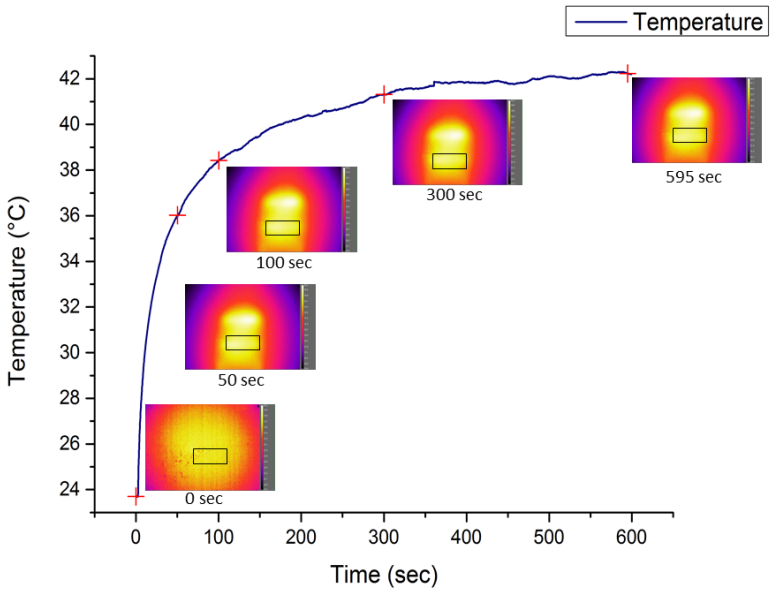

Figure 4.15: Heating of the LN substrate under the microchannel with respect to time since SAW activation ($t = 0$). The insets show five images from the thermocamera at 0 *sec* , 50 *sec*, 100 *sec*, 300 *sec* and 595 *sec* after SAW activation. Temperature values are the mean over the area shown by the black rectangle in the insets, under the first chamber where SAW was present.

The LN substrate acts as a heat sink for the solution in the microchannel at equilibrium and for this reason the temperature of the fluid inside the microchannel can be considered equal to that of the substrate at equilibrium.

The characterization of the SAW-induced heating effect was the most critical part in Renaudin et al. [6] (whose work was shown in §2.3.2). They monitored the reflectance variations in water due to 5 *sec* SAW pulses (of unknown amplitude) at different powers (from 28 dBm to 37 dBm). The relaxation time depended on the power and was defined as the time necessary for the system to have the same reflectance value as the reflectance value with the SAW inactive. This kind of heating characterization has two main problems: first, the water system is different from the avidin solution system (in which heating can induce different effects, e.g., different relaxation times or even it is possible that the signal does not restore), second, the powers involved could really change or even prevent the binding kinetics of biotin-avidin. For this SAW-based SPR sensor it was found that a power of about 18.4 dBm (which corresponds to about 69 mW) induced an increase in temperature of the substrate under the microchannel of about $3°C$ after the first 5 *sec*. The best configuration (in which the fastest binding kinetics was induced) found by Renaudin was with a power of 36 dBm (which corresponds to about 4 W), twice the power used for this experiment in dBm units, which corresponds to about 58 times the power used for this experiments in mW units. In a work published by Lo et al. [51] it was shown that the rupture point of the biotin-avidin bond occurs at around $43°C$. The temperature induced by the SAW pulse in the case of Reanudin et al. was likely comparable to or even higher than this critical value. When such temperature values are involved results must be analyzed very

critically. Therefore, the side heating effect of SAW must be treated carefully in order to be sure, or at least to have a qualitatively idea of the physical state of biological system to be studied and that a possible increase of the signal (as it will be shown in the next sections) can only be attributed to the SAW streaming effect.

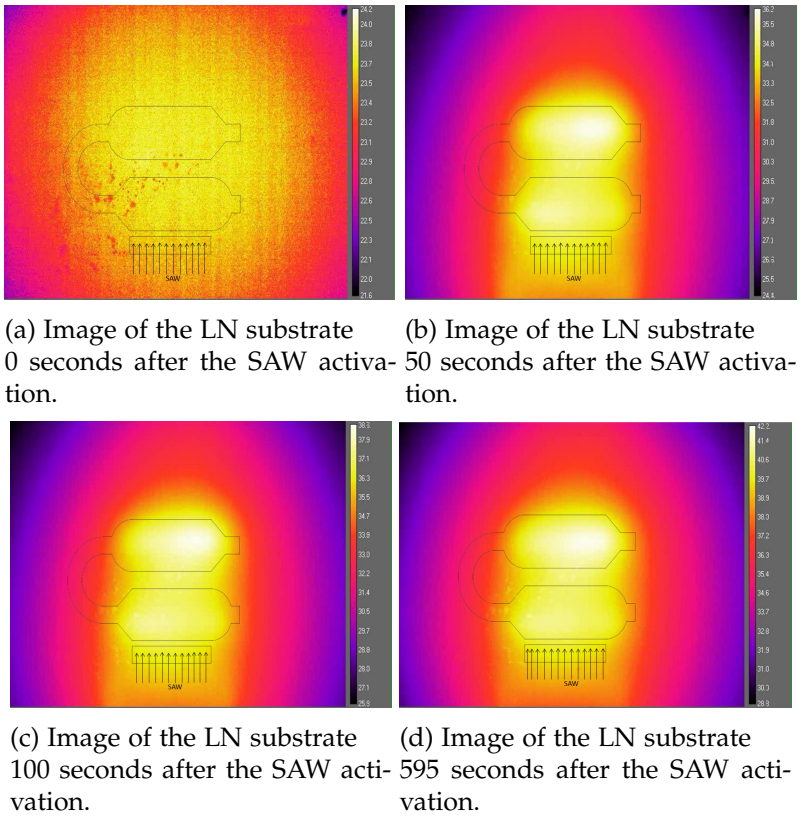

(a) Image of the LN substrate 0 seconds after the SAW activation.

(b) Image of the LN substrate 50 seconds after the SAW activation.

(c) Image of the LN substrate 100 seconds after the SAW activation.

(d) Image of the LN substrate 595 seconds after the SAW activation.

Figure 4.16: Images from the IR camera of the LN substrate of the chip under the microchannel area at different times after SAW activation. A schematic of the microchannel is superimposed on each image. SAW direction from IDT is specified by the arrows.

4.2.3 The SAW-enhanced SPR Biosensor

Studies on the SAW heating effect

As described in §4.1.3, Figure 4.17 depicts the SPR-shifts of the experiment made in the heating only area of the channel with the SAW activated. Functionalization and binding events of biotin-streptavidin were studied to detect changes in the resonanant wavelengths over time. In this case, as in the previous, it was not possible to study the kinetics of the functionalization or of the binding event.

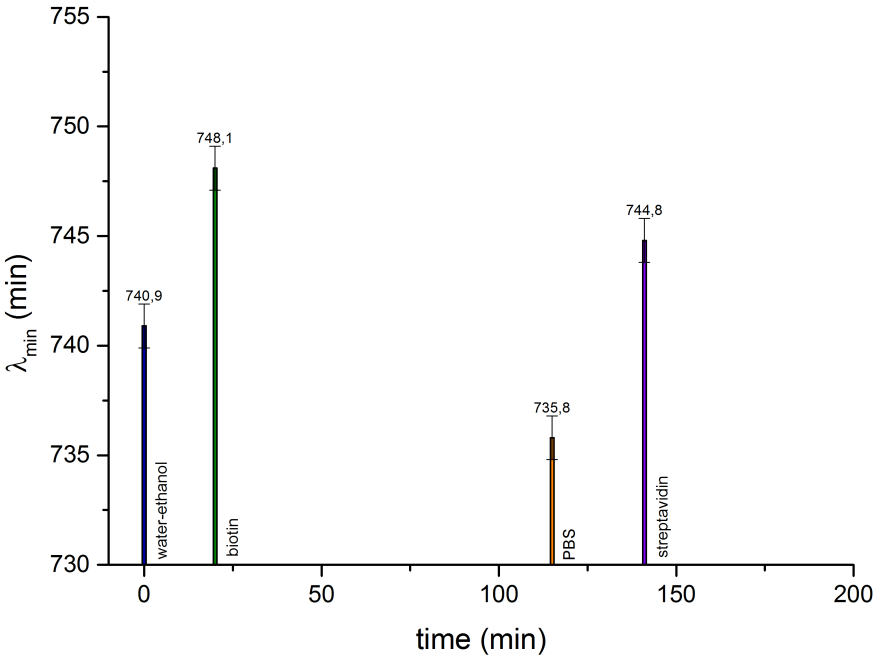

Figure 4.17: Diagram of the λ_{min} with respect to time in the case of a solution of water and ethanol (10:1), biotin in such solution (1 mg/mL), PBS (1X) and streptavidin in PBS (1 μM) (also after refresh). Measurements were taken in the "heating only area" (§3.2).

In this case the time between the injection of biotin after the water-ethanol solution or of the streptavidin after PBS could not be arbitrary because it was necessary to wait for the stabilization of the signal with respect to temperature. The refractive index is directly proportional to density and density itself depends on temperature. By increasing the temperature from $22°C$ to $42°C$ the refractive index of water and ethanol decreased by 2.41 $mRIU$ and 8.2 $mRIU$, respectively, at a wavelength of 589 nm [52] [53]. After 10 minutes the signal was stable, however the measurements were taken after 20 minutes to be sure that the system was at equilibrium.

$\lambda_{min,W.-E.}$ (nm)	$\bar{\lambda}_{min,biot.}$ (nm)	$\delta\lambda_{min}$ (nm)
740.9 ± 1	748.1 ± 1	7.2 ± 1.4
$\lambda_{min,PBS}$ (nm)	$\bar{\lambda}_{min,strept.}$ (nm)	$\delta\lambda_{min}$ (nm)
735.8 ± 1	744.8 ± 1	9 ± 1.4

Table 4.6: Resonant wavelengths of the water-ethanol solution (10:1), $\lambda_{min,W.-E.}$, and PBS, $\lambda_{min,PBS}$, references for the average resonant wavelengths of biotin, $\bar{\lambda}_{min,biot.}$, and streptavidin, $\bar{\lambda}_{min,strept.}$, respectively. resonant wavelength shifts, $\delta\lambda_{min}$, are displayed for these three cases.

Table 4.6 shows the average λ_{min} and λ_{min} shiftsvalues over time of biotin and streptavidin with their respective reference, water-ethanol solution and PBS.

Studies on the SAW streaming effect

Figure 4.18 depicts the results of the experiment made in the channel area where the streaming and heating effects of SAWs were present. Measurements were taken at the same times as with the previous experiment. Table 4.7 shows the average λ_{min} values over the time in which each solution was in the microchannel and the λ_{min} shifts of biotin and streptavidin with their respective reference, water-ethanol solution and PBS.

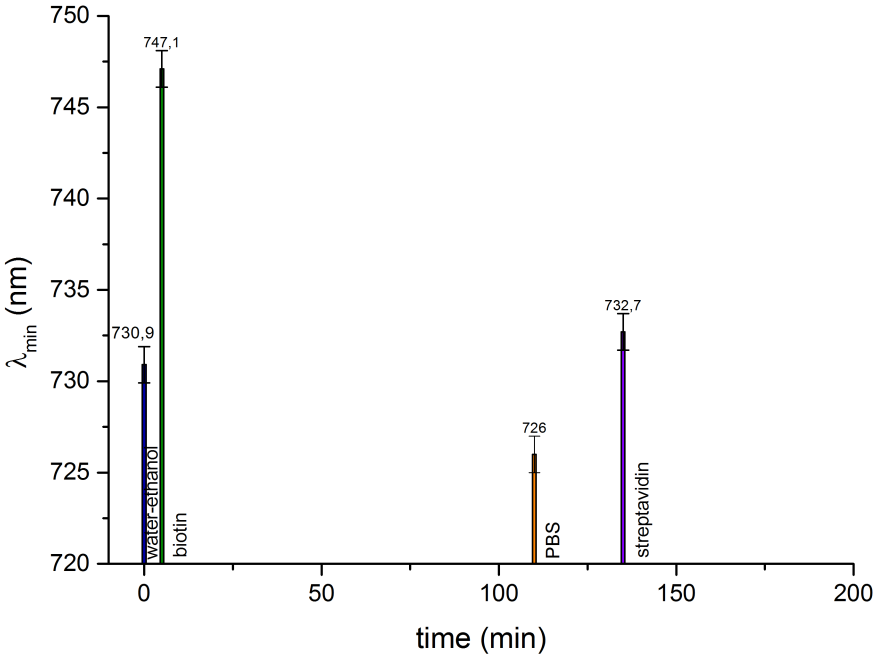

Figure 4.18: Diagram of the resonant wavelengths, λ_{min}, with respect to time in the case of water-ethanol solution (10:1), biotin in water-ethanol (1 mg/mL), PBS (1X) and streptavidin in PBS (1 μM). Measurements were taken in the "SAW area" (§3.2). Each column with these four values is plotted in correspondence of the time at which the injection of the solution in question was made.

$\lambda_{min,W.-E.}$ (nm)	$\bar{\lambda}_{min,biot.}$ (nm)	$\delta\lambda_{min}$ (nm)
730.9 ± 1	747.1 ± 1	16.2 ± 1.4
$\lambda_{min,PBS}$ (nm)	$\bar{\lambda}_{min,strept.}$ (nm)	$\delta\lambda_{min}$ (nm)
726 ± 1	732.7 ± 1	6.7 ± 1.4

Table 4.7: Resonant wavelengths of the water-ethanol solution (10:1), $\lambda_{min,W.-E.}$, and PBS, $\lambda_{min,PBS}$, references for the average resonant wavelengths of biotin, $\bar{\lambda}_{min,biot.}$, and streptavidin, $\bar{\lambda}_{min,strept.}$, respectively. resonant wavelength shifts, $\delta\lambda_{min}$, are displayed for these three cases.

Gold Surface Functionalization

The effect of SAW streaming on surface functionalization has not previously been studied. Renaudin at al. [6] only studied the effect on the binding event between avidin and biotin, but not on the functionalization process itself. Measurements were made in the channel without SAW, and with SAW in the heating and streaming areas separately. Both heating and streaming could affect the functionalization process. With these experiments the two effects were separated in order to understand the real effect of streaming on the functionalization. 1 mg/mL biotin-thiol in solution of water and ethanol (10:1) was analyzed.

Comparison of the Methods

$\Delta\lambda_{min}$ of the biotin with respect to water-ethanol in the channel, the heating effect of SAW, and the heating and streaming effect of SAW are shown in Table 4.8.

	$\Delta\lambda_{min}(nm)$	$SE(nm)$
SAW inactive	3.3 ± 1.4	0.05
Only heating	7.2 ± 1.4	0.23
Heating + Streaming	16.2 ± 1.4	0.43

Table 4.8: Resonant wavelength shifts of biotin in water-ethanol (1 mg/mL) with respect to water-ethanol only, $\Delta\lambda_{min}$, with their relative standard error, SE, when SAW was not active, in the microchannel where there was only the heating effect of SAW and in the microchannel where both heating and streaming by SAW were present.

Figure 4.19 (a), (b) and (c) show the shifts of the R biotin curve to the R water-ethanol curve in the three cases. In Figure 4.19 (d) the mean value of λ_{min} in the three cases are shown.

The streaming resulted in a greatly improved SPR shift which suggests a more efficient functionalization. λ_{min} in the case with SAW is about 5 times λ_{min} in the case without SAW. This enhancement of the functionalization can be attributed only to the streaming effect of SAW because the heating effect, studied independently, resulted in an enhancement of the functionalization that was much less than in the SAW case. λ_{min} in the heating-only area is about 2.2 times λ_{min} with SAW inactive and about 2.2 times less than λ_{min} in the SAW case. Kawasaki et al. [54] and Yamada et al. [55] had already found that the increasing of the temperature above $25^{\circ}C$ improved the attachment of thiol on gold. The streaming effect of SAW, though, improves the functionalization even further. SAW streaming makes biotin move chaotically in the water-ethanol solution increasing the probability of attachment whereas when SAW in not active, biotin diffuses slowly in the solution.

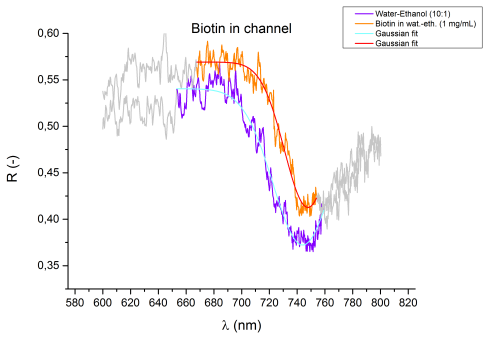

(a) R vs. λ of a typical measurement taken in the case of water-ethanol (10:1) and biotin in water-ethanol (1 mg/mL) on chip without SAW.

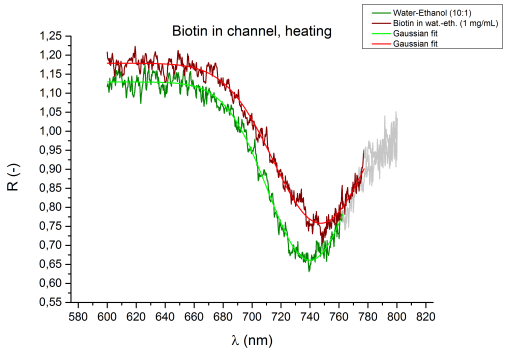

(b) R vs. λ of a typical measurement taken in the case of water-ethanol (10:1) and biotin in water-ethanol (1 mg/mL) on chip in the area where only the heating effect of SAW was present.

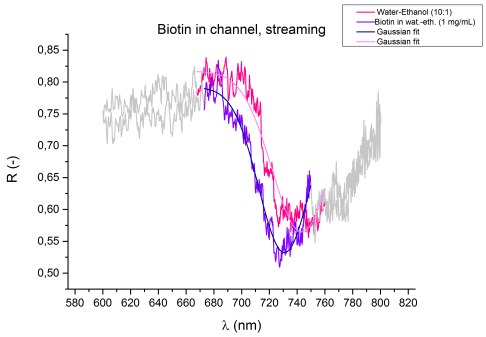

(c) R vs. λ of a typical measurement taken in the case of water-ethanol (10:1) and biotin in water-ethanol (1 mg/mL) on chip with SAW.

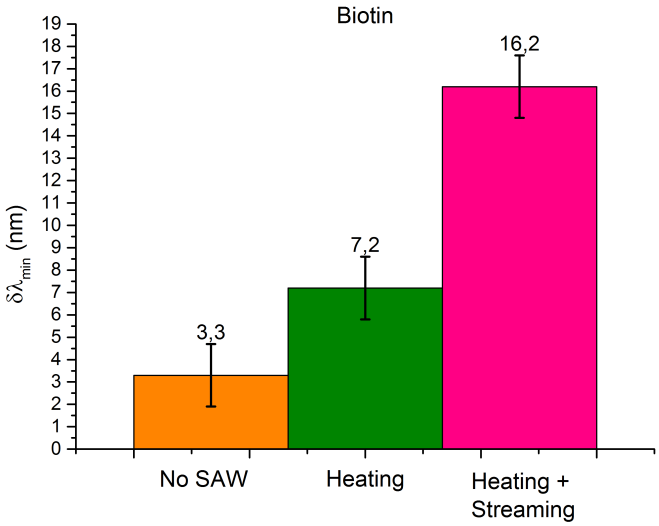

(d) Average resonant wavelength shift of biotin in water-ethanol (1 mg/mL) to water-ethanol only in the case without SAW, with the heating effect of SAW, and with SAW, respectively.

Figure 4.19: Comparison of the normalized reflectivities of water-ethanol solution and biotin in water-ethanol (1 mg/mL) in three cases: (a) without SAW, (b) in the area where only the heating effect of SAW was present and (c) with SAW. Data in grey were not used for the gaussian fit (see §4.1.1). Figure (d) shows the comparison between the average $\delta\lambda_{min}$ in these three cases.

Streptavidin Detection

The same studies done on the functionalization were made on the binding of streptavidin with biotin. The case without SAW in channel and with SAW separating heating and streaming effect were made. 2.5 μM streptavidin in PBS was analyzed.

Comparison of the Methods

In the case of streptavidin the role of the SAW streaming and heating had an unexpected effect. Table 4.9 shows the average λ_{min} values over the time in which the streptavidin solution was in the microchannel and the λ_{min} relative to PBS in the three cases: where SAW was inactive, where only the SAW heating effect was present, and where both SAW streaming and heating were present.

	$\Delta\lambda_{min}(nm)$	$SE(nm)$
SAW inactive	5.7 ± 1.4	0.20
Only heating	9.0 ± 1.4	0.34
Heating + Streaming	6.7 ± 1.4	0.16

Table 4.9: Resonant wavelength shifts of streptavidin in PBS (2.5 μM) with respect to PBS only, $\Delta\lambda_{min}$, with their relative standard error, SE, when SAW was not active, in the microchannel where there was only the heating effect of SAW and in the microchannel where both heating and streaming by SAW were present.

Data show that there is not an enhancement in the use of SAW. The shifts due to streptavidin-biotin are approximately the same. In this case there are many different aspects that must be taken into account. First of all the three measurements were made with three different functionalizations, the worst in the case of the inactive SAW and the best in the case where the SAW streaming effect was present. The small increase of the λ_{min} mean value in the heating case with respect to the case where SAW was inactive could be explained with the better functionalization that was made in that case. Moreover, as already stated, it was shown that the binding force between streptavidin and biotin descreases by increasing the temperature and it is almost null around $43°C$ [51]. However, these measurements were not taken in solution and for this reason this system is not exactly comparable to ours, but in any case it gives an idea of the phenomenon. It indicates on a qualitatively level that at our experimental temperatures such binding phenomenon might not necessarily be studied. It is possible that due to the temperature reached by the chip during the experiment the two effects of heating and streaming opposed one other, negating any positive streaming effects. In any case, it will be necessary to take further measurements in order to quantify these two opposite effects. First of all the streptavidin binding must be studied with the streaming effect but with all the functionalization methods and after that a scan in the SAW power should be made. These and other experiments will be necessary to explain these phenomena.

Figure 4.20 (a), (b) and (c) show the shifts of the R streptavidin curve to the R PBS curve in the three cases. In Figure 4.19 (d) the mean value of λ_{min} in the three cases are shown.

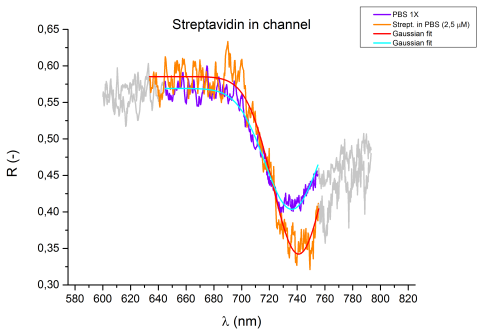

(a) R vs. λ of a typical measurement taken in the case of PBS (1X) and streptavidin in PBS (2.5 μM) on chip without SAW.

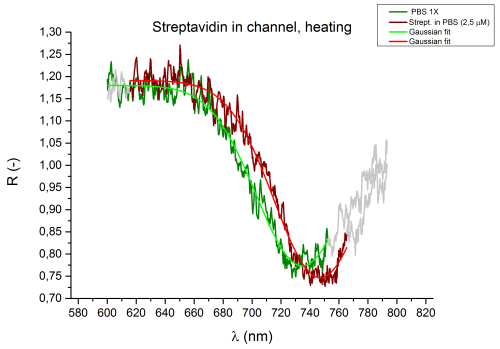

(b) R vs. λ of a typical measurement taken in the case of PBS (1X) and streptavidin in PBS (2.5 μM) on chip in the area where only the heating effect of SAW was present.

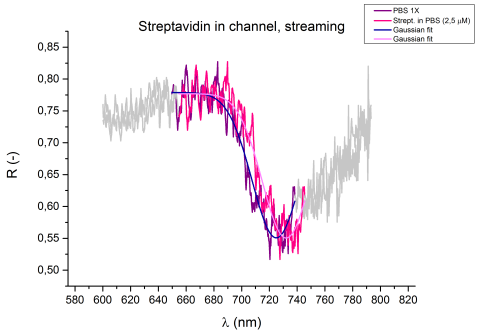

(c) R vs. λ of a typical measurement taken in the case of PBS (1X) and streptavidin in PBS (2.5 μM) on chip with SAW.

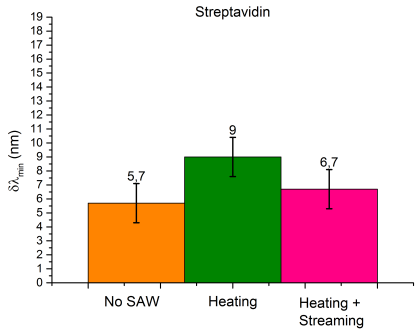

(d) Average resonant wavelength shift of streptavidin in PBS (2.5 μM) to PBS only in the case without SAW, with the heating effect of SAW, and with SAW, respectively.

Figure 4.20: Comparison of the normalized reflectivities of PBS and streptavidin in PBS (2.5 μM) in three cases: (a) without SAW, (b) in the area where only the heating effect of SAW was present and (c) with SAW. Data in grey were not used for the gaussian fit (see §4.1.1). Figure (d) shows the comparison between the average $\delta\lambda_{min}$ in these three cases.

Conclusions and Perspectives 5

A novel SAW-assisted SPR biosensor was realized and characterized. Advanced microfabrication techniques were used to make different chips which allowed the characterization of all the physical phenomena involved: SPR sensing and SAW-induced streaming of biological solutions. It was shown that for water-ethanol test solutions, a sensitivity of approximately 10^{-4} nm/RIU was reached. This sensitivity value is in line with the state of the art. The SPR signal with droplet-based SPR sensors was detected for different concentrations of streptavidin on gold areas functionalized with biotin and it was shown that streptavidin concentrations between 25 nM and 250 nM could be detected. This result is comparable or even slightly better than the results of some published localized SPR-biosensor [38] and the measured surface affinity constant $K_{A,surf}$ ($K_{A,surf} = (5.5 \pm 2.2) \cdot 10^6\ M^{-1}$) was in agreement with typical values found in literature (e.g., $(7.3 \pm 0.2) \cdot 10^6\ M^{-1}$, [50]). After the characterization of SPR sensing in microchannel, consecutive affinity experiments were made with SAWs active on the chip. This master thesis showed that the sensitivity of biosensors based on SPR can be enhanced by integrating SAW-driven microfluidics.

In the experiment with SAW the resonant wavelength shift caused by the functionalization of the SPR surface with biotin was found to be about 5 times higher than without SAW. Feedback controls showed that such an enhancement could only be due to the SAW-induced streaming effect. In fact, in the area of the chip where only the SAW-induced heating effect was present the signal was half of the signal where SAW-induced streaming was also present.
The possibility to decouple these two SAW-induced effects is really important because it was demonstrated [55] that an increase in temperature promotes the attachment of thiol-modified biotin to gold. The higher resonant wavelength shift with SAW active showed that a higher refractive index shift occurred at the gold-fluid interface which suggests that more biotin molecules were attached onto the gold surface. This enhancement can stem from the accelerated mixing induced by SAW in the microchannel chamber. It is likely that for this reason the probability of biotin coming in contact with the gold surface was increased, resulting in a more efficient functionalization. This extremely encouraging result paves the way for different new applications and studies.
For example, the next step will be to do the biotin functionalization at different SAW powers (i.e., SAW amplitudes) to see how SAW amplitude affects the streaming in the microchannel and in turn affects functionalization. By increasing the SAW amplitude, the maximum velocity of the velocity field of the fluid is increased (as it was shown in a previous work [34]) resulting in faster and stronger streaming with different streamlines.

In general, increasing the temperature will weaken the biological binding phenomena and above certain temperatures the biological system can even be damaged. The former happens for the biotin-streptavidin binding [51]. This was highlighted by the results obtained for the streptavidin solution. In contrast to the results obtained for biotin, no enhancement of the detection signal occurred with the SAW active. The heating effect likely changed the dynamics of the biotin-streptavidin binding completely weakening the positive effect of SAW-induced streaming (it is also possible that in this case streaming had the contrary effect of the biotin case). In the case of streptavidin other several measurements have to be taken to have a clear idea of the situation at the temperature and type of streaming involved in the microchannel. If it is shown that this is the case, the chip might be modified in order to avoid the heating effect of SAW onto the substrate making it possible to work at lower temperatures. For example, the sample holder can be modified to act as a Peltier cell in order to keep the chip substrate at a set temperature.

Other improvements can be made in the optical setup in order to enable real-time measurements of biological binding kinetics. In fact, monitoring the biological and chemical reaction allows the investigation of how different experimental conditions can influence the speed of the reaction, making it possible to find the configuration at which the reaction is as fast as possible; reducing the time of the experiments. Moreover, real-time measurements yield information about the reaction's mechanism, as well as the construction of mathematical models that can describe the characteristics of a chemical reaction. The polarizer was manually rotated during the various experiments made in this work. Such a procedure took about 10 *sec* for each spetrum acquisition, i.e., about 20 *sec* to acquire the reflectance spectra of s-polarized and p-polarized light (necessary to calculate the normalized reflectivity to detect the SPR) and all the kinetics occurring within this time get lost. The detection system can be accelerated by mounting the polarizer onto an automated rotation platform reducing the detection times down to the second. Another limit of the setup used for the SPR detection was the noise in the measurements caused by the fact that the cross-section of the light beam was larger than the SPR detection area. By replacing the two diaphragms with converging lenses or by adding them to the setup used in these experiments the spot size of the beam can be diminished down to the SPR gold area enhancing the signal to noise ratio.

The chip design allows the possibility of adding further feedback controls. This can be done by functionalizing only two of the four SPR areas (one for each chamber). In the same way it is possible to functionalize one of the two couples of the SPR surfaces with a different biorecognition element. Two different analyses can be performed on the same sample, avoiding waste and obtaining more specific results.

As discussed above, various improvements can be made to the SAW-based SPR chip and setup used in this work, although the results found are really encouraging and show a step forward as compared to conventional SPR devices. Taken together, the results presented in this thesis show that SPR biosensors can be succesfully integrated with SAW-driven microfluidic components. Importantly, the presence of SAW enhanced the functionalization procedure of the chip. This can

represent a step forward for the enhancement of SPR biosensor sensitivity making it possible to quickly detect diseases in a highly reliable way from solutions of human blood by lowering the limit of detection.

List of Tables

List of Figures

Nomenclature

$\bar{n}$	average refractive index
$\hat{\boldsymbol{i}}$	unit vector in i-direction
$\boldsymbol{k}$	wavevector
$\boldsymbol{r}$	position vector
$\boldsymbol{S}$	strain matrix
$\boldsymbol{T}$	stress matrix
ϵ	real part of the dielectric constant
η	coefficient of viscosity
Γ	surface concentration (mass/area) of a given analyte
λ	wavelength of light in vacuum
$\mathbf{E}$	electric field
$\mathbf{u}(x, y, z, t)$	displacement vector
ω	angular frequency
ρ	density
ζ	coefficient of viscosity
B_{max}	maximum binding capacity
C	concentration
c	propagation velocity of light in vacuum
C_0	capacitance per finger pairs
c_{ijkl}	elastic stiffness constants
e	electron charge
f	frequency
f_0	synchronous frequency
G	conductance

h	sensor surface thickness
i	imaginary unit
$I_{r,p}$	intensity of the p-polarized light reflected by the prism
$I_{r,s}$	intensity of the s-polarized light reflected by the prism
K^2	electromechanical coupling coefficient
K_A	equilibrium association constant
K_D	equilibrium dissociation constant
L_{pd}	penetration depth
m_e	electron mass
n	refractive index
n_d	refractive index at 587.6 nm
N_f	total number of fingers
N_p	number of IDT periods
n_{12}	refractive index of a binary mixture
n_{ef}	effective refractive index of an SP
P	power
p	fluid pressure
R	normalized reflectivity
R_p	reflectivity of p-polarized light
r_p	complex reflection coefficient of p-polarized light
R_s	reflectivity of s-polarized light
R_{eq}	shift in SPR angle/wavelength at equilibrium
Re	Reynold's number
S	observed signal
S_c	sensitivity of an SPR biosensor
S_h	refractive index sensitivity of sensor output to a refractive index change within the sensitive layer of a thickness h
S_{11}	diagonal term of the scattering matrix, S
S_{RI}	sensitivity of the output to a refractive index change
t	time
t_{exp}	exposure time

u_i particle displacement in the i-direction

v_{sound} SAW propagation velocity along the substrate

W IDT aperture

X detuning parameter

x_s SAW attenuation length

Y sensor output

γ complex propagation factor

λ_{min} resonant wavelength

λ_{SAW} SAW wavelength

ω_p plasma frequency

$\prod_{ik}$ momentum flux density tensor

ρ_e free electron density

σ_Γ minimum resolvable change of molecular mass captured by biorecognition elements

σ_{RI} refractive index resolution

σ_{so} standard deviation of noise of an SPR sensor output

θ_R Rayleigh angle

c'_{IJ} piezoelectrically stiffened elastic constants in piezoelectric materials (abbreviating subscripts)

Abbreviations

DI *deionized*

IDT *interdigital transducer*

LN *lithium niobate*

PBS *phosphate-buffered saline*

PDMS *polydimethylsiloxane*

RVU *reflectance variation units*

SAW *surface acoustic wave*

SP *surface plasmon*

SPR *surface plasmon resonance*

WF *write field*

Bibliography

[1] Y. Temiz, R. D. Lovchik, G. V. Kaigala, and E. Delamarche. Lab-on-a-chip devices: How to close and plug the lab? *Microelectronic Engineering*, 132: 156–175, 2015.

[2] X. Ding, P. Li, S. S. Lin, Z. S. Stratton, N. Nama, F. Guo, D. Slotcavage, X. Mao, J. Shi, F. Costanzo, and T. J. Huang. Surface acoustic wave microfluidics. *Lab on a chip*, 13(18):3626–49, 2013.

[3] M. Li, S. K. Cushing, and N. Wu. Plasmon-enhanced optical sensors: a review. *The Analyst*, 140:386–406, 2015.

[4] C.J. Strobl, A. Rathgeber, A. Wixforth, C. Gauer, and J. Scriba. Planar microfluidic processors. *2002 IEEE Ultrasonics Symposium, 2002. Proceedings.*, 1 (c):255–258, 2002.

[5] Richie J. Shilton, Leslie Y. Yeo, and James R. Friend. Quantification of surface acoustic wave induced chaotic mixing-flows in microfluidic wells. *Sensors and Actuators B: Chemical*, 160(1):1565–1572, December 2011.

[6] A. Renaudin, V. Chabot, E. Grondin, V. Aimez, and P. G. Charette. Integrated active mixing and biosensing using surface acoustic waves (SAW) and surface plasmon resonance (SPR) on a common substrate. *Lab on a chip*, 10(1):111–5, January 2010.

[7] J. Homola. Surface Plasmon Resonance Sensors for Detection of Chemical and Biological Species. *Chemical Reviews*, pages 462–493, 2008.

[8] Schasfoort, R.B.M. and Tudos, A. J. *Handbook of SPR*. The Royal Society of Chemistry, 2008.

[9] Heinz Raether. *Surface Plasmons on Smooth and Rough Surfaces and on Gratings*. Springer-Verlag Berlin Heidelberg New York London Paris Tokyo, 1986.

[10] M. Cardona. Fresnel Reflection and Surface Plasmons. *American Journal of Physics*, 39(10):1277, 1971.

[11] F. J. Reitz, J. R., Milford. *Foundations of electromagnetic theory*. Addison-Wesley publishing company, inc., 1960.

[12] Kretschmann, E. and Raether, H. Radiative Decay of Non Radiative Surface Plasmons Excited by Light. *Zeitschrift für Naturforschung*, 1968.

[13] J. Homola and M. Piliarik. Surface plasmon resonance (spr) sensors. In *Surface Plasmon Resonance Based Sensors*, volume 4 of *Springer Series on Chemical Sensors and Biosensors*, pages 45–67. Springer Berlin Heidelberg, 2006.

[14] V. Thomsen, D. Schatzlein, and D. Mercuro. Limits of Detection in Spectroscopy. *Pure and Applied Chemistry*, 18(12):112–114, 2003.

[15] Young Rok Kim, Sungho Jung, Hyunil Ryu, Yeong Eun Yoo, Sun Min Kim, and Tae Joon Jeon. Synthetic biomimetic membranes and their sensor applications. *Sensors (Switzerland)*, 12:9530–9550, 2012.

[16] Wolfgang Knoll, Martha Liley, Darko Piscevic, Jürgen Spinke, and Michael J. Tarlov. Supramolecular architectures for the functionalization of solid surfaces. *Advances in Biophysics*, 34(0):231 – 251, 1997.

[17] D. S. Ballantine, R. M. White, S. J. Martin, A. J. Ricco, E. T. Zellers, G. C. Frye, and H. Wohltjen. *Acoustic Wave Sensors*. Elsevier, 1997.

[18] J. Friend and L. Yeo. Piezoelectric Materials for Microfluidics. In *Encyclopedia of Microfluidics and Nanofluidics*, pages 1654–1662. Springer US, 2008.

[19] K. K. Wong. Properties of lithium niobate. 2002.

[20] TERA XTAL TECHNOLOGY CORPORATION. Lithium niobate wafers. URL http://www.teraxtal.com/english/product_page/product_page7.html. [Online; accessed 31-May-2015].

[21] *Smart materials*. CRC Press, 2009.

[22] Roditi International. Lithium tantalate properties. URL http://www.roditi.com/SingleCrystal/Lithium-Tantalate/LiTaO3-Properties.html. [Online; accessed 31-March-2015].

[23] Lord Rayleigh. On Waves Propagated along the Plane Surface of an Elastic Solid. *Proc. London Math. Soc.*, s1-17, 1885.

[24] Campbell Colin. *Surface Acoustic Wave Devices and Their Signal Processing Applications*. Academic Press, inc., 1992.

[25] L. D. Landau and E. M. Lifshitz. *Fluid Mechanics*. Pergamon Press, 1959.

[26] Sir James Lighthill. On Sound Generated Aerodynamically. I. General Theory. *Proceedings of the Royal Society of London. Series A, Mathematical and Physical Sciences*, 211(1107):564–587, 1952.

[27] Sir James Lighthill. Acoustic streaming. *Journal of Sound and Vibration*, 61(3): 391–418, 1978.

[28] K. Sritharan, C. J. Strobl, M. F. Schneider, a. Wixforth, and Z. Guttenberg. Acoustic mixing at low Reynold's numbers. *Applied Physics Letters*, 88(5): 054102, 2006.

[29] Carl Eckart. Vortices and streams caused by sound waves. *Phys. Rev.*, 73: 68–76, Jan 1948.

[30] Martin Wiklund, Roy Green, and Mathias Ohlin. Acoustofluidics 14: Applications of acoustic streaming in microfluidic devices. *Lab on a Chip*, 12(14): 2438, 2012.

[31] M. K. Tan, L. Y. Yeo, and J. R. Friend. Rapid fluid flow and mixing induced in microchannels using surface acoustic waves. *EPL (Europhysics Letters)*, 87 (4):47003, 2009.

[32] Trung-Dung Luong, Vinh-Nguyen Phan, and Nam-Trung Nguyen. High-throughput micromixers based on acoustic streaming induced by surface acoustic wave. *Microfluidics and Nanofluidics*, 10(3):619–625, 2011.

[33] R. Shilton, M. K. Tan, L. Y. Yeo, and James R. Friend. Particle concentration and mixing in microdrops driven by focused surface acoustic waves. *Journal of Applied Physics*, 104(1):014910, 2008.

[34] Carlo Maria Lazzarini. Tecnologia microfluidica ad onde acustiche di superficie integrata in microsensori basati su risonanza plasmonica di superficie. Master's thesis, Università di Pisa, 2014.

[35] B-H Jo, L. M. Van Lerberghe, K. M. Motsegood, and D. J. Beebe. Three-dimensional micro-channel fabrication in polydimethylsiloxane (pdms) elastomer. *Microelectromechanical Systems, Journal of*, 9(1):76–81, 2000.

[36] G. De Simoni, G. Signore, M. Agostini, F. Beltram, and V. Piazza. A surface-acoustic-wave-based cantilever bio-sensor. *Biosensors and Bioelectronics*, 68: 570–576, 2015.

[37] Jiri Homola. On the sensitivity of surface piasmon resonance sensors with spectral interrogation. 41:207–211, 1997.

[38] T. Arai, P. K. R. Kumar, C. Rockstuhl, K. Awazu, and J. Tominaga. An optical biosensor based on localized surface plasmon resonance of silver nanostructured films. *Journal of Optics A: Pure and Applied Optics*, 9(7):699–703, July 2007.

[39] S. Kedenburg, M. Vieweg, T. Gissibl, and H. Giessen. Linear refractive index and absorption measurements of nonlinear optical liquids in the visible and near-infrared spectral region. *Optical Materials Express*, 2(11):1588, 2012.

[40] Nenad Radojkovld and Experimental Sodion. Use of Mixing Rules in Predicting Refractive Indices and Specific Refractivities for Some Binary Liquid Mixtures. 313(16):310–313, 1992.

[41] N. F. Chiu, Y. C. Tu, and T. Y. Huang. Enhanced sensitivity of anti-symmetrically structured surface plasmon resonance sensors with zinc oxide intermediate layers. *Sensors (Basel, Switzerland)*, 14(1):170–187, 2013.

[42] S. K. Srivastava, R. Verma, and B. D. Gupta. Surface plasmon resonance based fiber optic sensor for the detection of low water content in ethanol. *Sensors and Actuators, B: Chemical*, 153(1):194–198, 2011.

[43] H. Rhee, P. Zou, N. D. Udeshi, J. D. Martell, V. K. Mootha, S. A. Carr, and A. Y. Ting. Proteomic mapping of mitochondria in living cells via spatially restricted enzymatic tagging. *Science*, 339(6125):1328–1331, 2013.

[44] R. Raiteri, M. Grattarola, H. J. Butt, and P. Skládal. Micromechanical cantilever-based biosensors. *Sensors and Actuators, B: Chemical*, 79(2-3):115–126, 2001.

[45] K. Tanaka, S. Yokoi, K. Morimoto, T. Iwata, Y. Nakamoto, K. Nakayama, K. Koyama, T. Fujiwara, and K. Fukase. Cell surface biotinylation by azaelectrocyclization: Easy-handling and versatile approach for living cell labeling. *Bioorganic and Medicinal Chemistry*, 20(6):1865–1868, 2012.

[46] S. I. Park, J. Shenoi, S. M. Frayo, D. K. Hamlin, Y. Lin, D. S. Wilbur, P. S. Stayton, N. Orgun, M. Hylarides, F. Buchegger, et al. Pretargeted radioimmunotherapy using genetically engineered antibody-streptavidin fusion proteins for treatment of non-hodgkin lymphoma. *Clinical Cancer Research*, 17 (23):7373–7382, 2011.

[47] P.C. Weber and F. R. Salemme. Structural origins of high-affinity biotin binding to streptavidin. URL http://www.rcsb.org/pdb/explore/explore.do?structureId=1STP. [Online; accessed 2-April-2015].

[48] Wikipedia. Biotin. URL http://en.wikipedia.org/wiki/Biotin. [Online; accessed 2-April-2015].

[49] X. Duan, Y. Li, N. K. Rajan, D. A. Routenberg, Y. Modis, and M. A. Reed. Quantification of the affinities and kinetics of protein interactions using silicon nanowire biosensors. *Nature Nanotechnology*, 7(6):401–407, 2012.

[50] Y. Tang, R. Mernaugh, and X. Zeng. Nonregeneration protocol for surface plasmon resonance: study of high-affinity interaction with high-density biosensors. *Analytical Chemistry*, 78(6):1841–1848, 2006.

[51] Y. Lo, J. Simons, and T. P. Beebe. Temperature dependence of the biotin−avidin bond-rupture force studied by atomic force microscopy. *The Journal of Physical Chemistry B*, 106(38):9847–9852, 2002.

[52] Alexey N Bashkatov and Elina A Genina. Water refractive index in dependence on temperature and wavelength: a simple approximation. In *Saratov Fall Meeting 2002: Optical Technologies in Biophysics and Medicine IV*, pages 393–395. International Society for Optics and Photonics, 2003.

[53] Juan Ortega. Densities and refractive indices of pure alcohols as a function of temperature. *Journal of Chemical and Engineering Data*, 27(3):312–317, 1982.

[54] Mitsuo Kawasaki, Tomoo Sato, Takumi Tanaka, and Kazunori Takao. Rapid self-assembly of alkanethiol monolayers on sputter-grown Au(111). *Langmuir*, 16(4):1719–1728, 2000.

[55] R. Yamada, H. Wano, and K. Uosaki. Effect of Temperature on Structure of the Self-Assembled Monolayer of Decanethiol on Au(111) Surface. *Langmuir*, 16(13):5523–5525, 2000.

[56] A. Abbas, M. J. Linman, and Q. Cheng. New trends in instrumental design for surface plasmon resonance-based biosensors. *Biosensors and Bioelectronics*, pages 1–10, 2010.

[57] Irving Langmuir. The adsorption of gases on plane surfaces of glass, mica and platinum. *Journal of the American Chemical Society*, 40(9), 1918.

[58] F. Labeed and H. Fatoyinbo, editors. *Microfluidics in Detection Science*. Royal Society of Chemistry, 2013.

[59] J. Friend and L. Y. Yeo. Microscale acoustofluidics: Microfluidics driven via acoustics and ultrasonics. *Reviews of Modern Physics*, 83(2):647–704, June 2011.

[60] S. Patskovsky, M. Maisonneuve, M. Meunier, and A. V. Kabashin. Mechanical modulation method for ultra- sensitive phase measurements in photonics biosensing. 16, 2008.

[61] T. Franke and A. Wixforth. Microfluidics for miniaturized laboratories on a chip. *Chemphyschem : a European journal of chemical physics and physical chemistry*, 9(15):2140–56, October 2008.

[62] Ghulam Destgeer, Sunghyuk Im, Muhammad Nadeem, Jin Ho Jung, Byunghang Ha, Anas Alazzam, and Hyung Jin Sung. μ-PIV of acoustic streaming flow induced via focus travelling surface acoustic waves (F-TSAW). 2013.

[63] L. Y. Yeo and J. R. Friend. Ultrafast microfluidics using surface acoustic waves. *Biomicrofluidics*, 3(1), January 2009.

[64] Andrew N. Cleland. *Foundations of Nanomechanics*. Springer, 2003.

[65] T. Tumolo, L. Angnes, and M. S. Baptista. Determination of the refractive index increment (dn/dc) of molecule and macromolecule solutions by surface plasmon resonance. *Analytical Biochemistry*, 333:273–279, 2004.

[66] M. E. Mcintyre. On the 'wave momentum' myth. *Journal of Fluid Mechanics*, 106:331–347, 5 1981. ISSN 1469-7645.

[67] Todd M. Squires and Stephen R. Quake. Microfluidics: Fluid physics at the nanoliter scale. *Reviews of Modern Physics*, 77(3):977–1026, 2005.

[68] Richie J. Shilton, Marco Travagliati, Fabio Beltram, and Marco Cecchini. Nanoliter-droplet acoustic streaming via ultra high frequency surface acoustic waves. *Advanced Materials*, 26(29):4941–4946, 2014.

[69] G. G. Stokes. On the theories of the internal friction in fluids in motion, and of the equilibrium and motion of elastic solids. *Transaction of the Cambridge Philosophical Society*, 8:287–342, 1845.

[70] Jacques Curie and Pierre Curie. Development, via compression, of electric polarization in hemihedral crystals with inclined faces. *Bulletin de la Societe de Minerologique de France*, 3:90–93, 1880.

[71] Jacques Curie and Pierre Curie. Contractions and expansions produced by voltages in hemihedral crystals with inclined faces. *Comptes Rendus*, 93:1137–1140, 1881.

[72] R. W. Wood. On a remarkable case of uneven distribution of light in a diffraction grating spectrum. *Philosofical Magazine*, 4:396–402, 1902.

[73] R. W. Wood. Preliminary note on the electron atmospheres of metals. *Philosofical Magazine*, 24:396–402, 1912.

[74] R Karlsson, a Michaelsson, and L Mattsson. Kinetic analysis of monoclonal antibody-antigen interactions with a new biosensor based analytical system. *Journal of immunological methods*, 145(1-2):229–240, 1991.

[75] F. Real-Fernández, I. Passalacqua, E. Peroni, M. Chelli, F. Lolli, A. M. Papini, and P. Rovero. Glycopeptide-Based Antibody Detection in Multiple Sclerosis by Surface Plasmon Resonance. *Sensors*, 12(5):5596–5607, 2012.

[76] E. M. Munoz, J. Correa, R. Riguera, and E. Fernandez-Megia. Real-time evaluation of binding mechanisms in multivalent interactions: A surface plasmon resonance kinetic approach. *Journal of the American Chemical Society*, 135(16): 5966–5969, 2013.

[77] K. Anraku, R. Fukuda, N. Takamune, S. Misumi, Y. Okamoto, M. Otsuka, and M. Fujita. Highly sensitive analysis of the interaction between HIV-1 gag and phosphoinositide derivatives based on surface plasmon resonance. *Biochemistry*, 49(25):5109–5116, 2010.

[78] Y. Uludag and I. E. Tothill. Cancer biomarker detection in serum samples using surface plasmon resonance and quartz crystal microbalance sensors with nanoparticle signal amplification. *Analytical Chemistry*, 84(14):5898–5904, 2012.

[79] J. Behrens, S. Langelier, A. R. Rezk, G. Lindner, L. Y. Yeo, and J. R. Friend. Microscale anechoic architecture: acoustic diffusers for ultra low power microparticle separation via traveling surface acoustic waves. *Lab Chip*, 15(1): 43–46, 2015.

[80] L. Masini, M. Cecchini, S. Girardo, R. Cingolani, D. Pisignano, and F. Beltram. Surface-acoustic-wave counterflow micropumps for on-chip liquid motion control in two-dimensional microchannel arrays. *Lab on a chip*, 10(15): 1997–2000, 2010.

[81] T. Franke, A. R. Abate, D. Weitz, and A. Wixforth. Surface acoustic wave (SAW) directed droplet flow in microfluidics for PDMS devices. *Lab on a chip*, 9(18):2625–2627, 2009.

[82] K. M. Ang, L. Y. Yeo, J. R. Friend, Y. M. Hung, and M. K. Tan. Nozzleless spray cooling using surface acoustic waves. *Journal of Aerosol Science*, 79:48–60, 2015.

[83] M. Li, S. K. Cushing, and N. Wu. Plasmon-enhanced optical sensors: a review. *The Analyst*, 140:386–406, 2014.

[84] Xiaowei Guo. Surface plasmon resonance based biosensor technique: A review, 2012.

[85] O. Tigli and M. Zaghloul. Circular surface acoustic wave (saw) devices, processes for making them, and methods of use, September 13 2011. US Patent 8,018,010.

[86] F. Beltram, R. Cingolani, M. Cecchini, S. Girardo, and D. Pisignano. Device for controlling fluid motion into micro/nanochannels by means of surface acoustic waves, March 12 2013. US Patent 8,393,356.

[87] T.J. Huang and J. Shi. Particle focusing within a microfluidic device using surface acoustic waves, November 5 2013. US Patent 8,573,060.

[88] V. Piazza, G. De Simoni, M. Cecchini, M. Travagliati, and F. Beltram. Automatic passive control of liquid positioning in microfluidic chips, August 20 2014. EP Patent App. EP20,120,790,652.

[89] Daniel J. O'Shannessy, Michael Brigham-Burke, and Kim Peck. Immobilization chemistries suitable for use in the {BIAcore} surface plasmon resonance detector. *Analytical Biochemistry*, 205(1):132 – 136, 1992.

[90] S. Lrofas, B. Johnsson, A. Edström, A. Hansson, G. Lindquist, R. Muller Hillgren, and L. Stigh. Methods for site controlled coupling to carboxymethyldextran surfaces in surface plasmon resonance sensors. *Biosensors and Bioelectronics*, 10(9–10):813 – 822, 1995.

[91] Y. Q. Fu, J. K. Luo, X. Y. Du, a. J. Flewitt, Y. Li, G. H. Markx, a. J. Walton, and W. I. Milne. Recent developments on ZnO films for acoustic wave based bio-sensing and microfluidic applications: a review. *Sensors and Actuators, B: Chemical*, 143(2):606–619, 2010.

[92] Trung Dung Luong and Nam Trung Nguyen. Surface Acoustic Wave Driven Microfluidics – A Review. *Micro and Nanosystemse*, 2(3):217–225, 2010.

[93] R.D. Harris and J.S. Wilkinson. Waveguide surface plasmon resonance sensors. *Sensors and Actuators B: Chemical*, 29(1-3):261–267, 1995.

[94] C. Lavers and J.S. Wilkinson. A waveguide-coupled surface-plasmon sensor for an aqueous environment. 22:75–81, 1994.

[95] J. Čtyrokỳ, J. Homola, and M. Skalskỳ. Tuning of spectral operation range of a waveguide surface plasmon resonance sensor. *Electronics Letters*, 33(14): 1246–1248, 1997.

[96] A. R. Rezk, O. Manor, J. R. Friend, and L. Y. Yeo. Unique fingering instabilities and soliton-like wave propagation in thin acoustowetting films. *Nature Communications*, 3:1167, 2012.

[97] A. Holmberg, A. Blomstergren, O. Nord, M. Lukacs, J. Lundeberg, and M. Uhlén. The biotin-streptavidin interaction can be reversibly broken using water at elevated temperatures. *Electrophoresis*, 26(3):501–510, 2005.